SPACE RESEARCH COORDINATION CENTER

THE FORMATION OF EXCITED ATOMS DURING CHARGE EXCHANGE BETWEEN HYDROGEN IONS AND ALKALI IONS

BY

RONALD ALLEN NIEMAN

SRCC REPORT NO. 180

UNIVERSITY OF PITTSBURGH

PITTSBURGH, PENNSYLVANIA

1971

The Space Research Coordination Center, established in May, 1963, has the following functions: (1) it administers predoctoral and postdoctoral fellowships in space-related science and engineering programs; (2) it makes available, on application and after review, allocations to assist new faculty members in the Division of the Natural Sciences and the School of Engineering to initiate research programs or to permit established faculty members to do preliminary; work on research ideas of a novel character; (3) in the Division of the Natural Sciences it makes an annual allocation of funds to the Interdisciplinary Laboratory for Atmospheric and Space Sciences; (4) in the School of Engineering it makes a similar allocation of funds to the Department of Metallurgical and Materials Engineering and to the program in Engineering Systems Management of the Department of Industrial Engineering; and (5) in concert with the University's Knowledge Availability Systems Center, it seeks to assist in the orderly transfer of new space-generated knowledge in industrial application. The Center also issues periodic reports of space-oriented research and a comprehensive annual report.

The Center is supported by an Institutional Grant (NsG-416) from the National Aeronautics and Space Administration, strongly supplemented by grants from the A. W. Mellon Educational and Charitable Trust, the Maurice Falk Medical Fund, the Richard King Mellon Foundation and the Sarah Mellon Scaife Foundation. Much of the work described in SRCC reports is financed by other grants, made to individual faculty members.

THE FORMATION OF EXCITED ATOMS DURING CHARGE EXCHANGE BETWEEN HYDROGEN IONS AND ALKALI ATOMS

By

Ronald Allen Nieman

B.S., Carnegie Institute of Technology, 1963

Submitted to the Graduate Faculty of
Arts and Sciences in partial fulfillment of
the requirements for the degree of
Doctor of Philosophy

University of Pittsburgh

1971

THE FORMATION OF EXCITED ATOMS DURING CHARGE EXCHANGE BETWEEN HYDROGEN IONS AND ALKALI ATOMS

Ronald Allen Nieman, Ph.D.

University of Pittsburgh, 1972

Advisor: Thomas M. Donahue

The charge exchange cross sections for protons and various alkali atoms have been calculated using the classical approximation of Gryzinski. It is assumed that the hydrogen atoms resulting from charge exchange exist in all possible excited states. Charge transfer collisions between protons and potassium as well as protons and sodium atoms have been studied in this work. The energy range investigated is between 4 and 30 keV. The theoretical calculations of $_{10}\sigma_{01}$ have been compared to measurements of σ_{10} made in the course of this work as well as other data. Also the calculated cross section for the creation of metastable 2S hydrogen has been compared to other experimental values. Good quantitative agreement is found for σ_{10} but only qualitative agreement for the metastable cross section. Analysis of the Lyman alpha window in molecular oxygen suggests that measured values of $\sigma(2S)$ may be in error. In addition to σ_{10}, thick alkali target data are presented. This allows the determination of the electron loss cross section σ_{01}. Finally, some work has been done with H_2^+.

FOREWORD

The author wishes to thank his advisor, Dr. T. M. Donahue, for his patience, guidance and minimum of control. The aid of R. T. Brackmann, W. R. Ott and W. E. Kauppila in the construction of the Geiger tubes is appreciated. I also would like to applaud the constructive genius of Morrie, Mac and the rest of the machine shop in putting together the apparatus as it should be and not as I said it was to be. To my cohorts and fellow drunks, thanks. I would like to thank Mrs. Meriem Green, who took time out from running the Physics Department, for typing this manuscript.

The author also wishes to acknowledge the works of another author, a Mr. W. Shakespeare, whose words for a fitting motto for this work. As Macbeth says in V.5. "Tis a tale...".

This work was supported in part by Navy Grant NONR 624-06.

TABLE OF CONTENTS

Table of Contents Continued

Table of Contents Continued

1.0. INTRODUCTION

Inelastic collisions between charged particles and neutral atoms and molecules have been studied for many years. In the 1930's Tate, Smith and Bleakney investigated interactions between electrons and atmospheric gases.[1-4] Heavy ion interactions have been studied too. Proton and atmospheric gas collisions have also been extensively investigated. The theories that have tried to explain the results obtained have involved approximations of one sort or another. The Born approximation has been used for high energy interactions.[5] Massey has deduced a simple expression that involves physically reasonable quantities for a two body collision.[6] This has provided insight into the problems but has not been able to predict the cross sections.

For the simpler colliding partners there is now good agreement between theory and experiment. However, even electron impacts with hydrogen atoms still yield surprises.[7] Of the many types of inelastic encounters one of the simplest is charge exchange. The fast probe ion captures an electron from the neutral target. Hasted tabulated many such cross sections.[8] He was able to deduce a typical value for the effective interaction distance.[6] It is a few atomic diameters. Consequently, it has become possible to predict the energy where the cross section is largest but not its magnitude. Section 2.3.2 deals with this in more detail.

An interaction that should be fairly easy to study is a proton colliding with an alkali atom. Both reactants are hydrogen-like. Theory and experiment compare favorably for the proton-hydrogen atom collision

system.[9-11] Furthermore, from the experimental point of view there is a simplifying circumstance. The removal of the target gas is expedited. A large cold surface will condense the alkalis. For example, at zero degrees Celsius the vapor pressure of sodium and potassium are respectively 2(-12)* Torr and 1(-9) Torr.[12] With normal target gases the only method of evacuation is to remove them with a high speed vacuum pump.

The cold trap method has been used before. One recent usage was in the experiment of Futch and Damm.[13] They pumped not only lithium with such a surface but also water vapor. These two substances were neutralizers for protons.

Recently interest has been aroused in proton-alkali reactions. Collisions leave the fast neutralized atoms in a highly excited state. Plasma machines using magnetic mirrors were initially designed to build the plasma by injecting fast H_2^+. At first it was thought that dissociation of the fast ions by the residual gas would increase the proton concentration. It was found charge transfer with these same residuals actually removed the fast ions. A mechanism for dissociation without collisions was sought. One such is the Lorentz force acting on the ions as they move in the intense magnetic fields. This effect is also mentioned in Section 5.5.2 on losses.

This general mechanism is called Lorentz ionization.[14] It would be useful also for hydrogen atoms. Highly excited atoms would be quite efficiently ionized this way.[15-17] In this injection method states below $n = 6$ are not expected to contribute significantly since the radiative

---

*Throughout powers of ten are expressed in the above fashion; for example, 2(-12) means 2×10^{-12}.

lifetimes are too short.[18] Those above n = 15 are generally ignored because of their weak binding energies. They would be too easily ionized by fringe fields.[19] Recent papers have been concerned with creating those states in between.[13,20,21]

Besides this work on neutral injection, it has been discovered these targets are useful for converting protons into H^- for accelerators. Cesium seems to be the prefered alkali target for this purpose.[22,23]

Donnally[24] discovered that with a cesium target, metastable hydrogen atoms were created from protons. He measured this cross section from 160 eV to 3 keV. A listing of experimenters and their alkali work will be given later. Other metastable sources recently used or discussed were proton-molecular hydrogen,[25-27] proton-atomic hydrogen,[9,28-30] proton-rare gas[27,31] and atom-atom[30] collisions. In addition Lyman alpha radiation had been seen during electron impact on H_2 [32] and proton-rare gas[26] and various ion-molecule collisions.[33,34]

Michal Gryzinski has published a series of papers on charged particle interaction.[35-39] He uses classical mechanics and calculates his results in the LAB frame instead of the traditional CM (center of mass) frame. The approximate form for the charge exchange cross section is very simple. There is good agreement with experimental values for many cases. Modification of his simple theory has been carried out for a great variety of collision partners.[40] One example is presented herein.

For a proton probe and alkali target the binding energies are well known. There seems to be no reason for excluding capture into <u>all</u> excited hydrogen levels. Thus a sum of these cross sections is needed. Throughout, the term "partial cross section" will refer to one of these. The sum becomes a finite integral with a few simple assumptions. It is

possible to calculate the cross sections for electron capture into the metastable $2S_{\frac{1}{2}}$ level as well as the total cross section.

Calculations for the proton-alkali vapor interaction are presented in Section 2. Cross sections for the two charge state are discussed. A simple extension of Gryzinski's approximate form for charge exchange is the basis for computing various cross sections as a function of probe energy. Total electron capture (σ_{10}) values can be obtained this way.

The total cross section (TX) is the sum of many partial ones. Particularly interesting is the cross section for the creation of hydrogen atoms in the first excited state. Some of these atoms will be in the metastable $2S_{\frac{1}{2}}$ state. This metastable cross section (MX) will be some fraction of the cross section for capture into the first excited hydrogen state. Relative statistical weights place this fraction at 1/4. The ratio of MX to TX can be calculated. The maximum value would be 0.25 if the states were populated according to their weights.

Whenever the above calculations are extended to include capture of inner shell electrons, there is a noticeable change in the above theoretical results. Usually for low energy protons, the valence electron values dominate the cross sections. Beyond a few tens of kilovolts of proton energy the inner shell contributions become important.

The experimental and theoretical results of this work are compared with those of other experimenters. Both TX and MX values are collated. Until very recently no one group had measured both cross sections for one alkali. Some anomalies appear in this compendium. They will be discussed later.

Total exchange values have been determined by groups working in many countries. Cross sections have been measured by Il'in, Oparin, Solov'ev, and Federenko[21] in Russia, Schmelzbach and coworkers[41] in Switzerland, and Schlachter[42] in this country. Principal investigators of the metastable cross sections include Colli,[26,43] Donnally[24] and Sellin.[44,45] Spiess, Valance and Pradel,[46] working in France, found both TX and MX for cesium.

TX values are measured in the present work for potassium and sodium targets. The proton energy range is 4 to 30 keV. These TX values can be matched with those of Il'in[21] and Schmelzbach.[41] The equilibrium neutral fractions (2.11) are also compared. Theoretical values for TX for cesium may be related to those obtained by Schlachter et al.[42]

Metastable creation by charge exchange has also been noticed. The modified Gryzinski metastable cross sections will be compared with those measured by Donnally[26] and Sellin.[45] Both have used cesium.

Cesium has been vigorously, if somewhat confusingly, investigated. TX for rubidium has not been determined in this energy range. Sodium and potassium are the convenient targets used here. Their cross sections should differ by about a factor of two. Lithium should have the smallest value of all the alkalis at any given energy. Table 1.1 lists the various groups and the types of measurements they have taken.

The classical theory of Gryzinski is modified in Section II. Comparisons are drawn between its predictions and observations with a proton beam. In this work the protons collide with sodium and potassium atoms. The ions are accelerated through 4 to 30 keV. The hydrogen molecular ion probes the same two targets above 10 keV. Its electron

capture cross section and its neutralized beam fraction for a thick target are also measured. No calculations have been done for H_2^+ nor have any other measurements been found for comparison.

A possible explanation for the greatly enhanced MX observations is given. It involves the Doppler shift of UV radiation and the narrowness of the transmission windows of oxygen. Some of the light will be shifted outside the Lyman alpha window. This effect of the molecular oxygen filter for the UV detector is somewhat fancifully described as the "velocity dependent solid angle" of the Lyman alpha counter. Resonant radiation has been seen in the exchange chamber. This glow seems to be caused by excited alkali atoms.

The theory section - Section 2 - is followed by the description of the apparatus. This includes the oxygen filter explanation in Section 3.10. Data-taking procedures and sample data comprise Section 4. The results of the experiment and the calculations are given in Section 5. The conclusions form the final segment of the body of this paper. Various tangential matters appear in the appendices.

2.0. THEORY

2.1. Nomenclature

Consider a rearrangement collision in which a fast particle (B) with initial charge $\underline{i}$ encounters a target particle (A). After the interaction the beam particle has charge $\underline{f}$. This is written as

$$B^i + A^j \rightarrow B^f + A^g + (f+g-i-j)e \qquad (2.1)$$

where the fast particle is written first. The following short-hand notation could also be used:

$$A^j(B^i, B^f)A^j \quad . \qquad (2.2)$$

The cross section for this reaction is written[8] as ${}_{ij}\sigma_{fg}$.

In practice there is a stream of these fast ions which encounter a localized aggregation of targets. This latter grouping is presented in terms of a number density $[n_j(x)]$ which is a function of distance along the beam track. The subscript marks one of several targets than can coexist in the region. The number of particles with charge $\underline{i}$ varies with the distance (x) along the track. If there are several reactions converting charges from $\underline{i}$ to $\underline{f}$, each one can involve different targets. This can be written as

$$dN^i(x) = \Sigma_{j,g} N^f(x)\ {}_{fg}\sigma_{ij}\ n_g(x)dx - \Sigma_{j,g} N^i(x)\ {}_{ij}\sigma_{fg}\ n_j(x)dx \quad . \qquad (2.3)$$

The source terms are collisions like (2.1) that convert net charge $\underline{i}$ to final charge $\underline{f}$. The loss terms remove $\underline{f}$ by returning the charge state to $\underline{i}$.

For protons interacting with alkali atoms there are three such charge states for the probe ion (1,0,-1). That case is treated in Appendix A. If a negligible number of H^- ions are formed, the equations in the next section are adequate.

2.2. The Two Charge State

If only two charge states are possible, Equation (2.3) is greatly simplified. It is more convenient, however, to discuss the fraction (F^i) of the probe beam that has charge $\underline{i}$ instead of the number. This is accomplished by dividing by the total number of beam particles. Furthermore, the total alkali density irrespective of charge is n_T. Let the product $n_T(x)\,dx$ be given by $d\pi$. The total electron loss cross section (σ_{10}) and the total electron capture cross section (σ_{01}) are given by

$$\begin{aligned} \sigma_{10} &= \sum_{j=0} \nu_j \sum_{g=j+1} {}_{1j}\sigma_{0g} \quad \text{[electron loss]} \\ \sigma_{01} &= \sum_{j=0} \nu_j \sum_{g=0} {}_{0j}\sigma_{1g} \quad \text{[electron capture]} \end{aligned} \tag{2.4}$$

where $\nu_j = n_j/n_T$ and $\Sigma n_j = 1$. Then the system of equations represented by (2.3) becomes

$$\begin{aligned} DF^0 &= -\sigma_{01}F^0 + \sigma_{10}F^+ \\ DF^+ &= -\sigma_{10}F^+ + \sigma_{01}F^0 \end{aligned} \tag{2.5}$$

where the symbol D is the differential operator d/dπ. An additional equation is

$$F^+ + F^o = 1. \tag{2.6}$$

In the likely event of interactions between discrete energy levels of the reactants, the definitions of fractions and cross sections in (2.5) should be extended. For example, electron capture by a proton from a ground state sodium atom can be denoted by ${}_{10}^{1}\sigma_{01}^{n}$ or ${}_{10}^{3s}\sigma_{01}^{n}$ where the resulting hydrogen atom has its electron in level n. If the atomic state is the metastable $2S_{\frac{1}{2}}$ level, this cross section becomes ${}_{10}^{3s}\sigma_{01}^{2s}$. In the same way, the fraction of metastable atoms is F^o_{2S}. In order to recover Equation (2.4) for this more detailed case, the following new relationships are needed:

$$\begin{aligned} F^o &= \Sigma_s F_s^o \\ {}_{1g}\sigma_{0h} &= \Sigma_{t,s} {}^{t}_{s}\sigma_{1g\,0h} \\ {}_{0g}\sigma_{1h} &= \Sigma_{t,s} F_s^o \; {}^{t}_{s}\sigma_{0g\,1h} / \Sigma_s F_s^o \end{aligned} \tag{2.7}$$

Since it is much more difficult to remove two electrons from an alkali than one (the valence electron), Equation (2.5) should simplify. The target will probably either neutral or, even less likely, singly ionized. It is expected that (2.5) will reduce to

$$\begin{aligned} \sigma_{10} &= {}_{10}\sigma_{01} \\ \sigma_{01} &= \nu_o \left\{ {}_{00}\sigma_{10} + {}_{00}\sigma_{11} \right\} + \nu_1 \left\{ {}_{01}\sigma_{10} + {}_{01}\sigma_{11} \right\} \quad \nu_o \gg \nu_1 \end{aligned} \tag{2.8}$$

where the cross section and the reactions with alkali target X are

$$
\begin{aligned}
&p + X \rightarrow H + X^{+}({}_{10}\sigma_{01}) && \text{[charge exchange]}\\
&H + X \rightarrow p + X + e({}_{00}\sigma_{10}) && \text{[stripping]}\\
&H + X \rightarrow p + X^{+} + 2e({}_{00}\sigma_{11}) && \text{[ionization]}\\
&H + X^{+} \rightarrow p + X\ ({}_{01}\sigma_{10}) && \text{[charge exchange]}\\
&H + X^{+} \rightarrow p + X^{+} + e({}_{01}\sigma_{11}) && \text{[stripping]}\ .
\end{aligned}
\tag{2.9}
$$

Since the X^{+} concentration is expected to be very small, the latter two reactions should be negligible. The second of (2.8) will then just depend on ${}_{00}\sigma_{10}$ and ${}_{00}\sigma_{11}$.

Equation (2.5) can be solved by introducing (2.6). The resulting first order differential equations can be readily integrated. The integration constants are evaluated by imposing the proper boundary conditions. In this work there are collisions with the ambient background gas. These produce a mixture of ions and neutrals impinging on the target region. The boundary conditions are

$$
\begin{aligned}
F^{+}(0) &= 1 - \delta\\
F^{o}(0) &= \delta\ .
\end{aligned}
\tag{2.10}
$$

In this case the solutions to (2.5) become

$$
\begin{aligned}
F^{+}(\pi) &= \left[\frac{\sigma_{10}}{\sigma_{10}+\sigma_{01}} - \delta\right] e^{-(\sigma_{10}+\sigma_{01})\pi} + \frac{\sigma_{01}}{\sigma_{10}+\sigma_{01}}\\
F^{o}(\pi) &= \left(\frac{\sigma_{10}}{\sigma_{10}+\sigma_{01}}\right)\left[1 - e^{-(\sigma_{10}+\sigma_{01})\pi}\right] + \delta
\end{aligned}
\tag{2.11}
$$

Here

$$
\pi\sigma = \sigma\int_{-\infty}^{\infty} d\pi \equiv n\ell\sigma \tag{2.12}
$$

where ℓ is the total length of the target region. The average density is simply n. The usual experimental condition is thought to be a pure

proton beam incident on the target material. In that case δ is zero and Equation (2.11) simplifies.

There are two limiting forms for (2.11). One is the "linear" approximation for π small. The other is the high density "asymptotic" value. These are

$$\left.\begin{aligned} F^{+}(\pi) &= 1 - \delta - \sigma_{10}\left[1 - \delta\left(\frac{\sigma_{10}+\sigma_{01}}{\sigma_{10}}\right)\right]\pi \\ F^{o}(\pi) &= \sigma_{10}\left[1 - \delta\left(\frac{\sigma_{10}+\sigma_{01}}{\sigma_{10}}\right)\right]\pi + \delta \end{aligned}\right\} \pi \ll 1 \qquad (2.13)$$

and

$$\begin{aligned} F^{+}(\infty) &= \frac{\sigma_{01}}{\sigma_{10}+\sigma_{01}} \\ F^{o}(\infty) &= \frac{\sigma_{10}}{\sigma_{10}+\sigma_{01}} \quad . \end{aligned} \qquad (2.14)$$

The thick target values of (2.14) are independent of the initial neutral concentration (δ). The linear region depends on both δ and the asymptote (F^{o}_{∞}). Again the standard pure proton beam expressions may be recovered by setting the initial fraction to zero. In this work the neutral fraction (F^{o}) is measured as a function of alkali density. The asymptotic value (2.14) can be used in conjunction with Equation (2.13) to determine the cross sections in this two state approximation. The slope, the intercept, and the asymptotic values of (2.11) must all be measured as a function of energy before σ_{10} can be known.

It is important to note the convention followed here: calculated cross sections will be denoted by Q but experimental ones by σ. Later, attempts will be made to match theoretical cross sections (Qs) with the measured values. For example, σ_{10} will be compared with ${}_{10}Q_{01}$. In this part of the theory section σ was used with the reactions. Explicit

values - cross sections calculated according to some theory - will be labeled Q. They so appear in the figures that follow the appendices.

2.3. Theoretical Descriptions of $\sigma_{10\ 01}$ as a Function of Energy

2.3.1. Introduction

The interactions among an alkali core, a proton, and the valence electron are too complex to be calculated exactly. In general three body problems are beyond the capabilities of physics. Three useful approximations will be made for the proton to neutral cross section. The first is rather qualitative. It is Massey's adiabatic criterion.[6] The other two are much more detailed. One is based on the Born approximation. The other is the classical calculation done by Gryzinski.

2.3.2. The Adiabatic Criterion

For simplicity let the target atom be at rest. If the beam particle passes it very slowly, the electron cloud can adiabatically adjust to the moving charge. If it passes very rapidly, the cloud cannot respond. For the proper range of speeds the electron will be able to attach itself to either charge center. The wave function will be a mixture of proton and alkali core wave functions. Here the probability of capture by the proton becomes large. Qualitatively then, the cross section for electron capture by the proton will be small for both large and small velocities. It will reach a maximum at the characteristic velocity v_{max}.

Whenever the period corresponding to the energy difference between the two atoms at infinite separation (the energy defect) becomes comparable to the transit time of the beam particle, the cross section is a maximum. This time (τ) is given by

$$\tau = \frac{a}{v_{max}} \qquad (2.15)$$

where a is a characteristic dimension of the system. It is a few angstroms. Then the expression for v_{max} is

$$v_{max} = \frac{|\Delta E| a}{h} \quad . \qquad (2.16)$$

Hasted[8] has investigated this quantity for a variety of charge exchange reactions. He has deduced a typical value for a of 8Å for capture into the ground state. The energy defect for capture into the second hydrogen level is about one electron volt (1.6 (-12) erg). Thus $v_{max} \sim 2.0\ (7)$ cm sec^{-1}. For a proton this corresponds to 200 eV. It will be seen later that Gryzinski values peak near 1 keV. (See Table 2.1)

2.3.3. The Born Approximation

Early work on electron capture by Oppenheimer[47] and Brinkman and Kramers[48] was shown to have omitted an interaction term.[49] Whenever this term was added, the resulting cross sections were too low.[50] The treatment was extended to include capture into excited states.[5] Jackson and Schiff[51] used the Born approximation for their calculations. They were able to relate their results to the OBK approximation. Bates and Dalgarno[9] applied this correction to their OBK calculations. They presented explicit forms for capture into the first four hydrogenic levels. The target atoms were also hydrogen-like. The captured electron came from the 1S, 2S or 2P states. These calculations have been extended for capture into the first fifteen levels.[52]

Consider the collision of a proton and a target atom. The electron is initially attached to charge Z_e in state n_i. It is captured into hydrogen state n_f. The cross section for capture from the state

with principal quantum number n_i and azimuthal quantum number l_i into the hydrogen state characterized by n_f and l_f is[9]

$$Q(n_i l_i - n_f l_f) = \frac{\pi a_o^2}{p^2} C(n_i l_i - n_f l_f) \int_x^\infty F(n_i l_i - n_f l_f)\, dx \qquad (2.17)$$

where

$$p = m v_i \hbar / a_o$$

$$x = \{p^2 + (a+b)^2\}\{p^2 + (a-b)^2\} / 4p^2$$

$$a = Z_e / n_i$$

$$b = 1 / n_f$$

a_o = first Bohr radius

C = constant

F = polynomial in x^{-1}

Jackson and Schiff[51] deduced the following correction term for a collision between normal hydrogen atoms (1S) and protons:

$$T = \frac{1}{192}\left(127+56p^{-2}+32p^{-4}\right)$$

$$\frac{-\text{Arctan}\{p/2\}}{48p}\left(83+60p^{-2}+32p^{-4}\right)$$

$$+\frac{\left[\text{Arctan}\{p/2\}\right]^2}{24p^2}\left(31+32p^{-2}+16p^{-4}\right) \qquad (2.18)$$

For a proton probe the energy in keV is $24.97\ p^2$.

For a metastable-like target the constants and functions will be rewritten as

$$\begin{aligned} C(2s-n_f l_f) &= 2^{-3}\, C(1s-n_f l_f) \\ C(2p-n_f l_f) &= 2^{-3}3^{-1}\, C(1s-n_f l_f)\, Z_e^2 \\ F(2s-n_f l_f) &= x^{-2}(x-2a^2)^2\, F(1s-n_f l_f) \\ F(2p-n_f l_f) &= x^{-2}(x-a^2)^2\, F(1s-n_f l_f) \end{aligned} \qquad (2.19)$$

For computational purposes it is somewhat better to change variables. The transformations are

$$\begin{aligned} x^{-1} &\rightarrow z \\ F(x) &\rightarrow G(z)/z^2 \end{aligned} \qquad (2.20)$$

Then Equation (2.17) becomes

$$Q_{BD}(n_i l_i - n_f l_f) = \frac{\pi a_o^2}{p^2} C(n_i l_i - n_f l_f) \int_0^{1/x} G_1(n_i l_i - n_f l_f)\, dz \qquad (2.21)$$

A few constants and functions are

$$C(1S\text{-}1S) = 2^8 Z_e^5$$

$$C(1S\text{-}2S) = 2^5 Z_e^5$$

$$C(1S\text{-}2P) = 2^5 Z_e^5 \qquad (2.22)$$

$$G(1S\text{-}1S) = z^4$$

$$G(1S\text{-}2S) = z^4(1-2b^2z)^2$$

$$G(1S\text{-}2P) = z^5(1-b^2z)^2$$

$$G(1S\text{-}2P) = z^5(1-b^2z)$$

$$G(2S\text{-}n_f l_f) = (1-2a^2z)^2 G(1S\text{-}n_f l_f)$$

In order to simulate electron capture from a ground state alkali target, $Q(2S\text{-}n_f l_f)$ is computed for an effective charge Z_e. This is chosen such that the binding energy of the alkali becomes that of a hydrogen-like 2S state. For potassium the effective charge is 1.130 times the proton charge. For sodium it is 1.229. As a first order

calculation then, assume the correction term [Equation (2.18)] is the same irrespective of initial and final states and charge Z_e. The charge exchange cross sections are shown in Figures 2-1 and 2-2. These Born calculations indicate that capture into the first excited hydrogen level dominates ground state transfer.

Butler, May and Johnston[53-56] have calculated cross sections for charge exchange between protons and ground state hydrogen atoms. They use the Born approximations, too. Their approximate cross sections for hydrogen excitation are also very large. About one half of all excited atoms will be present in the n = 2 level. Their cross sections peak near 17 keV.

2.3.4. Gryzinski Theory

The third approximation is the classical mechanics calculation of Gryzinski.[36-38] This allows cross sections to be calculated easily as a function of beam energy and readily compared with experiment. The shapes of these cross sections are in good agreement with this experiment.

The theory is extended slightly by allowing capture into all excited hydrogen states. To keep the total cross section finite the states are <u>not</u> weighted according to their total degeneracies. The ground state has been excluded from this calculation. Whenever the cross section is pathological - as it is for ground state capture - it should be calculated by detailed balancing.[40] In that case the contribution from the ground state is orders of magnitude less than that of the first excited state. Accordingly it is neglected throughout. It is also assumed that the substates are populated according to their statistical weights. This assumption is unverified.

In order to compute the total cross section for electron capture by the proton into all excited hydrogen levels, a summation of individual level contributions is performed (2.26). This can be approximated by an integral for sufficiently large principal quantum number n. It will be shown later how small n can be for this approximation to be valid. The total cross section is then a discrete sum over the first m excited states plus an integral correction term (2.29).

2.4. Calculation of the Total Cross Section

2.4.1. Calculation of $_{10}\sigma_{01}$

The reaction to be studied is a variant of (2.1). It is the simple charge exchange process

$$B^+ + A \rightarrow B + A^+ \quad (_{10}\sigma_{01}) \quad . \tag{2.23}$$

In order for capture to occur the electron must gain an energy corresponding to the beam velocity plus the difference in binding energies to A and B. An upper limit of the energy change is given by the translational energy plus the binding energy of the final state. Thus according to Gryzinski theory[38] a cross section will have the form

$$Q \simeq \int_{\frac{1}{2}m v_{B^+}^2 + U_i^A - U_i^B}^{\frac{1}{2}m v_{B^+}^2 + U_i^A + U_i^B} \sigma_{\Delta E} \, d(\Delta E) \tag{2.24}$$

Further the average energy of the electron bound to A will be approximately $\bar{E}_e^A \sim U_i^A$. The quantity $\sigma_{\Delta E}$ is approximately

$$\sigma_{\Delta E} = \frac{\sigma_o}{(\Delta E)^2} \frac{f_v}{U_i^A} \tag{2.25}$$

where σ_o = constant (6.56×10^{-14} eV^2 cm^2)

U_i^A = potential energy of electron bound to A

ΔE = energy change of the electron in going from A to B

$$f_v = \left(\frac{v_e}{v_{B^+}}\right)^2 \left(\frac{v_{B^+}^2}{v_{B^+}^2 + v_e^2}\right)^{3/2}$$

In performing the integration f_v is essentially constant so that Equation (2.24) becomes

$$_{10}Q_{01}(m) = \frac{2\sigma_o}{(U_i^A)^2} U_{HA}(m) \frac{\left(\frac{V^2}{1+V^2}\right)^{3/2} V^{-2}}{\left[1+V^2\right]^2 - U_{HA}(m)^2} \tag{2.26}$$

where Q(m) = cross section for capture into the m^{th} hydrogen level

$$U_{HA}(m) = \frac{U_i^B}{U_i^A} = \frac{13.6/m^2}{U_i^A}$$

$$V = \frac{v_{B^+}}{v_i^A}$$

An estimate on the maximum value for this cross section is Equation (4.1) of Reference 38:

$$Q_{max} \simeq \pi a_o^2 \left(\frac{r_a}{a_o} + 2 \frac{U_i^H}{U_i^A} Z_{B^+} \right)^2 \qquad (2.27)$$

where a_o is the first Bohr radius

Z_{B^+} is the beam particle charge

r_a is the amplitude of oscillation of the target electron

U_i^H is the ionization potential of hydrogen (13.6 eV).

These maxima are listed in Table 2.1.

The summation of these cross sections is performed in the above mentioned manner. The integration becomes

$$Q_S = \frac{\alpha}{2} \int_{\beta}^{\infty} \frac{X^2 \, dX}{X^4 - \beta^4} \qquad (2.28)$$

where

$$\alpha = \frac{27.2 \, \sigma_o}{(U_i^A)^3} \frac{f_v}{(1+V^2)^2}$$

$$\beta = \left[\frac{13.6}{U_i^A (1+V^2)^2} \right]^{1/2}$$

It becomes then

$$Q_S = \lim_{X_u \to \infty} \left\{ -\frac{\alpha}{4\beta} \ln\left|X+\beta\right| + \frac{\alpha}{4\beta} \ln\left|X-\beta\right| + \frac{\alpha}{2\beta} \operatorname{Arctan}\left(\frac{X}{\beta}\right) \right\} \Bigg|_{X_\ell}^{X_u} . \quad (2.29)$$

The total cross section thus is

$$Q = \sum_{m=n_0}^{n-1} Q(m) + \frac{\alpha}{\beta}\left[\frac{\pi}{2} - \operatorname{Arctan}\left\{\frac{n}{\beta}\right\} - \frac{1}{4}\ln\left|\frac{n+\beta}{n-\beta}\right|\right]. \quad (2.30)$$

This is the summation over n-2 excited states (Equation (2.26)) and the evaluation of (2.29) for $X_\ell = n$.

It should be noticed that Q(m) as given by Equation (2.26) is proportional to m^{-2} for large m. The quantum calculations are instead proportional to the inverse cube.[9,46,48] The Born results further show that the high angular momentum states are not populated. S state capture predominates for both fast ($E \gg 25$ keV) and slow ($E \ll 25$ keV) protons.[9,47,51] High velocity proton impacts on carbon foils produce an enhanced 2S population[34] in accord with these calculations. May[56] and others[9] have shown for proton-hydrogen atom exchange this no longer holds for medium energy ($E \approx 25$ keV). At 25 keV more than 50 per cent of the

captures will be into the $\ell = 1$ state. Only about one quarter are S state captures[54,56] as shown in Figure 2-3.

Figure 2-4 shows the sum of a few discrete level cross sections ($\underline{Q(m)s}$) for electron capture from potassium. It should be noted that about one half of the total contributions to the cross section come from the first excited state. If the magnetic substates are statistically populated, then approximately ten per cent of the resulting excited level cross section comes from the metastable 2S state. Also the rapid convergence of the cross sections is easily seen.

Equation (2.30) has been compared with the discrete summation of (2.26) for 200 levels. It was found that for most cases n = 11 is a satisfactory lower limit for the integral. Figures 2-5 - 2-6 show the theoretical cross sections for various alkali atoms. The predicted ratio of metastables to total hydrogen atoms is also shown in Figure 2-7.

2.4.2. Calculation of $_{01}\sigma_{10}$

It was disclosed in the preceding subsection that the neutralized probe particle will possess internal excitation. Thus the calculation of the subsequent electron loss by this fast probe is more complicated than that of Section 2.4.1. The charge exchange reaction is

$$H^{o}(m) + A^{+} \rightarrow p + A^{o}(n)\left(_{01}^{m}\sigma_{10}^{n}\right) \quad . \qquad (2.31)$$

The Gryzinski formalism - Equation (2.26) - becomes

$$ {}_{01}Q_{10}(m,n) = \frac{2\sigma_o}{(U_i^H)^2}\, m^4\, U_{AH}(m,n) \left[\frac{W^2(m)}{1+W^2(m)}\right]^{3/2} $$

$$ \times \frac{W^{-2}(m)}{\left[1+W^2(m)\right]^2 - U_{AH}^2(m,n)} \qquad (2.32) $$

where

$$ U_{AH}(m,n) = \frac{U_i^A(n)}{U_i^H}\, m^2 $$

$$ W^2(m) = \frac{\mathcal{E}_p}{U_i^H}\left(\frac{m_e}{M_p}\right) m^2 = W^2 m^2 . $$

Although the alkali target above becomes the probe and the excited hydrogen atom is its target, the projectile speed remains the proton velocity. Equations (2.26) and (2.32) are identical for that well known alkali, atomic hydrogen.

Equation (2.32) can be rewritten to show explicitly the dependence on the hydrogenic principal quantum number (m) as

$$ {}_{01}Q_{10}(m,n) = \frac{2\sigma_o}{(U_i^H)^2}\, \frac{U_i^A(n)}{U_i^H} \left[\frac{W^2}{W^2+m^{-2}}\right]^{3/2} $$

$$ \times \frac{W^{-2}}{\left[W^2+m^{-2}\right]^2 - \left\{\frac{U_i^A(n)}{U_i^H}\right\}^2} . \qquad (2.33) $$

This becomes for a highly excited atom (large m)

$$ {}_{01}K_{10}(n) = \frac{2\sigma_0}{(U_i^H)^2} \frac{U_i^A(n)}{U_i^H} \quad \frac{W^{-2}}{W^4 - \left\{\frac{U_i^A(n)}{U_i^H}\right\}^2} \qquad (2.34) $$

which is now independent of the hydrogen quantum number. Since $W^2 \sim \mathcal{E}_p/25$ for keV energies, a ten per cent error is made by substituting the asymptotic form (2.34) for the exact Equation (2.33) for m = 7 at 5 keV and m = 3 at 25 keV.

Alkali binding energies do not depend as simply on the principal quantum value as does hydrogen. However they do become hydrogenic for large ℓ-values as the quantum defect vanishes. Later the contributions of alkali electrons more tightly bound than the valence electron will be considered.

It can be seen that the cross sections (Equations (2.26) and (2.33)) possess a pole where their denominators vanish. Naturally the results there are unreliable. Garcia, Gerjuoy and Welker[40] discuss this and decide upon a useful change in the formalism. Whenever the limits of (2.24) allow this tangent-like discontinuity, just apply detailed balancing to calculate the offending cross section from the one corresponding to the reverse reaction. For example, ${}_{10}\sigma_{01}$ for the creation of ground state hydrogen is computed this way from ${}_{01}\sigma_{10}$. Their prescription becomes

$$ \sigma_{08}(E) = {}_{ab}\sigma_{cd}(E) = \frac{\omega_f}{\omega_i} {}_{cd}\sigma_{ab}(E) \qquad (2.35) $$

where ω_i and ω_f are the statistical weights of the initial and final states of the original cross section. For a proton and the valence electron of an alkali these weights are the same. For inner shell electron exchange they are not. Since half of the target atoms will have their electrons wrongly oriented for capture, the reverse cross section is divided by two. In Gryzinski theory the total cross section of a state with energy E is the number of "equivalent" electrons with that binding energy times the cross section of a single electron with energy E.

2.5. Predicted Background Lyman Alpha Signal

One of the aims of this experiment is to determine the metastable hydrogen (2S) population resulting from the charge exchange reactions. This is done by applying an electric field to the neutrals and observing Lyman alpha radiation. This mechanism is dealt with in Appendix C. It is known from the preceding sections that all excited hydrogen levels will be populated. Consequently there will be background radiation from the natural decay of highly excited levels.

Since the hydrogen beam is optically thin (the density is about 10^5 cm^{-3}), photon excitations can be neglected. Only the Einstein A coefficients are needed. The population of the i^{th} sublevel obeys the equation

$$\frac{dN_i}{dt} = -N_i \Sigma_j k(i,j) + \Sigma_j N_j k(j,i) \qquad (2.36)$$

where the loss terms are transitions into lower lying levels and the source terms are transitions down into this level from all of the j^{th} levels possible. The k's are just the Einstein A coefficients. They are tablulated in many places.[60,102] To solve (2.40) assume $N_i(t)$ is given by

$$N_i(t) = \sum_j C(i,j)\, e^{-\nu_j t} \tag{2.37}$$

where

$$\nu_i = \sum_j k(i,j)$$

$$k(i,j) = 0 \quad \text{for } j \geq i$$

and C(i,j) is the coefficient linking states i and j.
When this form is put into Equation (2.40) and the various exponentials are equated, the coefficients are seen to be

$$C(i,j) = \frac{\sum_\ell C(\ell,j)\, k(\ell,i)}{\nu_i - \nu_j} \qquad i \neq j$$

$$C(i,i) = N_i(0) - \sum_\ell C(i,\ell) \qquad i = j \tag{2.38}$$

where $N_i(0)$ is the initial population of the i^{th} state.

This system of coupled differential equations represented by (2.36) is solved for each time t by substituting for the populations of the higher levels. Such a repetitive procedure can be done easily on a large computer such as the IBM 7090. The number of levels that must be considered becomes quite large. For the n^{th} state there are n sublevels. For n states the number of equations is n(n+1)/2. For 10 states there

are two 55 x 55 matrices to be manipulated. For twelve levels they are 78 x 78. However for 20 states these matrices are 210 x 210 which far exceeds the memory size of the 7090. Further, the running time of the calculation goes as n^2. In order to minimize the errors in neglecting higher levels but to keep reasonable computing time, these coupled equations were solved for a varying number of levels. 10 levels is a good compromise.

The physics of this problem is in the initial population of these levels. Gryzinski results from Section 2.4 were used for this purpose. Two different models were used: (1) the sublevels were populated according to their statistical weights (2j+1); and (2) only the S sublevels were filled. The results of these calculations are displayed in Figures 2-8 and 2-9.

2.6. Projected Lyman Alpha Signal

Lyman alpha radiation is "seen" by the UV detector which will be described more completely in Section 3.5. The hydrogen beam passes beneath it and emits background radiation. This comes from the cascade of highly excited states mentioned previously. In order to detect metastable 2S atoms a strong electric field is applied across the beam path. Stark effect mixing of the metastable and resonance levels allows depletion of the 2S state. The transition probability of the "metastable" state is a function of the electric field intensity. Because of the high velocity of the atoms, a very intense high electric field is needed to quench the 2S state within some reasonable distance of the detector. The

field is too strong for the Bethe approximation[57] - Equation (2.39) - to be valid

$$\frac{1}{\tau} = 2780\ E^2 \qquad (2.39)$$

where τ is the lifetime in seconds and E is the field strength measured in volts cm^{-1}.

Equation (2.43) fails for very weak as well as very strong fields. The natural two photon radiative lifetime of one-seventh of a second[58,59] sets a upper limit. The lower limit to the lifetime is the resonance value of 1.6 nsec.[60] The calculations of Appendix C yield the lifetime of the metastable state for the entire range of fields that will be encountered normally. For more details see Appendix C (lifetime calculation) and Appendix D (field configuration).

The UV signal received depends primarily upon the metastable population, the geometry, and the efficiency of the detector and the electronics. Supposedly the geometry is known. Detector response is rather uncertain. It will be necessary to calibrate carefully and thoughtfully.

Since the metastable state can be populated either by direct interchange into the state (the $\mathcal{S}$ channel) or by cascase from higher states (the $\mathcal{C}$ channel), the beam energy enters into the population in two ways. The cross sections are energy dependent. But, in addition, the transit time from the oven to the detector depends on the square root of the energy. The slower the beam, the more cascades occur. The distance between the oven and the UV detector is 40 cm. Figure 2-10 shows the expected ratio of metastable atoms to all atoms as a function of beam energy. Figures 2-7 show the initial ratio for various targets.

3.0. APPARATUS

3.1. Source and Ion Selector

Figure 3-1 is a sketch of the apparatus. The ion source is a commercial Duo-Plasmatron type[61] which is capable of supplying several millamperes of ion current. High purity hydrogen gas is bled into the top of the source through a needle valve. No trapping of impurities is done in the gas line since the source operates with the relatively high pressure of 200 to 500 microns. Electrons are liberated from a number 80 mesh filament. To lower the work function of this 90% rhodium - 10% platinum filament the mesh is coated with a commercial oxide mixture.[62] Typical operating conditions for this filament are 6 volts AC and fifteen to twenty amperes.

These electrons spiral in the field of a small electromagnet. The poles of the magnet surround two sides of the source. It is clamped to the three topmost plates. To minimize arcing problems between the magnet and the source body the DC supply of the electromagnet is grounded to the cathode. The field is variable.

The ions sit in a conical well until they are extracted through a 30 mil hole in the apex. Pumping holes are drilled into the sides of the extraction cup located directly below the well. The current drawn by this extraction process varies between 1.0 and 3.0 amperes. In order to maximize the ion yield both this DC current and that of the magnet are varied. In general low currents give the largest yield for low energy ions whereas high energy ions require high arc and magnet currents. The

ions are accelerated through a high DC potential. This can be varied from 0 through 30 kilovolts.

After leaving this middle portion of the source, the ions are focussed by an electrostatic lens in the base of the source. The potentials have been arranged so that the base plate, which is the third element of the lens, is at ground potential. This requires that the cathode be kept at the variable negative high voltage. As a result there is no defocussing of the beam as it enters the grounded magnet chamber.

This brass magnet chamber sits between the poles of a large electromagnet. Typically the field was ~200 Oe. The magnet runs on highly regulated direct current. In order to exit this chamber the ion beam must be bent through a 30 degree angle along a 15 inch radius. Any one of the three major ions produced by the high pressure source can be selected. In addition to creating protons and ionized molecular hydrogen, the source also produces the H_3^+ ion in vast quantities. These three ions are generated in approximately equal numbers.

To decrease the pumping load on the exchange chamber pump, the magnet chamber has its own diffusion pump. It is an air-cooled two inch pump manufactured by the Veeco Vacuum Company and rated at 80 liters per second. The pump fluid is Dow Corning DC 704 silicon fluid. This pump can be valved off from the magnet chamber by a small two inch gate valve. With this pump in operation the gas pressure under normal gas load is 2×10^{-4} Torr.

Normally the ions emerging from the magnet chamber are protons. These ions are refocussed by an external einsel lens located between the magnet chamber and the exchange chamber. The two outermost elements of

the lens are at ground potential. The middle element potential varies from 0 to 6 kV DC.

3.2 The Charge Exchange Chamber

The charge exchange chamber is a cylinder 16 inches high and 10 inches in diameter. This stainless steel chamber has four equally spaced two inch long arms welded halfway up the sides of the chamber. The beam enters and leaves through two opposite arms. Below it hang a water baffle and a ten inch water-cooled diffusion pump. This pump, which is made by Consolidated Vacuum Corp. (CVC), is rated at 4400 liters per second (unbaffled). It operates on 220 Volts 3 phase. Its pumping fluid is also the low pressure DC 704. Typical operating pressures under gas load are 8 to 15 x 10^{-5} Torr with the magnet chamber pump operating. The pressure doubles whenever the small pump is valved off. Normal condensible and alkali vapor trapping is done by a large cylindrical copper shield. It surrounds five sides of the oven. It is connected to a liquid nitrogen reservoir by a one inch diameter copper bar. Holes in the shield allow passage of the ion beam. The background pressure for no gas load but a cold nitrogen shield is 5 x 10^{-7} Torr. There is a viewing port in the top of the chamber which allows observation of the space between the shield and the front of the oven.

3.3. The Oven

The oven is made of Monel and has a rectangular base with a one half inch diameter tube projecting symmetrically along the beam axis. Flanges are attached to the ends of the tube. A plate is bolted to each

flange with 6-32 stainless steel screws. A metal O-ring seals the plate-flange connection. Apertures drilled into the plates collimate the beam. The total length of the arms including the plates is 16 cm.

The target metal is slid along the arm into a well drilled into the rectangular base. The oven is heated by two sets of independently controlled heaters. One pair is mounted in the base and supplies most of the heat for the oven. A secondary set is strapped to the arms. This pair keeps the arms at a uniform temperature. At night they maintain the arms at a higher temperature than the well. This insures that no alkali is deposited in the arms between runs. The main heaters maintain good thermal contact with the base. They fit snugly into the base. Small screws press them against the sides of the holes.

Four chromel-alumel thermocouples monitor the oven temperature. One junction in the base senses the well temperature. A second is screwed to the top of the tube directly above the well. A third one is attached to the "downstream" plate on the arm. The fourth is located on the arm midway between the last two. The thermal E.M.F. is balanced against a standard voltage in a bridge circuit that uses a small, relatively insensitive galvanometer as the nulling device. Typical voltages are a few millivolts.

The oven itself sits on three sharpened screws embedded in a hanging platform. A bellows system and three external screws allow spatial orientation of this platform. In addition it may be slightly rotated about the beam axis by means of adjustment screws which push against arms attached to the top plate of the bellows system. A hollow stainless steel pipe passing through the top plate supports the platform.

It is now capped but could be used to supply gas to a standard gas target cell should that be necessary.

3.4. The Detection Chamber

Between the exchange and detection chambers is a valve, a bellows assembly, and a vacuum separator. The bellows allows the detector chamber to be translated normal to the beam. The valve is also a CVC 2 inch gate valve. The separator is a brass plate with a 3/8 inch diameter hole drilled in the center. The detector chamber is identical to the exchange chamber. It is pumped by a 6 inch CVC water-cooled oil diffusion pump. The unbaffled pumping speed is 1400 liters per second. It runs on single phase 110 V alternating current. The fluid was initially DC 704 fluid but later Convalex 10 was used. This pump has a CVC liquid nitrogen trap. A single filling of nitrogen lasts for approximately 4 hours. A typical background pressure is 3×10^{-7} Torr for the chamber valved off. Whenever the connection is made with the exchange chamber, it rises to 5×10^{-7} Torr. Capacitor plates in the entrance arm are used to sweep the ions from the neutral beam path.

3.5. The Detectors

Two major detectors hang in this chamber. They are the ion detector and the Lyman alpha UV counter. The ion detector consists of a thermocouple foil mounted inside a protecting Faraday cup. A grid, which is 90% transparent, is negatively biased to reject secondary electrons. In addition the Faraday cup guard, the cup itself and the foil can all be biased positively. These features are shown in Figure 3-2.

The thermocouple is a 1 mil thick Nichrome foil. It is sandwiched between 1½ inch diameter rings. Three rings are copper; the fourth ring in front is boron nitride. The heating effect of a particle striking the foil is independent of its charge. Hence the foil can be used to monitor neutral atoms. It is calibrated against the proton beam by varying the beam current and noting the deflection on a nulling galvanometer. This meter is part of a bridge circuit. Its standard voltage is supplied by a mercury reference cell and a resistor string. The voltage drops have been arranged in multiples of two for convenience. The thermal E.M.F. is a few microvolts.

The junction is formed by contact between the foil and a small copper wire soldered to the back of the foil. Current is drawn off through a larger wire attached to the rings. The foil also integrates beam fluctuations. It has a thermal time constant of 4 seconds.

A bellows system allows this detector to move in 3 dimensions. Also the detector can be rotated through a slight angle (about 10°) in the same manner as the oven.

The UV detector, however, is fixed in space. It hangs on a bar from the top plate of the chamber. The clamps that secure it to the bar allow the detector to be repositioned somewhat. These clamps are not accessible when the plate is bolted in place. Adjustments can only be done whenever the chamber is open to the air.

This detector is a modified Fite and Brackmann[63] counter. It is a cylindrical Geiger tube filled with a few crystals of iodine and argon buffer gas. Constant iodine pressure is maintained by water cooling the tube. A positive high voltage terminal collects electrons liberated whenever a UV photon ionizes the iodine. The relevant reactions are

$$h\nu + I_2 \rightarrow I_2^+ + e \qquad \text{(photoionization)} \qquad (3.1)$$

$$e + X \rightarrow 2e + X^+ \qquad \text{(cascade)} \qquad (3.2)$$

$$e + I_2 \rightarrow I + I^- \qquad \text{(quench)} \qquad (3.3)$$

where X is the inert buffer gas. Here it is argon. The threshold for reaction (3.1) is about 9.7 eV (1270 Å). An oxygen cell ahead of the detector limits the wavelengths that can enter the counter. Oxygen has 7 well known UV "windows".[64] One such absorption minimum occurs at the wavelength of Lyman alpha (1216 Å). More will be said about this molecular oxygen filter later. A lithium fluoride crystal[65] seals the counter. This single crystal is one inch in diameter and one-sixteenth inch thick. Lithium fluoride has a short wavelength cutoff of 1080 Å which corresponds to 11.4 eV.[63]

The filter is a chamber with a lithium fluoride crystal in front and an O-ring groove in back. A good vacuum seal obviates the need for an additional piece of LiF. Screws fasten the cell to the face of the detector. Oxygen flows through the chamber to prevent ozone[66] build-up. Since water vapor also has an extremely large cross section for Lyman alpha,[67] the gas is dried by passing it through a dry ice-acetone trap.

A light baffle is mounted in front of the oxygen filter. The solid angle subtended by the detector ($d\Omega$) is $4\pi/333$. Two wires hang astride the beam path. Whenever high voltage is applied to these wires, the quenching electric field is created. This is treated in detail in Appendix D. The counter then observes part of the radiation. Figure 3-3 is a schematic representation of the detector and its electronics.

3.6. The Calibrators

Initially the UV counter was calibrated by means of a radioactive source. It was swung into position directly below the detector. After each data point was taken, the source was moved into place. The counting rates for that day's run were then normalized using these calibrations. Since there was so much uncertainty in the counter efficiency, an in situ calibration was attempted.

In order to calibrate the UV detector its response to a known reaction is determined. Fite and Brackmann[32] measured the cross section for

$$e + H_2 \rightarrow \text{countable UV} \quad . \tag{3.4}$$

It peaks at about 100 eV at 1.6 (-17) cm^2 and decreases monotonically. A modified Pierce gun was built from commercially available parts. Its prototype is described elsewhere.[68] Normally the electron current to the Faraday cup (the electron trap) was about 1% of that drawn from the filament. It was possible to have currents on the order of 100 μA in a 1 cm spot for calibration. This gun is shown in Figure 3-4.

The gun filament was a strip of pure tungsten sheet 1 mil thick cathode and 1/16 inch wide. It was maintained below the ground potential of the second anode accelerating plate. The first plate was operated near the filament. The electrons then fell through a total potential of a few hundred volts. The beam is focussed by a three element lens. This consists of the second plate, a short cylinder at several tens of volts, and a flat sheet with a large (1/8 inch) aperture kept at ground potential. The ion beams pass through a gap of several centimeters between this plate and the Faraday cup guard. The guard is also grounded. The electron

trap is a 3 cm long cylinder closed at one end. To prevent electron reflection from this cup, wire is coiled inside the trap and it is biased slightly above ground. Typical operating voltages on these various gun members are $V \sim -150$, $V_2 \sim -150$, $V_3 \sim 0$, $V_4 \sim -60$ and $V_5 \sim -60$. Both the last element of the lens (V_6) and the trap guard (V_7) are grounded. The trap itself (V_8) is ~2 volts. All of these parts are mounted on two long ceramic rods which are not included in Figure 3-4.

These rods fit into two aluminum holders. These disks in turn fit on vertical threaded rods. The holders are held in place by ordinary nuts. The rods screw into a hanger which straddles the UV detector. The gun can thus be oriented in space. Again these adjustments can be performed only when the top plate is unbolted. Since the gun was to be used only as a calibration device, no effort was expended in trying to make it monoenergetic. The energy spread is consequently rather large, about 1 eV.

3.7. Electronics

The temperature of four locations in the oven is measured by Chromel-Alumel thermocouples. Each one forms one arm of a standard bridge circuit. The oven monitors pass through an octal vacuum feed-through. An eight wire cable runs to a Leeds and Northrup thermocouple switch. This special switch alternately selects the junction to be nulled. No reference junction is used. The various solder connections at room temperature serve this purpose. Since the room temperature varies much less than 1°F, it is much more constant than a naive, unprotected water-ice system would be. The thermocouples are calibrated against several

standard points. Since some of these points are below room temperature (about 70°F), the reference battery (a "D" cell) has a polarity reversal switch.

Five standard temperatures are used. They are (1) the boiling point of nitrogen, (2) carbon dioxide sublimation point, (3) the ice point, (4) the water-steam point, and (5) the melting point of lead. These values are listed in Table 3.1.

It can be shown that[70]

$$\frac{d^2\mathcal{E}}{dT^2} = -\frac{\tau}{T} \tag{3.6}$$

where τ is the Thompson coefficient,

T is the absolute temperature, and

$\mathcal{E}$ is the thermal emf.

The solution to (3.6) is

$$\mathcal{E} = A + BT + CT\,\ell nT \quad . \tag{3.7}$$

In order to reform this into the more familiar parabolic expression, add and subtract the term $CT\ell nT_o$. A power series expansion of this modification of (3.7) is performed. By rearranging and renaming the coefficients the sought-for form appears. The linear form is an excellent approximation for the portion of the calibration curve above the ice point.

The nulling galvanometer for the thermocouples was made by Rubicon Company. Its sensitivity is 4 (-8) A/mm. The foil thermocouple, which is the neutral beam detector, and its associated circuitry is much more sensitive.

The nulling device for the foil is a Leeds and Northrup model 2430A galvanometer with a rated sensitivity of 0.49 μV/mm. To maintain it at a uniform temperature it is kept in a plastic box. Although the metal case around the meter is grounded, additional shielding is provided by wire screening around the box. The time constant of the foil and its circuitry is about 4 seconds.

The neutral detector leads pass through individual ceramic feed-throughs. They terminate in female BNC connectors. The wires to the bridge are RG-58/U coax. The current carrying ring wire is fed to a tee. One branch is connected to the bridge. The other goes to ground through the microammeter. The second lead is fed directly into the bridge.

The standard voltage for the bridge is supplied by a resistor string across a 1.34 V mercury cell. There are 11 taps on this string. The one per cent precision resistors are selected so that the reference voltage varied by factors of two. Thus the minimum voltage is 2^{-11} of the maximum. The fine adjustment resistor is a ten-turn fifty ohm precision potentiometer. A battery reversal switch and an off-on switch complete the controls on the bridge box.

The current meter that monitors the ring wire is an RCA model WV-84C Ultra Sensitive Microammeter. This is battery powered. The meter range is about 2 (-10) to 1 (-3) amperes. Typical currents are a few microamps. The input resistance is high (about 10^9 ohms). A shunt capacitor of a few tenths of a microfarad is sufficient for integrating a noisy signal.

The UV counter is powered by a Fluke 6000 VDC supply. Pulses pass through a high voltage capacitor to a Hewlitt-Packard amplifier M/N

450AR. It has two fixed gains; it can boost the input by either 20 or 40 dB. The amplified pulse is fed to a tee. Part of the signal is displayed on a Dumont oscillograph M/N 304-HR. The rest goes into a Hewlitt-Packard 10,000 count scaler. The model H43-521CR scaler has three fixed sampling times: 1/10, 1 and 10 seconds. In addition the device has a provision for an external gate. By this a sampling time of any desired length can be selected. Data were taken with the 1 second fixed time.

The Duo-Plasmatron ion source is powered by a 30A transformer, a DC power supply capable of delivering a few amperes to the small electromagnet, the arc supply and the voltage source for the einsel lens. The large negative voltage on the filament, the arc and magnet supplies, and the topmost plates of the source are furnished by a Sorensen M/N 1030-20 supply. It provides 30 kV at 15 mA. High voltage isolation transformers allow line voltage to power the two floating supplies safely. The arc supply gives a few hundred volts and up to 3 amps to the source to create the two plasmas (H and H_2) in the extraction cup. The internal einsel lens is powered by a Plastic Capacitors Model HV250-103M 25 kilovolt DC supply. It is rated at 10 mA but the normal load is 1 - 2 mA.

Since the electron source for the Duo-Plasmatron consumes roughly 100 watts, water cooling is needed. A closed water system cools the filament electrodes, the 2 topmost plates of the source, and the middle (ungrounded) element of the einsel lens. Distilled water is circulated by a small pump from a refrigeration unit into demineralizer filters. The chilled, filtered water flows through the hollow source plates.

The electron gun used a plethora of power supplies. The filament is heated by a 25A 28V transformer. Two Kepco Model ABC-400 supplies

bias the cathode and the acceleration plate. Lens potentials are furnished by a 250 VDC Sorensen supply through voltage dividers. Small voltages are provided by batteries.

3.8. Gas Handling System

The hydrogen for the source and calibration target comes from a high purity tank through various valves and runs of copper tubing. Gas goes from the tank through a standard regulator. It is connected to the tubing through a threaded nut and shut-off valve. At a tee the flow branches. It supplies the ion source directly. A valved branch line feeds the calibration target. It has been explained previously how the source cathodes are maintained at high voltage. The gas system is grounded. A length of glass insulates the gas line at the source. It is equipped with O-ring sealed quick-couplers for easy removal. To prevent ionization of the gas the needle valve is at source voltage. This makes gas flow adjustments rather inconvenient while the source is operating. The flow is set before high voltage is applied. The valve and glass assembly is attached to the source through another coupler joint.

Meanwhile gas for the target flows through the valved tee branch to a gas reservoir. This is another stainless steel vacuum chamber. This chamber is 6 inches in diameter and 16 inches tall. It is similar to the exchange and detector chambers in all respects. A 6 inch CVC water-cooled oil diffusion pump evacuates the vessel. It is backed by a Welch M/N 1936 fore pump. A water cooled baffle sits atop the pump stack. Between the baffle and the chamber is a 6 inch gate valve. This

pumping station can clean the gas handling system as well as function as a reservoir for the gas target.

3.9. Vacuum Stands

There are two stands supporting the vacuum chambers. A long, welded, steel table holds all but the reservoir chamber. This vacuum chamber has its own stand. The reservoir bolts directly to its stand. The rectangular top of this table is 16 x 24 inches. The top of the stand is 48 inches above the floor. The pump stack hangs below the chamber. The fore pump is below it. The base of the stand has adjustable feet. The elevation can be changed by several inches. Physically it stands beside the detector chamber at the foot of the long table. A few inches of clearance are provided so that the detector chamber can be moved transverse to the ion beam.

The large table is also adjustable. It is 63" long and 24" wide. Both the exchange and detector chambers roll on rails hung between the side pieces of the table. The 10 inch diffusion pump limits the table height. The fore pump backing this big diffusion pump is also located outside the table. It sits beside the reservoir fore pump in the nook formed by the two stands.

The large electro-magnet is bolted directly to the table. The ion source is clamped to the magnet chamber. However it hangs beyond the back of the table. The entire table is angled into a corner of the room. The source is thus relatively secure from falling bodies.

Sitting inside the side rails of the table are the fore pumps for the magnet and detector chambers. The hydrogen tank is secured to the

front leg of the table. The liquid nitrogen reservoir for the detector chamber juts beyond the table front.

3.10. The Oxygen Filter

At this point it is a good idea to examine in detail the UV counter and its molecular oxygen filter. The detector that was used was a modified Fite and Brackmann (FB) counter.[63] The buffer gas used was one half atmosphere of argon instead of the helium of Reference 63. This design modification of Ott[68,69] produces a good plateau, i.e., the counter sensitivity is essentially independent of applied voltage.

The properties of such a counter were investigated by Fite and others.[63] The angular and radial sensitivity of the original counter design and its temperature dependence have been reported. The lithium fluoride windows have been discussed by Schneider[71] (index of refraction) and Ott[69] (transmission of polarized Lyman alpha radiation).

The transmission of light by molecular oxygen has been studied by many workers.[64,66,72-75] Table 3.2 lists the seven regions of high UV transparency. The shape of the absorption curve near 1216 Å has received much attention. It has been mapped with 0.2 Å resolution. While the results obtained are not identical, they are similar enough to allow a simple approximation to be made for the absorption coefficient as a function of wavelength (See Figure 3-5).

These data[74,75] have been fitted to two low order polynomials. The coefficient doubles within ½Å on the UV side of Lyman alpha but a one angstrom shift towards longer wavelengths is required for the same effect. The polynomial representations are

$$\left.\begin{aligned} \tilde{\lambda} &= \lambda - 1213.3 \\ k(\tilde{\lambda}) &= 1.5233 - 1.8749\,\tilde{\lambda} + 0.6170\,\tilde{\lambda}^2 \end{aligned}\right\} \lambda < 1215.4$$

$$\left.\begin{aligned} \tilde{\lambda} &= \lambda - 1217.3 \\ k(\tilde{\lambda}) &= 0.6406 + 0.2393\,\tilde{\lambda} - 0.03416\,\tilde{\lambda}^2 \\ &\quad + 0.0271\,\tilde{\lambda}^3 + 0.03192\,\tilde{\lambda}^4 \end{aligned}\right\} \quad \lambda > 1215.4 \qquad (3.8)$$

It is an artifact of this model that the coefficient falls below the Lyman alpha value which seems to be the true minimum.[73] Departure from Beer's Law - pressure independence of the absorption coefficient - has been noted.[66,75]

Using the above approximation, one can now calculate the attenuation of the radiation by the oxygen gas. For light incident upon the cell at an angle θ from the perpendicular the transmitted intensity obeys

$$I_\nu = I_o \exp\{-k_\nu x \sec\theta\} \qquad (3.9)$$

where x is the depth of the cell measured in atm-cm and $k\nu$ is the absorption coefficient at frequency ν. For a gas flow system the oxygen pressure must be slightly above atmospheric. Hence x is just the linear dimension.

Whenever a source moves with velocity v with respect to a stationary observer, light emitted at frequency ν_o is seen at the Doppler shifted frequency ν where[76]

$$\nu = \nu_o \gamma(1 - \beta\cos\theta) \qquad (3.10)$$

and

$$\beta = v/c$$

$$\gamma = [1-\beta^2]^{-\frac{1}{2}} \quad .$$

In this work $v/c \approx 1/150$ so that Equation (3.10) can be approximated by

$$\nu = \nu_o(1-\beta\cos\theta) + \tfrac{1}{2}\nu_o\beta^2 \qquad (3.11)$$

where the first term is the classical Doppler shift and the other is called the relativistic shift. This one is always towards the red (longer wavelengths) whereas the classical shift varies from red to blue. Thus the net shift is redward. Since the absorption coefficient curve is also asymmetrical, the strange curves of Figures 3-5 and 3-6 result from Equation (3.9). The parameter for the family of curves is the proton energy in keV.

Since absorption by the oxygen can limit the acceptance angle of the counter more severely than a geometrical aperture, it seems natural to extend the notion of a solid angle and call this a "velocity dependent solid angle".

The relativistic shift for a 30 keV beam is only about 25 mÅ. For beta values one order of magnitude larger than those encountered here this shift moves the apparent source of "line center" (1215.67 Å) radiation appreciably. The region that emits this radiation travels farther upstream towards the oven as the energy increases. The apparent light source can be outside the field of view. In this case a small slit would loose too much Lyman alpha radiation. For the energies typically encountered in this experiment a geometrical angle of 5° will lose 20 per cent of the light. Figure 3-5 shows the relative transmission of the

oxygen as a function of the complement of θ, viz., δ. Figure 3-6 is the integrated intensity of the light as a function of the geometrical half-angle (δ_o) and the energy.

This velocity dependence of the solid angle will wreak havoc with calibrations. Some workers have worried about the Doppler shift.[33,77] The extent of their concern about the standard calibration procedure is not known. This method[32] consists in colliding electrons with thermal molecular hydrogen. Countable UV is created. When metastable atoms are quenched, their energy is several thousand electron volts. Consequently the solid angles may differ considerably.

For purposes of illustration suppose that the counting rates are proportional to the cross section and the solid angle. This is a low density target. One then has

$$\sigma_x = \frac{R_x}{R_c} \frac{d\Omega_c}{d\Omega_x} \sigma_c \qquad (3.12)$$

where the subscript "c" stands for calibration and "x" for the experiment. $d\Omega_x$ varies with beam energy. Above 10 keV it is relatively constant. At lower accelerating voltages a slight energy variation changes beta rapidly and with it, the solid angle. Since $d\Omega_x$ is velocity dependent, the measured cross section (σ_x) will be too small unless this effect is noted. If the rates were equal and the velocity dependent solid angle were twice the "thermal" one, σ_x would actually be twice σ_c. A naive calculation would have called them equal instead. The calibration correctly gauges the angular and radial counter sensitivities but not the geometry.

Unless special precautions are taken, Lyman alpha can scatter into the UV detector. This light reflects from metal surfaces. It will have undergone a different Doppler shift than the directly viewed radiation. The virtual emitting region can be much bigger than the real. Light that travels directly downward under the FB detector, strikes a horizontal surface, and reflects upward into the counter will add a constant background to the directly viewed radiation. This reflect light will be shifted less than the equivalent direct light. For faster metastables the frequency of the scattered light moves towards higher attenuation values. And so its signal decreases. Such an effect is noticeable in the data of Sellin and Granoff.[45] Their measurements show an abrupt jump near 10 keV that can be explained by this scatter-shift hypothesis.

There is a large caveat to be connected to the above calculations: Nature is not simple. At least four effects should be included in quantifying the response of the filter to Lyman alpha. First, the beam is a three-dimensional entity. It is more or less a cylinder. This finite extent of the source should be included in a more complete calculation. Secondly, impurities such as water vapor or ozone will wash out the absorption minimum. A third point is that the curves were derived using values of the absorption coefficient for low pressure. Preston[66] and Watanabe[75] have observed a linear pressure effect on this coefficient for line center Lyman alpha radiation. The attendant change at nearby wavelengths is unknown. Preston suggested that the minimum lies near a weak oxygen band. At atmospheric pressure the absorption curve could be even more distorted than it is for low pressure.

Finally, the calculation was performed under the assumption that the photons vanish from the beam. As a result of multiple scatterings in

the oxygen, some will actually emerge from the cell and enter the counter. This is a radiative transfer problem. The photon flux consequently is too low. The impurity effect will decrease this flux but increase the effective acceptance angle of the detector. The baric changes will probably decrease both the angle and the transmission.

Although "gold black"[78] deposits reduce the reflection of Lyman alphas from metallic surfaces, visible[79] as well as ultraviolet radiation[33,80] is emitted whenever ions strike such surfaces. The light intensity is strongly dependent on both the beam current and its angle of impact with the surface. Such countable UV has been observed in this experiment too. When protons hit the rod holding the radioactive source calibrator (Section 3.6), the counting rate was markedly increased.

4.0. PROCEDURES FOR DATA TAKING

4.1. Data Taking

4.1.1. Introduction

The basic data taken are the neutral beam fraction (F^o) and target density (n(x)). These are measured as a function of probe energy. The triad of fraction, density and energy are adjusted in four simple ways. The simplest is to fix the beam energy and vary the alkali density over a narrow range. This is the low density (LD) method. The neutral fraction is approximately a linear function of target density (see Equation (2.13)). A related method is to look at two or three different energies and slightly vary the density. This is basically performing several LD runs at once. Of course the number of measurements that can be taken for each energy is lessened. This cross section normalization method is useful in normalizing sets of results. It is used mainly as an overview of charge exchange reactions, especially for the H_2^+ beam interacting with the alkalis.

The third main run type is the complete curve (CC) run. Again the beam energy is fixed. This time the oven temperature is increased to such a high value that the high density asymptote (C^o) is reached. There the neutrals obey (2.14). The fourth type is done very infrequently. The oven stays very hot. This creates a thick target. This run type verifies the asymptotes already found by CC runs or measures them for a variety of energies.

4.1.2. Density Determinations

The density is determined by monitoring the oven thermocouples described in Section 3.4. It is known that the vapor pressure of a metal obeys

$$P(T) = P_o e^{-k/T} \quad . \tag{4.1}$$

This is converted to density at NTP by invoking the Ideal Gas Law. Thus the density of an alkali is given by

$$\rho(T) = \frac{A\, e^{-B/T}}{T} \quad . \tag{4.2}$$

The constants are determined by fitting the data given in Reference 12. They are tabulated in Table 4.1.

A molecular flow model is used to find the target density in the oven. Let A_1 be the area of the well opening and A_2 the exit area of each flange. If the well density is n_1, the density of particles re-entering the well is n_o, and the particle density leaving through each one of the two flanges is n_2, then the following relation holds:

$$n_1 v_1(T_1) A_1 = n_o v(T_o) A_1 + 2 n_2 v_2(T_2) A_2 \quad . \tag{4.3}$$

There are two limiting cases: the atoms bounce back into the well with its thermal velocity (T_1) or with the arm temperature (T_2). These two extremes are presented in Equations (4.4) and (4.5).

$$\frac{n_2}{n_1} = \left[1 + \frac{2A_2}{A_1} \sqrt{\frac{T_2}{T_1}} \right]^{-1} \tag{4.4}$$

$$\frac{n_2}{n_1} = \left[1 + \frac{2A_2}{A_1} \right]^{-1} \sqrt{\frac{T_1}{T_2}} \quad . \qquad (4.5)$$

Typical operating temperatures are $T_1 \sim 500°K$ and $T_2 \sim 450°K$. Equation (4.4) can be approximated as

$$\frac{n_2}{n_1} \left[1 + \frac{2A_2}{A_1} \right]^{-1} \sqrt{\frac{T_1}{T_2}} \left\{ 1 - \tfrac{1}{2} \frac{\frac{T_1 - T_2}{T_2}}{1 + 2A_2/A_1} \right\} . \qquad (4.6)$$

For the above temperatures the discrepancy in densities is less than 3 per cent.

4.1.3. Neutral Fraction Determination

For one data point the total beam falls upon the foil thermocouple (D_{tot}). The bridge circuit is used to null the generated E.M.F. The reading of the fine adjustment pot is recorded as D_{tot}. The coarse control is always adjusted so that the null position is at least half way (500) on the fine pot. Since experimenters normally have five fingers on each hand, there is a bias towards recording readings in multiples of five. This "half way" precaution keeps this bias error small.

High voltage is applied to the capacitor plates at the entrance to the detector chamber. The ions are swept from their original beam track. The lessened heating effect is noted (D_n). Small contact potentials are determined by turning off the beam and recording the galvanometer deflection (D_{zero}). Then the sought-for neutral fraction is just

$$F^{o} = \frac{D_{n} - D_{zero}}{D_{tot} - D_{zero}} \quad . \qquad (4.7)$$

T_1 is the well temperature (t_w). T_2 is the average tube temperature as determined by the two arm thermocouples (t_m, t_a). The flange thermocouple (t_f) is merely a check upon the effectiveness of the arm heaters. Since it is nearest the cold shield and it makes poor contact with the arms (the metal O-ring), it normally reads lower than the others. These galvanometer readings are converted into temperatures using the calibration curves of Section 3.7. The particular curve to be used depends on the room temperature.

4.2. Typical Data Runs

4.2.1. Charge Exchange Cross Sections

A typical LD run consists of monitoring three foil galvanometer deflections, four thermocouple readings and the proton current. This last datum is a check. The galvanometer readings are so much more sensitive that they are used for serious measurements. A difference of two per cent is noticeable on the galvanometer irrespective of the total signal; occasionally a change of ten per cent on the ring current is not noticeable.

Figure 4-1 shows a sample data set. Oven thermocouples [tw, tm, ta] determine the vapor density. Equation (4.7) determines $F^{o}(\pi)$. The next data point is taken. For LD and CC runs the oven temperature is increased. For the others the energy is changed and later a new density is set.

4.2.2. Lyman Alpha Data

Whenever Lyman alpha radiation is to be monitored, the above procedures change. Normally an LD run is made. At the same time the photon counter is activated. While the total beam - both protons and neutrals - enters the detector chamber, this counting rate is recorded (NF). Then the dipole field is applied. The metastables are quenched. This rate is recorded (F). Whenever the foil galvanometer zero is being determined, the background signal (BG) is noted. The number of metastables is then proportional to F-NF. The cascade signal is NF - BG. The proportionality constant (Ξ) is the same for both. It was to have been determined by the electron gun calibration. This tale appears later. Typical counter data are presented in Figure 4-2. The above naive picture must be modified somewhat. Just as the quench field mixes the levels of the first excited state, it also mixes the other levels. Further it will be seen in Appendix C that some of the "resonant" levels live longer.

4.3. UV Detector Calibration

The counting rate of the scaler depends upon the number of photons that can be transmitted by the optical train. The proportionality constant (xi) between the photons emitted and the counting rate is given by

$$\Xi = d\Omega \frac{dS}{R^2} T^2 T_o E_c E_e \qquad (4.8)$$

where $d\Omega$ is the solid angle subtended by the beam

dS is the area of the detector

R is the distance from the beam to the detector

T is the transmission of the LiF crystal

T_o is the transmission of the oxygen

E_c is the counter efficiency

E_e is the efficiency of the electronics.

The quantity $d\Omega dS/R^2$ is called the throughput of the optics. It is readily measurable. The transmission of the crystals is approximately one half.[69] For oxygen at NTP the extinction length is extrapolated to 1/0.65 cm. Thus the transmission (T_o) is 0.278. However the counter response is strongly temperature dependent. The photoionization efficiency[61] (reaction (3.1)) is approximately 0.42 but the iodine density follows Equation (4.2).

In addition to this counter response, the iodine reactions limit the number of photons that can trigger the detector. This dead time effect has been calculated.[69] The notation used there is slightly different from that used here. The observed counting rate (R_o) must be corrected for the counts that are lost while the Geiger tube is recovering from the previous pulse. Let the maximum rate as determined by the dead time be designated as R_x. The actual rate (R_a) becomes

$$R_a = R_o \left(1 + 2 \frac{R_o}{R_x} \right) \quad . \qquad (4.9)$$

Typical pulses after 40 dB amplification are 1 volt high. The peak occurs 40 μsec after onset. The recovery time is about 250 μsec. The next

triggering pulse occurs approximately 350 μsec after the onset. This differs somewhat from other counters.[69]

AC fields are present in this interaction region. They come primarily from the ripple on DC power supplies. In order to lessen their effect on the scalar discriminator, a 120 Hz trap was installed between the amplifier and the scaler. It is estimated that the electronics pass one half of the signal pulses. To simplify calculations the calibration runs should ideally produce the same rates as data runs.

In light of the filter discussion in Section 3.10 and the published angular response of the UV counter,[63] Ξ is actually dependent on temperature and emitter position.

5.0. RESULTS

5.1. Charge Exchange Cross Sections

5.1.1. Measurements of σ_{10} and σ_{01}

The electron capture (σ_{10}) and loss (σ_{01}) cross sections have been determined for a pair of beam ions and a pair of alkali targets. Equation (2.11) has been used to find σ_{10} as a function of beam energy for proton-sodium, proton-potassium, molecular hydrogen ion-sodium and molecular hydrogen-ion-potassium interactions. These are shown in Figures 5-1 - 5-3. They are also listed in Tables 5.1 - 5.3.

The high density asymptotes (2.14) were found for all the above combinations. The values shown in Figures 5-4 - 5-6 are probably lower limits. It is not known if the true asymptotes have been reached. The error bars merely indicate a significant spread in data. Equation (2.14) is used to derive the values for σ_{01} as shown in Figures 5-7 - 5-8. The error bars shown for these cross sections are those which arise from an assumed ten per cent error in the asymptote.

The σ_{10} shapes agree quite well with Gryzinski theory and Equation (2.30). Normalized theoretical curves are shown in Figures 5-1 and 5-2. $_{01}Q_{10}$ has been calculated for a few simple excited alkali states and the hydrogen 2S level.

Preliminary results have been reported for protons interacting with potassium.[40,81] These have been slightly modified. The background neutral fraction (δ) correction as shown in Equation (2.13) causes a miniscule increase in σ_{10}. A more important change is caused by the application of standard statistical methods and the removal of bad data.

5.1.2. H^- Contributions and $\sigma_{\bar{1}0}$ and $\sigma_{0\bar{1}}$

An upper limit on the amount of H^- ion produced is about three per cent below 10 keV. This comes from deducing the negative ion current that would diminish the ring current enough to affect the inferred positive flux. The difference between total beam and neutral beam heating can be ascribed almost entirely to the positive current monitored. Above 10 keV no H^- seems to be formed. A reasonable limit is one per cent.

If there were appreciable negative ions in the beam, the complete curve data (CC) of 4.1.1 would deviate from the simple exponential expression of (2.11). The H^- concentration should be small. Its most probable source is charge transfer with H^o. Proton interactions with cesium create no more than 3 per cent H^- above 4 keV.[42] The simple form of Equation (A46) should be usable here. The difference between the data and the simple exponential was examined for $\sigma_{\bar{1}0}$ and $\sigma_{0\bar{1}}$ as set forth in Appendix A.

A series of test cases was run. The high density asymptote was found very accurately. The determinations of α and β depended upon the relative sizes of A and B. This is proper. Actual data were then put through this procedure. The results were quite definite. Two exponentials always fit the data worse than just one as given by (2.11). Since some of the parameters of the extended fit interact, their number was reduced from 5 down to 3 eventually. Successive iterations were also used. At the very best the errors associated with this extended fit nearly equalled those of the simple exponential. By this time, however, the parameters had changed drastically from the initial guesses. α and β showed an infuriating tendency to approach one another.

There are three disturbing possible explanations for this failure. The obvious one is that there is too much scatter in the data from random errors to allow the finding of these two additional cross sections. Then, the double electron charge exchange cross sections that were dropped so hurriedly in Appendix A might turn out to be comparable to the ones found. This is unlikely. The two cases mentioned in the appendix are indeed small. There is even the strong possibility that σ_{01} is not really constant. [(see Equation (2.7)].

5.1.3. Inner Shell Electron Contributions

Il'in[21] invokes inner shell interactions to explain the high energy portion of his measured cross sections. A calculation by Vinogradov, Presnyakov and Shevel'ko[82] for the metastable cross sections also involves exchange with the inner electrons of the alkali target. The values of Bearden and Burr[83] and the formalism of Section 2.4 produce interesting differences in both the total charge transfer cross section (TX) and the metastable creation one (MX).

A partial listing of the binding energies for the alkalis is given in Table 5.4. The valence electron is bound by 4 or 5 electron volts. The shell just below it has binding energies on the order of tens of volts. For the next lower shell these values rise to hundreds of volts. Thus the main contributions to the cross sections come from the valence electron and from the electrons in the first shell beneath it. Valence values predominate at low energies but significant changes appear at high energy when the inner shell electrons are included. The contribution of the inner shell is taken to be the cross section

corresponding to that ionization potential multiplied by the number of electrons with that energy.

For this inner shell exchange direct formation of ground state hydrogen predominates. This is contrary to the result of valence electron transfer. Both cesium and rubidium energies are especially close to the hydrogen 1S binding energy. However, the excited hydrogen cross sections are also affected. The effectiveness of these inner electrons increases with increasing atomic weight. TX and MX for lithium change imperceptibly whereas the total cross section for rubidium doubles at one keV and flares about 20. The calculation for the total cross section diverges for the cesium 5p subshell. A better approximation along the lines suggested by Gerjuoy[84] or detailed balancing[40] should be applied to this or any other example of a tangent-like discontinuity.

The tendency of the cross sections to bundle is loosened. The total cross sections would still cluster except that lithium gains too little from its two 1s electrons. The metastable values are completely untied. They run parallel now instead of asymptotically converging. These results are depicted in Figures 5-11 - 5-14.

It is true that the theoretical cross sections increase when inner electrons are included. These computed values do not exhibit the bulge seen by Il'in.[21] None of the other[41,42] measured cross sections bulge either. There is enough scatter in the metastable cross sections reported by Sellin and Granoff[45] to satisfy either the pure valence or the included inner shell calculations. The data do seem to fit the valence values better.

5.1.4. Detailed Balancing Results

Whenever the cross sections are discontinuous, they can still be determined by using prescription (2.35). For valence electron exchange into the hydrogen ground state the weights are equal.

The maximum contribution is less than 4 (-17) cm^2. The gap between the lithium-sodium bundle and the K-Rb-Cs bundle again appears. The ordering of the cross sections is the reverse of the TX values mentioned previously. The lithium cross section is now the largest, cesium smallest.

For inner shell transfer only the cesium value diverges. The electrons that form the $(5p)^6$ shell are further divided energetically into the O_{II} (2 electrons at 13.1 eV) and O_{III} (4 electrons at 11.4 eV) subshells. The ratios of the weights are 4/2 and 8/2, respectively. σ_{10} so calculated is shown in Figure 5.11.

$_{01}Q_{10}(1,1)$ also misbehaves. It is calculated from a modified version of Equation (2.26) where the binding energy is appropriately changed. The weights are again equal. This value is used in computing the curves of Figures 5-9 - 5-10 where it is an upper bound to the experimental values.

5.2. Determination of the Neutral Fraction Background

The major background gas is molecular hydrogen. It flows from the source in the beam path at least until the middle of the magnet chamber. There about one-half of the gas is removed by the 2" diffusion pump. The most likely candidates for causing the zero target density signal (δ) for proton and molecular ion beams are

$$p + H_2 \rightarrow H + H_2^+$$
$$H_2^+ + H_2 \rightarrow H_2 + H_2^+ \quad . \qquad (5.7)$$

Allison[85] among others has investigated the first reaction. McClure[86] has measured the molecular hydrogen cross sections. The second reaction above is much more likely in this energy range than a dissociative collision into H or H^+.

The background signals are fitted to the curves of Allison (proton probe) and McClure (molecular hydrogen). They are plotted in Figures 5-15 - 5-16. δ is typically 0.04. It should be noted that the potassium vapor data was taken earlier than the sodium. There seems to be a larger background gas π value for the sodium target. Ion gauge readings in the exchange chamber bear out this higher gas pressure for the later runs.

Because of poor statistics all molecular hydrogen ion data were averaged together. These data scatter much more than the comparable proton values. Nevertheless all path length-density (π) measurements are consistent. Whenever the background fraction (δ) is fitted to the above mentioned cross sections with the methods of Appendix E, the normalization constant is π itself. For the 28 cm path length between the magnet chamber and the oven, this value and Equation (2.12) yield an average pressure of about 1(-4) Torr. Uncorrected exchange chamber ion gauge readings were about half of this value. The elbow (the magnet chamber) gas pressure was about 0.1 Torr for 500 microns source pressure. Since the molecular hydrogen density is higher towards the source, there is good agreement between this derived value and observations.

Table 5.5 lists the results of the above calculation. Potassium served as the target earlier than sodium. Observed ion gauge determinations are lower for the former as are the derived π values. By using this data and the known cross sections, one can compute the number of metastable atoms formed by collisions with the background hydrogen gas.

5.3. The Metastable Hydrogen 2S State

5.3.1. Sources of Metastable Atoms

The metastable cross section for electron caputre (MX) has been calculated from Equation (2.26). It is assumed that it is one quarter of the value for capture into the first excited state. MX is displayed for various targets in Figure 2.5. Cascade effects are important for the total 2S population. The $\mathcal{C}$ channel contributes about 13 per cent to the number formed (see Figure 2-8).

Collisions with hydrogen gas also contribute. The background gas π values found in the preceding segment can be used to calculate the initial metastable concentration. Van Zyl, Jaecks, Pretzer and Geballe[87] report this cross section to be 6 (-17) cm^2. The background metastable fraction is then 7 (-3). Bayfield[27] claims it is 1 (-17). This reduces the fraction to 1 (-3).

The attempted UV detector calibration of Section 4 ranks in history with that famous success, Apollo XIII. As the hydrogen pressure increased, the counting rate decreased!

Although the in situ calibration was a smashing failure, xi - Equation (4.8) - can be estimated. Instead of the expected ratio of

20 per cent for MX to TX, a value less than 2% was found. To try to account for this, one should begin by reciting the litany of known loss mechanisms.

5.3.2. Loss Mechanisms

Metastable atoms are formed during charge exchange with alkali atoms. The 2S state is fragile. Its population can be depleted not only by a second charge transfer reaction but also through the Stark effect mixing described in Appendix C. Stray electric fields can cause this mingling of the 2S and 2P levels. Two other sources of such a field are motion in a magnetic field and collisions with a target without charge transfer. This first mechanism is related to the Lorentz ionization mentioned in the introduction.

The general Lorentz transformation for fields in a fixed frame (unprimed coordinates) to some moving frame is given by[88]

$$\vec{E}'_{\parallel} = \vec{E}_{\parallel} \qquad \vec{E}'_{\perp} = \gamma\left(\vec{E}_{\perp} + \vec{\beta} \times \vec{B}\right)$$

$$\vec{B}'_{\parallel} = \vec{B}_{\parallel} \qquad \vec{B}'_{\perp} = \gamma\left(\vec{E}_{\perp} - \vec{\beta} \times \vec{B}\right) \qquad (5.8)$$

where $\vec{v}$ is the relative velocity of the moving system with respect to the stationary one. The parallel ($\parallel$) and perpendicular ($\perp$) directions are determined by the velocity vector. β and γ have the standard relativistic definitions. Motion in the earth's magnetic field creates an electric field of about 1 volt cm^{-1} for the speeds encountered in this

work. Fringe fields from the magnet are approximately 2 Gauss. The most intense field near the einsel lens reaches 10 G. For these values the fields are 4 and 20 V cm^{-1} respectively. The metastable lifetimes are correspondingly 354, 22 and .9 μsec. For the maximum field the fraction remaining drops to 2/3 of the original. For the more reasonable and more pervasive fringe value the fraction removed shrinks to 1/60. This $\vec{v} \times \vec{B}$ mixing should have little effect on the metastable population.

The fields from comoving protons will be considered next. For the nominal energy of 30 keV ($v/c \approx 1/150$) and 1 cm defining apertures a 2 μA beam possesses a flux of 1.25 (13) sec^{-1} cm^{-2}. Under these conditions the beam density is 6(4) cm^{-3} and the average proton spacing is about 2.5 (-2) cm. The static field thus produced is only 2.3 (-4) V cm^{-1} which is negligible even when compared with the earth induced field.

Actually these protons are not comoving. A velocity distribution is superimposed upon the much greater beam speed. Purcell[89] has performed a semi-classical calculation which relates the transition probability between the metastable 2S and resonant 2P levels to the Maxwellian temperature. Several of his numerous misprints are corrected and are shown below. This transition rate (W) is simply related to the cross section through

$$W = N \sigma \bar{v} \tag{5.9}$$

where N is the ion (or electron) density and

$\bar{v}$ is the average Maxwellian speed.

These rates are

$$W_i'(2S_{1/2} \rightarrow 2P_{1/2}) = N_i \frac{96 e^4 a_0^2}{\hbar^2} \left(\frac{\pi m_i}{8kT}\right)^{1/2} \ln\left\{\frac{0.458\, kT\hbar}{e^2 a_0 m_i \omega'}\right\}$$

$$W_i''(2S_{1/2} \rightarrow 2P_{3/2}) = N_i \frac{192 e^4 a_0^2}{\hbar^2} \left(\frac{\pi m_i}{8kT}\right)^{1/2} \ln\left\{\frac{0.458 kT\hbar}{e^2 a_0 m_i \omega''}\right\} \quad (5.10)$$

where ω' is 2π x 1058 MHz

ω'' is 2π x 9940 MHz

T is the absolute temperature

m_i is the reduced mass of the ion as suggested by Seaton[90] and the other atomic constants have their normal (cgs-esu) values. The extra factor of 2 in the second equation comes from the enhanced strength of the $2S_{1/2}$ - $2P_{3/2}$ transition. The filament temperature is about 1500°K. If the protons have this temperature, each cross section from (5.10) is about 2.5 (-12) cm^2. These are listed in Table 5.6. Electrons are about one tenth as effective as protons in this quench mechanism.

The formulae of Purcell can also be applied to the quenching by alkali ions which were formed previously by charge transfer with the proton beam. The velocity distribution is now a delta function of the beam speed.

$$W_i' = 2\pi N_i \int_0^\infty dv\, f(v)\, b^2 \left[\frac{3}{2} - 2C + \ln\left\{\frac{v}{\omega' b}\right\}\right] \quad (5.11)$$

where $b^2 = \frac{12\, e^4 a_0^2}{h^2 v^2}$

$f(v) = \delta(v - v_0)$

$C = 0.5771$ (Euler's constant).

The cross sections so derived are shown in Table 5.7. Their sum is roughly 1 (-13) cm^2. Wilcox and Lamb[91] have extended the Purcell relations to 3S - 3P transitions. Since this S state decays by dipole radiation, its lifetime is not noticeably affected.

In addition to being quenched by ionic impacts, the metastables are also disturbed by molecular collisions. The dipole-multipole interaction changes the internal state of the molecule as well. Gersten[92] has calculated these cross sections and has compared them with the experimental results of Fite and coworkers.[10] For their thermal beams there is very good agreement between theory and observation. The cross sections may be approximately written as

$$\sigma_\ell = \pi \frac{\ell+1}{\ell} \left\langle 4 g_\ell \frac{\ell+1}{2\ell+3} \left(\frac{3 e a_0}{\hbar v} M_\ell \right)^2 \right\rangle^{1/(\ell+1)} \qquad (5.12)$$

where $g_\ell = 5/3$ for $\ell = 1$ (dipole interaction), $g_\ell = 56/45$ for $\ell = 2$ (quadrupole) and the average is performed over the projectile speed. With the measured quadrupole moments of Bloom et al.[93] and an average speed of 8 (5) cm sec^{-1} (1/3 eV) all values agree to within about 25 per cent. Incidently, the cross section for CO_2, which has not been measured, is calculated to be 3.5 (-14). This is somewhat larger than the observed values for N_2, O_2 and H_2 but is one sixth the water vapor

result. When this calculation is extended to kilovolt energies, the cross sections are still considerable - about 5 square angstroms.

The background gases that could quench the 2S atoms in this manner are primarily molecular hydrogen, air, water vapor and hydrocarbons from the pump. Water is the most efficient of the metastable destroyers that have been measured but it should be a minor constituent due to trapping by the cold bucket around the oven. Hydrocarbons typically exhibit a dipole moment of 2 (-18) esu.[94] Since this is nearly the value for H_2O, hydrocarbons should behave like water vapor. Molecular hydrogen should be the primary target. It is the most abundant background gas. The following cross sections are taken from Table 5.8 for a 10 keV proton beam: $\sigma(N_2)$ = 6 (-16), $\sigma(O_2)$ = 4 (-16), $\sigma(H_2)$ = (-16), $\sigma(H_2O)$ = 3 (-15). For measured hydrogen densities the population change will be a few per cent.

Sellin's 3 component fit has yielded a total depletion cross section of 2 (-15) cm^2 at 15 keV.[44] Equation (5.13) for H_2 quenching gives 2.4 (-16). This suggests that removal of the metastables by ionization may be very important.

Other investigations in this energy range have been conducted recently.[95-97] Three loss mechanisms have been considered. Electron loss by stripping rather than by charge transfer has been studied. The two other destruction mechanisms are de-excitation and formation of H^- by electron capture. Bates and Walker[98] have calculated the cross section for ionization. The results of Dose, Meyer and Salzmann[95] for nitrogen and water vapor quenchers may indicate H^- formation is important below 5 keV. The combination of Gersten and Bates and Walker calculations adequately describes the high energy region, however.

The total quenching cross sections for hydrogen,[96] nitrogen, and water vapor[95] are about 1 (-15) cm^2. The ionization cross sections for H_2 and the noble gases[96] seem to be approximately 3 (-16). Cesium[97] at 2.5 keV has this same general value.

5.3.3. Tentative Solution to the Case of the Missing Metastables

As the calculations of Section 5.3.2 show, large quenching cross sections do exist. The problem is how to couple a large cross section with an abundant metastable destroyer. There are not enough protons for the Purcell values to be effective. The number of alkali ions present is also too low. For total conversion of protons into neutrals and complete retention of the resulting ionized alkalis there will be only 2.5 (9) ions per cubic centimeter at day's end. Hydrogen is present in larger quantities but its cross section is some 4 orders of magnitude smaller. Clearly something more is needed.

If the charge transfer process is viewed as resulting from the presence of an external electric field, then a possible solution appears. Assume that this field is so intense that the 2S and 2P states are thoroughly mixed. After a few nanoseconds the metastable state will be depleted. In the time it takes to reach the UV detector the more highly excited states can decay into the 2S state. The metastable ratio will then be about 1% which is the observed value.

Donnally[24] says 0.3 per cent of his protons were converted into metastables. For his published value of 4 (-15) cm^2 which may be somewhat low[41] one deduces π to be less than 1 (12) cm^{-2}. Sellin in his H_2 studies operated near 1.5 (15) cm^{-2} with his 10.16 cm oven. The metastable formation cross section there was a few times 10^{-18} cm^2 which is

much less than the expected alkali values. The oven used in the present experiment was 16 cm long. As the metastable data of Figures 5-17 and 5-18 show, the present π values are larger than those of Donnally but smaller than those of Sellin.

Sellin built a model consisting of three beam components: protons, ground state hydrogen atoms, and metastable atoms. Using equations similar to those in Appendix A for three charge states, he was able to fit the metastable signal as a function of H_2 density. The resulting curve looks like a question mark lying on its side. There is an initial linear region. This is followed by a peak and then the signal decreases toward a lower asymptote. This is totally consistent with the observed sodium data. Curvature is evident in Figure 5-18. Other data show the peaking and the subsequent decline.

There seem to be two different effects operating here. The metastables are being quenched by the alkali target. The counting rate is linear below a sodium density of about 5 (12) cm^{-3}. Then the rate becomes at least a quadratic function of density. The background signal is linear throughout. This Lyman alpha probably comes from decay of the 2P states. The resonant levels are filled from higher ones. The cross sections for populating these states are much smaller than MX. The initial populations will be linearly dependent on the target density. Hence this background signal will be, too.

The 20 keV data can be interpreted as a two state picture, for example. The metastable creation cross section is 5 times the background value. It should be more like 100 times as great. The sum of MX and the loss value is about 27 (-16) cm^2. Similar values can be deduced from the

16 keV data of Figure 5-17. As Sellin has shown, the 3 component model is needed to explain the variation of metastable fraction with density. It is difficult to estimate the depletion cross sections for this reason.

A second effect is the reduction of counting rates. If the counter efficiency is known fairly well, another quenching mechanism is probably needed. A guess at the size of this cross section is about $1/3\pi$ or 2 (-14) cm^2, which is rather large. Sellin does need a quench cross section of about 2 (-15) for a much larger path length-density product and lower formation rate, however.

If the formation field is so strong as to ravish the 2S state so completely, it may not affect any other state. All other excited levels can decay through dipole transitions. Such a field will mix them too but not change their populations so drastically. The idea of the populations being related to the statistical weights would still be valid for all but the metastable state.

5.4. Excited Alkali Atoms

The viewing port in the exchange chamber overlooks the front of the oven. Through the plexiglass brightly shines akaline light. With sodium in the oven, an intense yellow light is seen. Protons colliding with potassium atoms produce a washy blue color. The sodium radiation comes from the famous D lines ($\lambda\lambda$5895.93, 5889.96). These arise from the transitions $3^2P - 3^2S$. The corresponding lines in potassium ($4^2P - 4^2S$) lie in the infrared at $\lambda\lambda$7644.94, 7699.01Å. The $5^2P - 4^2S$ transitions are visible and are blue ($\lambda\lambda$4044.14, 4047.20).[98] These states should not be as heavily populated as the lower lying P states. Consequently

this blue radiation should not be as intense as the infrared potassium light or, by extension, the sodium D lines. In fact, the blue light is much weaker than the yellow. Since two different energy levels are populated, one infers that most (if not all) alkali states are populated by the proton interaction. This result also appears in the calculation of $_{01}Q_{10}$ in Section 2.4.2. Hence, charge exchange reactions between protons and alkali atoms create excited alkali atoms as well as excited hydrogen atoms.

$_{10}Q_{01}$ has been calculated for charge transfer with excited alkalis. Figure 5.19 shows the cross section for electron capture from the first excited state for both sodium and potassium. This cross section is twice that with ground state targets. Metastable formation is much less. The density of such excited targets is very small however. It can be calculated by equating the number of atoms that decay per unit time and unit volume to the number formed from the proton beam per second per unit beam per unit area. It follows that

$$\frac{n^*}{n} = \frac{I}{qA}\,\sigma\,\tau \qquad (5.14)$$

where n^* is the number density of excited atoms,

n is the alkali density,

I is the beam current,

q is the proton charge,

A is the area of the beam,

σ is the cross section for making the excited atoms,

τ is the lifetime of the state.

For reasonable values for these quantities, the ratio is only 1 (-8). The D lines were also seen for H_2^+. Even if the excitation (without electron transfer) cross section is much larger than 1 (-14), the ratio will still be small for believable values.

6.0. CONCLUSIONS

6.1. Overview

In this work the interactions between hydrogen ions and alkali atoms are studied. The proton study may be divided conveniently into three main parts. The first is the experimental determination of the total electron capture and loss cross sections (σ_{10} and σ_{01}) for potassium and sodium. The proton energy ranges between 4 and 30 keV. The second major point is the modification of Gryzinski theory for charge exchange between protons and alkalis. Predictions are made for both the total charge exchange cross section ($_{10}Q_{01}$) and the cross section for exchange into just the metastable hydrogen $2S_{\frac{1}{2}}$ state. Comparisons are made between these values and measured ones. In this way the observations of several groups (including this one) can be systematized. The investigation of Lyman alpha radiation from metastable hydrogen atoms is the third theme.

Several minor points are also covered in the present work. A fast survey of cross sections has been run using molecular hydrogen ions in place of protons. These seem to be the only measurements in the 10 - 30 keV range. Collisions between both ions and hydrogen gas create a background atomic hydrogen beam. The fraction so produced is directly proportional to known cross sections. Proton collisions with alkali atoms excite the target atoms. As they decay, they emit copiously. During the study of the hydrogen 2S state, the sharp angular sensitivity of the molecular oxygen filter has been calculated. These various matters will now be examined in more detail.

6.2. Proton Beam

The measured proton data are consistent with both the sparse experimental points of Il'in, Oparin, Solov'ev and Federenko[21] and the modified Gryzinski calculations of Section 2. The total electron capture cross sections (σ_{10}) agrees with the theoretical charge exchange cross section ($_{10}Q_{01}$) to within a scale factor. σ_{10} for potassium is 1.65 times the computed value for charge exchange into all excited hydrogen states. The best value for the sodium multiplicative factor is 1.38. Elsewhere, Schlachter et al.[42] report σ_{10} for cesium which is 1.31 times larger than the theoretical result here. The measured values for σ_{10} are thus within a factor of two of the exchange cross section ($_{10}Q_{01}$). It appears that the major component of σ_{10} is $_{10}\sigma_{01}$ as has been assumed in Section 2.

The measured cross sections (σ_{10}) for both sodium and potassium agree generally with those of Il'in. For potassium the values found here agree very well at low energy but are much lower near 30 keV. The quoted results of Schmelzbach[41] are much lower than either the present data or the Russian values. The discrepancy is roughly a factor of four. This is probably due to difficulty in determining the oven density. However, all three results exhibit the same shape above 5 keV.

The sodium target data agrees well with Il'in. The flaring that appears in his potassium cross sections does not occur here for sodium. The general shape of the curves agrees with the Gryzinski form given by (2.30). The systematic difference between the two curves (the "gap") is distinct in the present work but is much less noticeable in Il'in's

results. Even there, however, potassium cross sections are always larger than sodium values. Here, if anything, the gap is too large.

The asymptotic values also agree well. The single point of Il'in almost coincides with the present measurement for K. The values of Schmelzbach are consistently lower. For sodium the present data lie below that of Il'in. When these results are combined with those of Schlachter, one sees that F^{0}_{∞} for alkalis is quite consistent. Below ten kilovolts the maximum neutral fraction is nearly unity. Then it declines monotonically. Near 20 keV the ratio becomes one half. F^{0}_{∞} falls to 0.25 near 30 keV.

6.3. H_2^+ Beam

The cross sections for the molecular hydrogen ion are uniformly larger than those of the proton probe. σ_{10} for potassium seems to be much larger than σ_{10} for sodium. The reason for the apparent factor of 4 difference is unknown. The neutral fraction is also larger for H_2^+ than for H^+ at the same energy.

6.4. H(2S)

Since the in situ calibration of the Lyman alpha detector was a failure, it is necessary to estimate the counter efficiency. Assuming this is known to about a factor of 2, one needs to invoke a powerful quenching device to destroy the metastables formed by direct exchange. The cross section for this annihilation is approximately $2\ (-14)\ cm^2$. This value is compatible with known depletion values. A new mechanism seems to be required; the standard ones are not powerful enough. Sodium

quenching of the 2S atoms is evident. This cross section seems to be about 2 (-15) cm^2. The predicted creation value is only a few times 10^{-16}.

The modified Gryzinski calculation indicates that all metastable cross sections will be nearly equal above 10 keV. This has been observed.[45] Also the ratio of the metastable to the total cross section should be approximately constant at ten per cent. No data are available on this.

Metastable atoms are formed by charge exchange directly into the state. Cascading from higher levels will also populate the 2S state. If all m_J substates are filled, this increases the population by about 13 per cent. Half of these decays occur within 10 nsec of their birth. If only S state atoms are created, the cascade effect is much smaller and much slower. The population enhancement is 2½% after ½ msec. Half of these decays occur within 200 nsec after they have been formed. Such indirectly formed metastable atoms seem to be the only metastables observed in this experiment.

6.5. General Remarks

Equation (2.30) describes quite well the cross sections for protons interacting with the alkalis. If inner shell electrons are included in the calculations, the predictions are not as accurate. Both σ_{10} and $\sigma_{10}(2S)$ are noticeably affected. The data does not support this inclusion. In medical argot, it is "contraindicated".

The Born approximation as calculated by Bates and Dalgarno[9] also predicts large cross sections. Unlike the classical calculation, the

Born predicts that ground state formation overwhelms metastable creation above 25 keV. The Gryzinski calculation, when modified by detailed balancing, relegates the ground state to a continuing role as a minor constituent.

There are experimental anamolies as well. For example, the metastable cross section found by Sellin[45] exceeds the total valve found by Schlachter. Sellin does normalize his results to the cesium cross sections measured by Il'in. Schlachter's results seem higher than the Russian values. Spiess[46] has verified these higher values near one kilovolt. It seems that Il'in's experimental shapes may not be quite right. His results do show the proper ordering, however. The largest cross section does belong to cesium and the smallest to lithium. This result is predicted by the calculations of Section 2.

The question of relative population of the sublevels is still unanswered. The metastable cross sections reported so far are too large. Even if the s electron of a ground state alkali is transferred to a hydrogen s state during the charge exchange collision, the measurements remain high. Because of decay from higher levels into the metastable $2S_{\frac{1}{2}}$ state of hydrogen, the effective cross section for producing these metastables will be larger than the direct exchange value (the $\mathcal{L}$ channel). This augmentation will be time dependent. Its exact magnitude and time variation depends strongly on the model of relative hydrogenic populations used. For the "all state" model the cross section will be increased 13% in about 20 nsec. On the other hand, the s state model reduces this enhancement to about 2 per cent. This requires nearly one half of one microsecond. Probably experimental transit times between the metastable source and its detector are tens of nanoseconds.

Counterbalancing this enhancement of measured cross sections by decay is the severe angular selectivity of the commonly used iodine UV detector and its oxygen filter. The filter properties are strongly energy dependent. For the tens of kilovolt energy in this experiment and the small ($\sim$ 5%) geometrical apertures, the Lyman alpha cross section has been reduced by about 20 per cent. Scattered light will be rejected by the filter as the beam energy is increased. Apparently such reflected light artificially increases many measurements of the metastable cross section.

σ_{10} for protons on alkalis agrees fairly well between the various experimental groups and modified Gryzinski theory, but the metastable cross sections disagree with both this theory and the various groups. Below 30 keV σ_{10} is probably known to within a factor of two for all alkali vapor targets. The metastable cross section even for cesium is still uncertain to an order of magnitude.

APPENDIX A

THREE COMPONENT BEAM CALCULATION

A.1. Solutions of the Differential Equations

Whenever the proton beam traverses the target region, charge transfer reactions can leave a beam particle in one of three charge states. The fast particle can still be a proton. It could have captured one electron to become a fast hydrogen atom. Possibly it could have acquired two electrons and become an H^- ion. These processes with their relevant cross sections are shown schematically in Figure A-1. Traditionally the subscripts on the sigma refer to the initial and final charge states of the fast particle. For example, σ_{10} means electron capture by the proton.

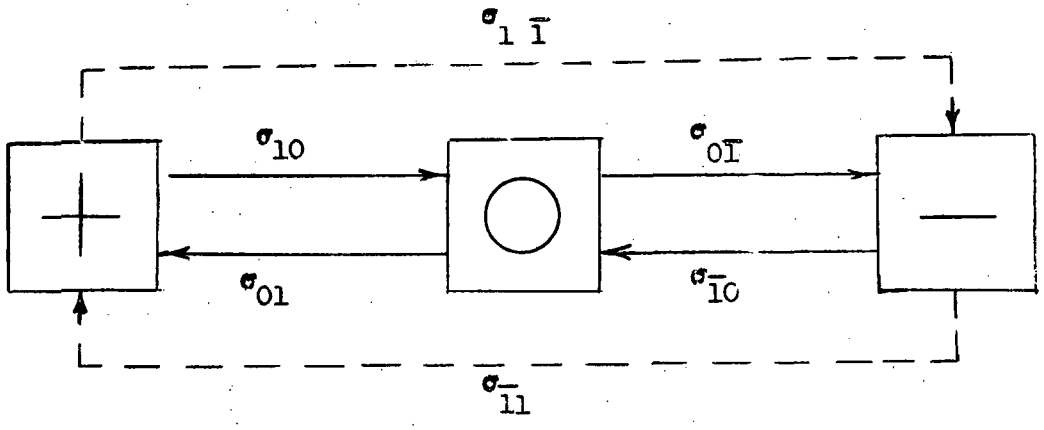

Figure A-1.

The double electron exchange processes ($\sigma_{1\bar{1}}, \sigma_{\bar{1}1}$) are assumed negligibly small compared with the others shown. This implies any H^- ions present must come from a two step process via σ_{10} and $\sigma_{0\bar{1}}$. For

example, Schlacter et al.[42] measured σ_{1I} for cesium for 2 - 15 keV. He found it varied from 3.7 (-17) to 5.2 (-18) cm^2. Schmelzbach and co-workers [41] also investigated this cross section for protons on potassium. In the energy range of 2.5 to 22 keV it declined monotonically from about 2 (-17) to 1 (-18) cm^2.

The simplified differential equations relating the various beam components may be written as

$$\begin{aligned} DF^+(\pi) &= -\sigma_{10} F^+(\pi) + \sigma_{01} F^\circ(\pi) \\ DF^\circ(\pi) &= -(\sigma_{01}+\sigma_{0T})F^\circ(\pi) + \sigma_{10} F^+(\pi) + \sigma_{T0} F^-(\pi) \\ DF^-(\pi) &= -\sigma_{T0} F^-(\pi) + \sigma_{0T} F^\circ(\pi) \end{aligned} \tag{A1}$$

where $D = \frac{d}{d\pi}$ (D is the differential operator)

$\pi = n(x)\ x$ (n is the target density at x)

$$F^i(\pi) = \frac{I^i(\pi)}{I_{tot}} .$$

Naturally since the equations are written in terms of fractions,

$$F^\circ + F^+ + F^- = 1 . \tag{A2}$$

For this work the ion fraction of interest is the so-called "neutral fraction" (F°). A straightforward but tedious method of solving the system of equations for just F° is to differentiate the second of (A1), substitute for the various derivatives and eliminate F^-. A more powerful and elegant method is given in Section 2. Either way after some algebraic manipulations the following equation emerges:

$$D^2F^0 + (\sigma_{10} + \sigma_{01} + \sigma_{T0} + \sigma_{0T})\, DF^0$$

$$+ \left[(\sigma_{10}+\sigma_{01})(\sigma_{T0}+\sigma_{0T}) - \sigma_{01}\sigma_{0T}\right] F^0 = \sigma_{10}\sigma_{T0} \quad . \tag{A3}$$

The solution is

$$F^0(\pi) = Ae^{-\alpha\pi} + Be^{-\beta\pi} + C \tag{A4}$$

where

$$\alpha = p + q \tag{A5}$$

$$\beta = p - q \tag{A6}$$

$$p = \tfrac{1}{2}(\sigma_{10} + \sigma_{01} + \sigma_{T0} + \sigma_{0T}) \tag{A7}$$

$$q^2 = p^2 - \gamma \tag{A8}$$

$$\gamma = (\sigma_{10} + \sigma_{01})(\sigma_{T0}+\sigma_{0T}) - \sigma_{01}\sigma_{0T} \quad . \tag{A9}$$

In order to evaluate A and B let

$$F^+(\pi) = aAe^{-\alpha\pi} + bBe^{-\beta\pi} + cC$$
$$F^-(\pi) = rAe^{-\alpha\pi} + sBe^{-\beta\pi} + tC \quad . \tag{A10}$$

By substituting into (A1) it is seen that

$$a = \frac{\sigma_{01}}{\sigma_{10} - \alpha}$$

$$b = \frac{\sigma_{01}}{\sigma_{10} - \beta}$$

$$c = \frac{\sigma_{01}}{\sigma_{10}} \qquad \text{(A11)}$$

$$r = \frac{\sigma_{0T}}{\sigma_{T0} - \alpha}$$

$$s = \frac{\sigma_{0T}}{\sigma_{T0} - \beta}$$

$$t = \frac{\sigma_{0T}}{\sigma_{T0}}$$

The proper boundary conditions for $\pi = 0$ are now inserted. The case of a pure proton beam has been solved before.[100] There the equations were solved for the positive fraction. Here, as a result of solving for the neutral beam, the equations exhibit symmetry under the exchange of +1 and -1 in the cross sections. An example is the values of a and r.

In this work the boundary conditions are for a mixed initial beam, i.e.,

$$F^{+}(0) = 1 - \delta - \epsilon$$

$$F^{\circ}(0) = \delta \qquad \text{(A12)}$$

$$F^{-}(0) = \epsilon$$

Then the system may be cast into matrix formulation.

$$\begin{pmatrix} 1-\delta-\epsilon \\ \delta \\ \epsilon \end{pmatrix} = \begin{pmatrix} a & b & c \\ 1 & 1 & 1 \\ r & s & t \end{pmatrix} \begin{pmatrix} A \\ B \\ C \end{pmatrix} . \tag{A13}$$

This is in the standard form ($\vec{y} = A\,\vec{x}$) with a known vector ($\vec{y}$), a matrix of coefficients (A) and the unknown vector ($\vec{x}$). To solve (A13) express the vectors as a sum of vectors so that x and y are

$$\begin{aligned} X &= X^0 + \delta X^1 + \epsilon X^2 \\ y &= y^0 + \delta y^1 + \epsilon y^2 \end{aligned} \tag{A14}$$

where

$$Y^0 = \begin{pmatrix} 1 \\ 0 \\ 0 \end{pmatrix}, \; Y^1 = \begin{pmatrix} -1 \\ 1 \\ 0 \end{pmatrix}, \; Y^2 = \begin{pmatrix} -1 \\ 0 \\ 1 \end{pmatrix} . \tag{A15}$$

Equation (A13) now becomes three separate matrix equations

$$Y^0 = Ax^0 \tag{A16}$$

$$Y^1 = Ax^1 \tag{A17}$$

$$Y^2 = Ax^2 . \tag{A18}$$

Equation (A16) is that of a pure proton beam mentioned above. Its solution is

$$A^{\circ} = \frac{t-s}{\Delta}$$

$$B^{\circ} = \frac{r-t}{\Delta}$$

$$C^{\circ} = \frac{s-r}{\Delta} \qquad \text{(A19)}$$

where

$$\Delta = \det \begin{vmatrix} a & b & c \\ 1 & 1 & 1 \\ r & s & t \end{vmatrix} \qquad \text{(A20)}$$

The solutions of (A17) and (A18) are respectively

$$A' = \frac{s(1+c) - t(1+b)}{\Delta}$$

$$B' = \frac{t(1+a) - r(1+c)}{\Delta}$$

$$C' = \frac{r(1+b) - s(1+a)}{\Delta}$$

$$A^{2} = \frac{b-c+s-t}{\Delta} \qquad \text{(A21)}$$

$$B^{2} = \frac{c-a+t-r}{\Delta}$$

$$C^{2} = \frac{r-s+a-b}{\Delta}$$

Note that

$$A^0 + B^0 + C^0 = 0$$
$$A^1 + B^1 + C^1 = 1 \qquad \text{(A22)}$$
$$A^2 + B^2 + C^2 = 0$$

so that this satisfies the second of Equations (A12).

In summary, calculations yield

$$A=\left[\{t-s\}+\delta\{s(1+c)-t(1+b)\}+\epsilon\{b-c+s-t\}\right]\Delta^{-1} \qquad \text{(A23)}$$

$$B=\left[\{r-t\}+\delta\{t(1+a)-r(1+c)\}+\epsilon\{c-a+t-r\}\right]\Delta^{-1} \qquad \text{(A24)}$$

$$C=\left[\{s-r\}+\delta\{r(1+b)-s(1+a)\}+\epsilon\{r-s+a-b\}\right]\Delta^{-1} \qquad \text{(A25)}$$

$$\Delta = a(t-s)+b(t-r)+c(s-r) \qquad \text{(A26)}$$

A.2. Alternate Derivation of the Basic Equation

This section is for those enamored with matrix manipulations. An alternate (and faster) derivation of Equation (A4) is given here.[101] Equation (A1) may be cast into the following matrix form:

$$DF = AF \qquad \text{(A27)}$$

where D is the differential operator mentioned before and

$$F = \begin{pmatrix} F^{+} \\ F^{o} \\ F^{-} \end{pmatrix} \tag{A28}$$

$$A = \begin{pmatrix} -\sigma_{10} & \sigma_{01} & 0 \\ \sigma_{10} & -(\sigma_{01}+\sigma_{0T}) & \sigma_{T0} \\ 0 & \sigma_{0T} & -\sigma_{T0} \end{pmatrix} . \tag{A29}$$

Now let

$$F = VG \tag{A30}$$

where the matrix V is so chosen that it is independent of and G and $V^{-1}AV$ is a diagonal matrix. Then (A30) becomes

$$DG = V^{-1}AVG \tag{A31}$$

Let a_i be the i^{th} eigenvalue of A. Then each component of Equation (A31) can be easily integrated to yield equations of the form

$$G_i = G_i^{o} \exp\{a_i \pi\} \tag{A32}$$

Use (A30) to solve for F. Then the i^{th} component of the F vector, which is some charge component, satisfies

$$F_i(\pi) = \sum_j C_{ij} \exp\{a_i \pi\} \quad . \tag{A33}$$

In the problem considered here

$$\sum_j C_{ij} = F_i(0)$$
$$\sum_{i,j} C_{ij} = 1 \quad . \tag{A34}$$

The eigenvalues of A satisfy

$$a\left[a^2 + 2p\,a + \gamma\right] = 0 \tag{A35}$$

where p is given by (A7) and γ by (A9). Hence

$$a = 0,\ -p-q\ ,\ -p+q \tag{A36}$$

and Equation (A33) is just (A4).

A.3. Exact Evaluation of the Coefficients

It is usually assumed that the thick target asymptote is very nearly that of the two charge system, i.e.,

$$C_2 = \frac{\sigma_{10}}{\sigma_{10} + \sigma_{01}} \quad . \tag{A37}$$

The actual value is given by Equation (A25)

$$C \doteq \frac{\left[\{s-r\}+\delta\{r(1+b)-s(1+a)\}+\epsilon\{r-s+a-b\}\right]}{\Delta} \quad . \tag{A25}$$

With a bit of difficulty it can be shown that (A25) is

$$C = C_2 \mu \tag{A38}$$

where C_2 is given by (A37) and

$$\mu = \left[1 + \frac{\sigma_{0T}}{\sigma_{T0}} C_2\right]^{-1} \quad . \tag{A39}$$

C does not depend on either δ or ϵ. This implies that if a beam were to traverse several thick target regions, the equilibrium fractions would be characteristic of the last zone encountered. The beam forgets the others.

This lack of hysteresis can be seem merely by considering Equations (A1) for a thick target ($\pi \to \infty$). The left sides all vanish. Two simple relationships appear -

$$\begin{aligned} F^{+}(\infty) &= \frac{\sigma_{01}}{\sigma_{10}} F^{\circ}(\infty) \\ F^{-}(\infty) &= \frac{\sigma_{0T}}{\sigma_{T0}} F^{\circ}(\infty) \end{aligned} \quad . \tag{A40}$$

The equilibrium value for F° (C) is found to be

$$F^{\circ}(\infty) = \frac{\sigma_{10}\,\sigma_{T0}}{\sigma_{T0}(\sigma_{10}+\sigma_{01}) + \sigma_{01}\,\sigma_{0T}} \quad . \tag{A41}$$

This is another form of (A38). It is independent of the boundary conditions at zero density. Also the second of Equations (A40) becomes

$$F^{-}(\infty) = 1 - \mu \quad . \tag{A42}$$

Typical values for a thick target are $F^{\circ}(\infty) \sim \frac{1}{2}$ and $F^{-}(\infty) \sim 1/100$. The ratio of the cross sections in the definition of μ is quite small. The two component system should have asymptotes very close to those of the 3 component system.

The coefficients of the exponentials do depend on δ and ϵ. Equations (A23) and (A24) become

$$A = A^{\circ}\left[1 - \delta\left\{1 + \left(\frac{\sigma_{01}}{\sigma_{10}}\right)\frac{\sigma_{10}-\sigma_{T0}}{\sigma_{10}-\beta}\right\} - \epsilon\left\{1 + \frac{\sigma_{01}\,\sigma_{T0}}{\sigma_{10}\,\sigma_{0T}}\left(\frac{\sigma_{T0}-\beta}{\sigma_{10}-\beta}\right)\right\}\right]$$

$$B = B^{\circ}\left[1 - \delta\left\{1 + \left(\frac{\sigma_{01}}{\sigma_{10}}\right)\frac{\sigma_{T0}-\sigma_{10}}{\sigma_{10}-\alpha}\right\} - \epsilon\left\{1 + \frac{\sigma_{01}\,\sigma_{0T}}{\sigma_{10}\,\sigma_{T0}}\left(\frac{\sigma_{T0}-\alpha}{\sigma_{10}-\alpha}\right)\right\}\right] \quad . \tag{A43}$$

The superscripted terms are given by (A19). They become

$$A^\circ = \frac{\sigma_{10}\,\sigma_{0\bar{1}}\,(\sigma_{10}-\sigma_{\bar{1}0})}{2q\alpha\,(\sigma_{\bar{1}0}-\beta)}$$

$$B^\circ = \frac{\sigma_{10}\,\sigma_{0\bar{1}}\,(\sigma_{\bar{1}0}-\sigma_{10})}{2q\beta\,(\sigma_{\bar{1}0}-\alpha)} \qquad \text{(A44)}$$

Both the coefficient of the faster dying exponential, which here is A, and the longer lived term will not be used here in their full gory forms. Approximations can be used. The cross sections so found can be tested by substituting them into the exact forms.

A.4. Approximate Forms for the Coefficients

By brute force one can calculate the ratios A°/C and B°/C. A°/C is approximately

$$\frac{A^\circ}{C} = \begin{cases} \dfrac{\sigma_{0\bar{1}}}{\sigma_{\bar{1}0}}\,\dfrac{(\sigma_{10}+\sigma_{01})(\sigma_{10}-\sigma_{\bar{1}0})}{|D|^2} & D<0 \\ \dfrac{\sigma_{10}-\sigma_{\bar{1}0}}{2\sigma_{01}} & |D|\approx 0 \\ -1+\dfrac{\sigma_{0\bar{1}}}{\sigma_{\bar{1}0}-\sigma_{10}} & D>0 \end{cases} \qquad \text{(A45)}$$

where D is defined as $\sigma_{10} + \sigma_{01} - \sigma_{\bar{1}0} - \sigma_{0\bar{1}}$. The ratio of B° to C is obtained by substituting -D for D in (A45). Only two distinct cases exist; either one coefficient is large and the other very small or both are approximately equal. Furthermore, if $\sigma_{\bar{1}0} > \sigma_{10}$, then both coefficients will be negative. The maximum value is -C.

Since the two charge state should be a good approximation, (A6) can be written in the nice form

$$F^{o}(\pi) = G(\pi) + g(\pi) \tag{A46}$$

where

$$\begin{aligned} G_1(\pi) &= (C-\delta)\left[1-e^{-\alpha\pi}\right] + \delta \\ g(\pi) &= B\left(e^{-\beta\pi} - e^{-\alpha\pi}\right) \end{aligned} \tag{A47}$$

The first term in (A47) is just (2.10), the two component equation. The H^- fraction should influence the correction (A47 Bottom) strongly. Definitions (A5) - (A9) indicate that β should be affected more by H^- than α.

There should be enough information in the difference expression (A47 Bottom) to determine two more cross sections ($\sigma_{\bar{1}0}$ and $\sigma_{0\bar{1}}$). Three things are particularly useful in this correction. The low density slope of the curve, its total area, and the position of the maximum can be conveniently used to find the negative ion cross sections. Any two of these will be sufficient for $\sigma_{\bar{1}0}$ and $\sigma_{0\bar{1}}$. The third one can be used to verify the values. The peak could be easily missed. This one will be the check. The slope (m_o), the area (S), and the peak position (π_{max}) are given by

$$\begin{aligned} m_o &= 2_q B \\ S &= \frac{2_q B}{p^2 - q^2} \\ \pi_{max} &= \frac{1}{2_q} \ln\left\{\frac{p+q}{p-q}\right\} \end{aligned} \tag{A48}$$

The peak position can be approximated as $1/\alpha$.

The first approximation (2.9) yields α, S and C. The ratio of the area to the slope can then be used to find β. The slope gives B immediately. The boundary conditions fix A. The coefficient C is just the asymptote given by (2.14). The two known cross sections (σ_{10} and σ_{01}) are substituted into Equation (A9) and then (A7) yields all four cross sections. This can be iterated to give the best values for σ_{10} and σ_{01}. As a check the position of the maximum difference (π_{max}) can be calculated. Whenever all four values are known, the fit to (A6) can be compared with the data.

The two charge state predicts a simple linear equation for the neutral fraction behavior near zero density. For small π Equation (A4) becomes

$$F^{\circ}(\pi) = \delta - A(p+q)\pi - B(p-q)\pi \quad . \tag{A49}$$

This can be rewritten as

$$F^{\circ}(\pi) = \delta + \sigma_{10}\left[1 - \delta\left(\frac{\sigma_{10}+\sigma_{01}}{\sigma_{10}}\right) - \lambda\right]\Lambda\pi \tag{A50}$$

where

$$\lambda = (1-\mu) + (A-B)q/\sigma_{10}\Lambda$$

$$\Lambda = \frac{P}{\sigma_{10}+\sigma_{01}} = 1 - \frac{DC_2}{2\sigma_{10}} \quad . \tag{A51}$$

The first of (A51) can be approximated as

$$\lambda = \begin{cases} \left\{1 - \dfrac{\sigma_{01}}{\sigma_{\bar{1}0} - \sigma_{10}}\right\} \dfrac{-D}{|D|} & |D| >> 1 \\ \dfrac{C_2 D}{2\Lambda\sigma_{10}} \left\{1 - \dfrac{\sigma_{01}}{\sigma_{\bar{1}0} - \sigma_{10}}\right\} & |D| > 0 \\ \left(\dfrac{\sigma_{01}}{\sigma_{\bar{1}0}}\right) C_2 & |D| \approx 0 \end{cases} \qquad \text{(A52)}$$

Equation (A50) is to be compared with

$$F^{\circ}(\pi) = \delta + \sigma_{10}\left[1 - \delta\left(\frac{\sigma_{10} + \sigma_{01}}{\sigma_{10}}\right)\right]\pi \qquad \text{(2.12)}$$

The terms are similar but their near equality depends on a fortuitous set of cross section values, i.e., D small.

A.5. Hydrogen Molecular Ion as the Probe

In addition to the proton beam discussed above, runs were made with the H_2^+ beam on both sodium and potassium. The interpretation of this data is more difficult than for proton beams.

In the following reactions X is the target alkali atom. The capital letter refers to the cross section for the reaction proceeding left to right. The corresponding small letter is for the reverse reaction. For example, σ_G here is σ_{10} above and σ_g is the electron capture cross section. This system is somewhat simplified for negative ion formation is not considered. There is also no distinction between

the various possible excited and ground states.

$$
\begin{aligned}
H_2^+ + X &\underset{a}{\overset{A}{\rightleftharpoons}} H_2 + X^+ \\
H_2^+ + X &\underset{b}{\overset{B}{\rightleftharpoons}} H^+ + H + X^+ \\
H_2^+ + X &\underset{c}{\overset{C}{\rightleftharpoons}} H + H + X^+ \\
H_2 + X^+ &\underset{d}{\overset{D}{\rightleftharpoons}} H^+ + H + X \\
H_2 + X^+ &\underset{e}{\overset{E}{\rightleftharpoons}} H + H + X^+ \\
H_2 + X &\underset{f}{\overset{F}{\rightleftharpoons}} H + H + X \\
H + X &\underset{g}{\overset{G}{\rightleftharpoons}} H + X^+
\end{aligned}
\qquad \text{(A53)}
$$

In the same manner as Appendix A.2 the differential equations for this set of charge transfer reactions become

$$DG = MG \qquad \text{(A54)}$$

where D is the differential operator

G is the vector of specie fractions

M is the matrix of cross sections.

In analogy to the earlier definitions the specie fractions are

$$
\begin{aligned}
G^o &= \frac{H_2}{T} \\
G^+ &= \frac{H_2^+}{T} \\
T &= H_2 + H_2^+ + H + H^+ \quad .
\end{aligned}
\qquad \text{(A55)}
$$

Consequently G is

$$G = \begin{pmatrix} G_1^\circ \\ G_1^+ \\ F^\circ \\ F^+ \end{pmatrix} \qquad \text{(A56)}$$

The matrix is

$$M = \begin{pmatrix} -m_0 & n & p & q \\ r & -m_+ & s & t \\ u & v & -l_0 & w \\ x & y & z & -l_+ \end{pmatrix} \qquad \text{(A57)}$$

The various elements of M are in turn defined as

$$\begin{aligned} m_0 &= \sigma_D + \sigma_E + \sigma_F + \sigma_a \\ n &= \sigma_A \\ p &= \sigma_d + \sigma_e + \sigma_f \\ q &= \sigma_d \\ m_+ &= \sigma_A + \sigma_B + \sigma_C \\ r &= \sigma_a \\ s &= \sigma_b + \sigma_c \\ t &= \sigma_b \\ l_0 &= \sigma_b + \sigma_c + \sigma_d + \sigma_e + \sigma_f + \sigma_g \\ u &= \tfrac{1}{2}\sigma_D + \sigma_E + \sigma_F \\ v &= \tfrac{1}{2}\sigma_B + \sigma_C \\ w &= \sigma_{G_1} \\ l_+ &= \sigma_b + \sigma_d + \sigma_{G_1} \end{aligned} \qquad \text{(A58)}$$

$$\begin{aligned} \alpha &= \tfrac{1}{2}\sigma_D \\ \gamma &= \tfrac{1}{2}\sigma_B \\ \beta &= \sigma_g \end{aligned}$$

Note that again

$$\begin{aligned} G^0 + G^+ + F^0 + F^+ &= 1 \\ DG^0 + DG^+ + DF^0 + DF^+ &= 0 \end{aligned} \tag{A59}$$

The factors in the exponents of the solution obey

$$\det \left| M - I\mu \right| = 0 \tag{A60}$$

After some manipulation the following fourth order equation emerges:

$$\mu^4 + P\mu^3 + Q\mu^2 + R\mu + S = 0 \tag{A61}$$

where

$$P = m_0 + m_+ + l_0 + l_+$$

$$\begin{aligned} Q = {} & (m_0 + m_+)(l_0 + l_+) + m_0 m_+ + l_0 l_+ \\ & - [t\gamma + w\beta + s\nu + r\eta + u\rho + x\xi] \end{aligned}$$

$$\begin{aligned} R = {} & m_0 m_+ (l_0 + l_+) + l_0 l_+ (m_0 + m_+) \\ & + t\gamma (m_0 + l_0) + w\beta (m_0 + m_+) + s\nu (m_0 + l_+) \\ & + sw\gamma + tv\beta - r\eta (l_+ + l_0) - r\xi\gamma - rp\nu \\ & - up (l_+ + m_+) - x\xi (l_0 + m_+) - uns \\ & - tn\alpha - wpx \end{aligned}$$

$$
\begin{aligned}
S = {} & m_o m_+ l_o l_+ + m_o (l_o t y + l_+ s v + s w y + t v z) \\
& + m_o m_+ w z - m_+ (l_+ u p + l_o q x + t n x) \\
& - \pi n l_o l_+ - \pi p w y - \pi q v z - \pi l_o q y - \pi p v l_+ \\
& - n z w \pi - u n s l_+ + u p t y + u q z v \\
& - u q s y - u t z n - \chi n s w - \nu p t v \\
& + q s v \chi
\end{aligned}
$$

Here P is the sum of all cross sections and S vanishes.

The equilibrium values (thick target) satisfy

$$MG = Z \tag{A62}$$

where Z is a vector with all null elements. This is again overspecified.

It becomes

$$\begin{pmatrix} -m_+ & s & t \\ v & -l_o & w \\ y & z & -l_+ \end{pmatrix} \begin{pmatrix} g_1 \\ g_2 \\ g_3 \end{pmatrix} = \begin{pmatrix} -r \\ -u \\ -\nu \end{pmatrix} \tag{A63}$$

where

$$g_1 = G^+/G^o$$
$$g_2 = F^o/G^o$$
$$g_3 = F^+/G^o$$

The normalization equation (Equation (A59) Top) implies

$$G^o = \left[1 + g_1 + g_2 + g_3\right]^{-1} \tag{A64}$$

The difficulties with the hydrogen molecular ion beam should now be obvious. There are 14 cross sections to be measured and four beam components. Each component will be a complicated function of π: three exponentials and a constant. This experiment measures only the total neutral flux. The ratio of neutral flux to total flux (R) is

$$R = G^{o}(1 + \chi g_2) \tag{A65}$$

where χ is the fraction of the hydrogen atoms reaching the detector. If the dissociation products gain energy from the interaction with the target, χ should be nearly zero.

For linear data runs (π small) only single scattering reactions are important. Then

$$\begin{aligned} G_1^{+} &= 1 - (\sigma_A + \sigma_B + \sigma_C)\pi \\ G_1^{o} &= \sigma_A \pi \\ F^{+} &= \tfrac{1}{2}\sigma_B \pi \\ F^{o} &= (\tfrac{1}{2}\sigma_B + \sigma_C)\pi \\ R &= \left[\sigma_A + \chi\left(\tfrac{1}{2}\sigma_B + \sigma_C\right)\right] . \end{aligned} \tag{A66}$$

If σ_A and σ_a are the dominant cross sections, then the hydrogen ion components behave as the proton ones did above in Sections 2.2.

APPENDIX B

TRANSITION PROBABILITIES

In Section 2.5 the equations for the time dependent hydrogen level populations were derived. They depend upon the Einstein A coefficients. It was discovered that all substates through n = 12 were needed. Various groups[60,102] have compiled these coefficients through n = 6. Hence it was necessary to compute the rest. A large number of radial hydrogenic integrals have been calculated.[102,103] These were used to determine the required probabilities. The coefficients are related to these integrals through

$$A(n,\ell;n',\ell') = \frac{64\pi^4\nu^3}{3hc^3}\ \frac{\max(\ell,\ell')}{2\ell+1} \times\ e^2a_o^2\left[\int_0^\infty R(n',\ell')\,r\,R(n,\ell)\,dr\right]^2 \tag{B1}$$

where

$$\max(\ell,\ell') = \begin{cases} \ell & \text{for } \ell > \ell' \\ \ell' & \text{for } \ell < \ell' \end{cases} .$$

Four digit values were used for the integrals. The resulting coefficients were then verified by comparison with existing values. It was then discovered that a number of mistakes appear in Condon and Shortley.[102] They are listed in Table B1. The average transition probability is defined by

$$\bar{A}(n) = \frac{1}{n^2} \sum_{\ell=0}^{\ell=n-1} (2\ell+1) A(n,\ell;n',\ell') \qquad n>n' \quad . \tag{B2}$$

Values for this average probability have been tabulated[60] for principal quantum numbers 2 through 20. The average values from this work agree well with those other ones. (See Table B2)

One further check is possible. Various approximations exist for the average lifetime of a state. For example,[104] according to Bohr's correspondence principle, in the limit of large quantum numbers the power radiated is equal to

$$P = \frac{\hbar\omega}{\tau} \tag{B3}$$

where $1/\tau$ is the reciprocal mean lifetime (the transition probability) and ω is the orbital frequency. For hydrogen the probability for a transition from the circular orbit characterized by quantum number n to (n-1) is

$$\frac{1}{\tau} = \frac{2}{3}\left(\frac{\alpha}{n}\right)^5 \frac{m_e c^2}{\hbar} \tag{B4}$$

where α is the fine structure constant and m_e is the electron mass.

Bethe and Salpeter[105] fitted data and decided that the lifetime is approximately

$$\tau \simeq \tau_o \, n^{4.5} \tag{B5}$$

where $\tau_o = 2.66\,(9)\ \text{sec}^{-1}$. May[56] placed limits on the lifetime. He discovered

$$\frac{\tau_o \, n^4}{8 \ln(n)} < \tau(n) < \tau_o \frac{n^5}{4} \tag{B6}$$

where the upper limit is just Equation (B4) rewritten. There is another formulation which shows that the lifetime depends on the total quantum number j. Table B2 lists some of these quantities.

APPENDIX C

CALCULATION OF THE METASTABLE LIFETIME

The lifetime of the metastable $2S_{\frac{1}{2}}$ level of hydrogen has been investigated both theoretically[56-59,106,107] and experimentally[10,31,103] Under the influence of a weak electric field the Stark effect mixes the metastable state with the resonant 2P levels. It is assumed that the field is so weak that only the n = 2 levels mix together. This implies any splitting is comparable to the 2P doublet splitting (about 45 μeV) but is much less than the separation of the n = 2 and n = 3 levels (on the order of 1 eV). This perturbation is

$$h_s = -eE_z = -eE\ r\ \cos\theta \quad . \tag{C1}$$

Since h_s is an odd parity function of θ, the only nonvanishing matrix elements are those between states of different parity. Furthermore h_s does not depend upon either the angle φ or the spin. The only states that are mixed are those that obey $\Delta m_\ell = 0$ and $\Delta m_s = 0$.

For simplicity assume the unperturbed Hamiltonian exactly selects the $2P_{3/2}$ energy. This is taken as the zero energy point. It is convenient to rename the states so that "a" refers to the $2S_{\frac{1}{2}}$ state, "b" to $2P_{\frac{1}{2}}$ and "c" to the mixing $2P_{3/2}$ states. The unmixed states will be designated "r" and the "g" state is the $1S_{\frac{1}{2}}$ ground state. The behavior of the four excited states as the electric field strength varies is depicted in Figure C-1. Separation energy is measured in millikaysers [1K = 1 cm^{-1}] with respect to the "r" state. Similarly, Figure C-2 shows the change in the "a" or metastable state as a function of field strength.

In this representation the Hamiltonian $\mathcal{H}$, which satisfies the standard eigenvalue equation, can be broken into unperturbed and

perturbed pieces several ways. In this Appendix it is written as

$$\mathcal{H} = H + h = H + h_{\vec{L}\cdot\vec{S}} + h_s \qquad (C2)$$

where

$H\Psi = \mathcal{E}_o\Psi$

$\mathcal{E}_o$ = is the r state energy

$h_{\vec{L}\cdot\vec{S}}$ is the spin interaction that splits the other states.

This term creates the diagonal values of Equations (C9) and (C10).

One convenient representation for the levels is to give the orbital and spin angular momenta and their projections. A typical designation is $|\ell s m_\ell m_s>$. In this case s is always one half and hence superfluous. The perturbation couples $|\ell s m_\ell \uparrow>$ and $|\ell' s' m'_\ell \uparrow>$ states, for example. To simplify matters only the states with $m_s = \frac{1}{2}$ will be discussed. These results are the same as those for the $-\frac{1}{2}$ states. The simplified representation becomes $|\ell m_\ell>$. Thus the lettered states become

$$\begin{aligned} |g\rangle &= |00\rangle \\ |a\rangle &= |00\rangle \\ |b\rangle &= |10\rangle \\ |c\rangle &= |10\rangle \\ |r\rangle &= |1\,{-1}\rangle,\ |11\rangle \ . \end{aligned} \qquad (C3)$$

In order to evaluate the matrix elements, the following relationships are useful:

$$\int_0^\infty r^n e^{-r/a}\, dr = a^{n+1}\, n! \qquad (C4)$$

$$Y_{0,0} \cos\Theta = \frac{1}{\sqrt{3}}\, Y_{1,0}$$

A typical matrix element to be considered is $\langle c/a \rangle$. For the Schrodinger hydrogen atom this is

$$\langle c|a\rangle = -eE\int_0^\infty dr\; r^4 \frac{e^{-r/a_0}(2-r/a_0)}{(2a_0)^3\, a_0\sqrt{3}} \times \int_0^{4\pi} d\Omega \cos\Theta\, Y_{0,0}\sqrt{\frac{2}{3}}\, Y_{1,0}^* \qquad (C5)$$

Equation (C5) can be evaluated with the aid of (C4) as

$$\langle c|a\rangle = \sqrt{2}\,\eta \qquad (C6)$$

where

$$\eta = \sqrt{3}\, eE a_0 \qquad (C7)$$

Similarly

$$\langle b|a\rangle = \eta \qquad (C8)$$

The quantity a_0 is the first Bohr radius. Its numerical value is .529 (-8) cm. Again it should be pointed out that throughout this work the notation D(P) means D x 10^P.

When the fine structure is taken into account, the total perturbation matrix becomes

$$h_t = \begin{pmatrix} \mathcal{E}_a & \eta & \sqrt{2}\,\eta \\ \eta & \mathcal{E}_b & 0 \\ \sqrt{2}\,\eta & 0 & 0 \end{pmatrix} \qquad \text{(C9)}$$

where $h_t = h_L^{\rightarrow}\cdot\vec{S} + h_s$. In (C9) all energies are measured with respect to the energy of the unmixed states ($\mathcal{E}_o$). $\mathcal{E}_a$ is the energy of state "a" with respect to "r" and $\mathcal{E}_b$ the energy of "b". $\mathcal{E}_a$ and $\mathcal{E}_b$ are both negative. If the $2P_{3/2}$ state is neglected, the reduced perturbation matrix becomes

$$h_r = \begin{pmatrix} \mathcal{E}_a & \eta \\ \eta & \mathcal{E}_b \end{pmatrix} . \qquad \text{(C10)}$$

Two approaches were taken in evaluating the mixing coefficients. If standard second order non-degenerate perturbation theory[109] is applied, then one finds the energy W_a and the wave function $|\psi_a\rangle$ for h_s to be

$$W_a = \mathcal{E}_a + \eta^2\left\{\frac{1}{\mathcal{E}_a-\mathcal{E}_b} + \frac{2}{\mathcal{E}_a}\right\}$$

$$|\psi_a\rangle = a_1|a\rangle + a_2|b\rangle + a_3|c\rangle$$

$$a_1 = 1 - \tfrac{1}{2}\eta^2\left\{\frac{1}{(\mathcal{E}_a-\mathcal{E}_b)^2} + \frac{2}{\mathcal{E}_a{}^2}\right\}$$

$$a_2 = \frac{\eta}{\mathcal{E}_a-\mathcal{E}_b}\,, \qquad a_3 = \frac{\sqrt{2}\,\eta}{\mathcal{E}_a} . \qquad \text{(C11)}$$

Only the coefficients a_2 and a_3 will be affected by third order theory and have a term of order η^3. This result (C11) yields the standard Bethe approximation[57] for the lifetime (Equation (2.43)):

$$\frac{1}{\tau} = 2780\ E^2 \quad .$$

In the dipole approximation the transition probability per unit time for spontaneous emission from state k to n is

$$\gamma_{kn} = \frac{4e^2\omega_{kn}^3}{3\hbar c^3}\left|\vec{r}_{kn}\right|^2 \qquad \text{(C12)}$$

where $\omega_{kn} = \left|E_k - E_n\right| / \hbar$

and $\vec{r}_{kn}$ is the dipole matrix element.

For the resonant 2P-1S transition this element is

$$\vec{r}_{21} = \frac{2^{15/2}}{3^5}\, a_0 \quad . \qquad \text{(C13)}$$

It is convenient to introduce the notation

$$\Gamma = \left(\frac{2}{3}\right)^8 \alpha^4 \frac{c}{a_0} \qquad \text{(C14)}$$

where α is the fine structure constant. Γ has the value 6.27 (8) sec^{-1}. The energy of the n^{th} hydrogen level is

$$E_n = -\frac{e^2}{2a_0 n^2} \quad . \qquad \text{(C15)}$$

This implies

$$\omega_{21} = \frac{3}{8}\frac{c}{a_0}\alpha \quad . \tag{C16}$$

Hence Equation (C12) becomes

$$\gamma_s = \Gamma\eta^2\left\{\frac{1}{(\varepsilon_a-\varepsilon_b)^2} + \frac{2}{\varepsilon_a^2}\right\} \quad . \tag{C17}$$

The second approach will be done in somewhat greater detail. It is exact diagonalization of the perturbation matrix (Equation (C9)). This method[106] has been applied to this problem before, albeit incorrectly. In order to examine the effect of the $2P_{3/2}$ state on the metastable lifetime, Equation (C10) will be solved first.

The secular determinant to be solved is

$$\begin{vmatrix} \varepsilon_a-\lambda & \eta \\ \eta & \varepsilon_b-\lambda \end{vmatrix} = 0 \quad . \tag{C18}$$

The eigenvalues satisfy the simple quadratic equation

$$(\varepsilon_a-\lambda)(\varepsilon_b-\lambda) = 0 \quad . \tag{C19}$$

The roots of (C19) are

$$\begin{aligned} \lambda_1 &= \langle\varepsilon\rangle - \tfrac{1}{2}\sqrt{\varepsilon_L^2 + 4\eta^2} \\ \lambda_2 &= \langle\varepsilon\rangle + \tfrac{1}{2}\sqrt{\varepsilon_L^2 + 4\eta^2} \end{aligned} \tag{C20}$$

where

$$\langle \mathcal{E} \rangle = \frac{\mathcal{E}_a + \mathcal{E}_b}{2}$$

$$\mathcal{E}_L = \mathcal{E}_b - \mathcal{E}_a \qquad \text{(C21)}$$

The magnitude of $\mathcal{E}_L$ (the Lamb shift) is about 4.5 μeV (1058 MHz).

Let

$$E = A - \lambda I \qquad \text{(C22)}$$

then

$$EX = 0 \qquad \text{(C23)}$$

The determinant of E is just Equation (C18). Equation (C23) is to be solved for the eigenvector X corresponding to each particular eigenvalue λ. Since the determinant vanishes, the components of each eigenvector are over-determined and hence have many possible values. This degeneracy can be removed by forcing the eigenvector to be normalized. For this case the equation is

$$|a_1|^2 + |a_2|^2 = 1 \qquad \text{(C24)}$$

It will be useful to partition E. It is shown in standard mathematical texts[110] that matrix manipulations are as valid for matrices as they are for elements of matrices. Equation (C23) becomes

$$EX = \left(\begin{array}{c|c} S & R \\ \hline C & M \end{array}\right)\begin{pmatrix} X_1 \\ X_i \end{pmatrix} = 0 \qquad \text{(C25)}$$

where S is a 1 x 1 matrix (really just $E_{1,1}$)

R is a 1 x (n-1) row matrix

C is an (n-1) x 1 column matrix

M is an (n-1) x (n-1) matrix

X_1 is the first element of the X vector of (C23)

X_i is the (n-1) element vector which was the rest of X.

Then Equation (C23) becomes

$$\begin{aligned} SX_1 \times RX_i &= 0 \\ CX_1 + MX_i &= 0 \end{aligned} \qquad (C26)$$

This system of equations could be solved if the determinant did not vanish. But from Equation (C18) it is seen that

$$SM - RC = 0 \qquad (C27)$$

Since Equations (C26) are redundant, pick the last of them to solve for the ratio X_i/X_1. Then the equation is cast in the standard matrix form of $\vec{y} = A\vec{x}$. Also consider the solution of M using Cramer's rule. Then X_1 is easily seen to be proportional to the determinant of M.

For the 2 x 2 version of E, M is a single element. M is a simple 2 x 2 matrix for the full treatment of this lifetime calculation (Equation (C30)).

For the reduced matrix (C10)

$$\begin{aligned} Na_1 &= \mathcal{E}_b - \lambda_1 \\ Na_2 &= -\eta \end{aligned} \qquad (C28)$$

It is readily shown that these satisfy (C23). If Equation (C24) is used to determine N, one finds that [to within an overall sign]

$$a_1 = \frac{\varepsilon_b - \lambda_1}{\sqrt{(\varepsilon_b - \lambda)^2 + \eta^2}}$$
$$a_2 = \frac{-\eta}{\sqrt{(\varepsilon_b - \lambda)^2 + \eta^2}} \quad . \tag{C29}$$

These are shown in Figure C-2.

Consider now the 3 x 3 case represented by Equation (C9). In the same way one obtains the secular determinant

$$\begin{vmatrix} \varepsilon_a - \lambda & \eta & \sqrt{2}\,\eta \\ \eta & \varepsilon_b - \lambda & 0 \\ \sqrt{2}\,\eta & 0 & -\lambda \end{vmatrix} = 0 \tag{C30}$$

the eigenvalue equation

$$\lambda^3 - \lambda^2(\varepsilon_a + \varepsilon_b) + \lambda(\varepsilon_a \varepsilon_b - 3\eta^2) + 2\varepsilon_b \eta^2 = 0 \tag{C31}$$

and the eigenvectors

$$\begin{aligned} N a_1 &= -(\varepsilon_b - \lambda)\,\lambda \\ N a_2 &= \eta\,\lambda \\ N a_3 &= -\sqrt{2}\,\eta\,(\varepsilon_b - \lambda) \end{aligned} \tag{C32}$$

where

$$N^2 = (\varepsilon_b - \lambda)^2 \lambda^2 + \eta^2 \lambda^2 + 2\eta^2 (\varepsilon_b - \lambda)^2 \quad . \tag{C33}$$

There are two asymptotic regions of interest for each case: the small η region and the high η area. For the two state example the roots become

$$\lambda_1 = \mathcal{E}_a - \frac{1}{2}\frac{\eta^2}{\mathcal{E}_L}$$
$$\lambda_2 = \mathcal{E}_b + \frac{1}{4}\frac{\eta^2}{\mathcal{E}_L} \qquad \text{(C34)}$$

and the coefficients approach

$$a_1 = 1$$
$$a_2 = 0 \qquad \text{(C35)}$$

For large η the eigenvalues and eigenvectors become

$$\lambda = \pm \eta \qquad \text{(C36)}$$

$$a_1 = \frac{1}{2}$$

$$a_2 = \frac{1}{2} \qquad \text{(C37)}$$

Figure C-3 shows the effect of an external field on a_1 and a_2.

The three state example has the following zero field forms:

$$\lambda = \mathcal{E}_a, \mathcal{E}_b, 0 \qquad \text{(C38)}$$

$$a_1 = 1$$
$$a_2 = 0 \qquad \text{(C39)}$$
$$a_3 = 0$$

Of course for slightly larger fields the two state approximation holds.

The third root is $-\frac{2\eta^3}{a}$. For large fields ($\eta \gg \mathcal{E}_a + \mathcal{E}_b$) the secular equation becomes approximately

$$\lambda^3 - 3\eta^2\lambda = 0 \qquad (C40)$$

Its roots are

$$\lambda = 0, +\sqrt{3}\,\eta, -\sqrt{3}\,\eta \qquad (C41)$$

If the growth of the $|a>$ state energy eigenvalue is followed as the electric field increases, it becomes clear that the proper root is the small one. Then the cubic equation can be truncated to a simple linear one. It becomes

$$3\eta^2\lambda - 2\eta^2\mathcal{E}_b = 0 \qquad (C42)$$

Whence the small root is

$$\lambda = \frac{2}{3}\mathcal{E}_b \qquad (C43)$$

Since a_1 is independent of the electric field, it becomes negligible. Hence the coefficients approach

$$a_1 = 0$$
$$a_2 = (2/3)^{\frac{1}{2}}$$
$$a_3 = (1/3)^{\frac{1}{2}}$$

They are displayed as a function of the field in Figure C-4. The displacement of the "metastable" level appears in Figure C-3. Figure C-5

shows the metastable lifetime as a function of applied field. The two state value is the lower curve. The theoretical quadrupole lifetime ($1/\gamma_{QUAD}$) is added to this calculation in that plot. Breit and Teller[58] and Shapiro and Teller[59] have assigned it a value of about 1/7 of a second. A more recent calculation [107] changes it to 1/3 second.

$$\gamma_{TOT} = \gamma_{QUAD} + \gamma_S + \gamma_D \tag{C45}$$

$$\gamma_S = \Gamma (a_2^2 + a_3^2) \tag{C46}$$

$$\tau = 1/\gamma_{TOT} \tag{C47}$$

The third term in Equation (C45) is due to a projected permanent dipole moment in the atom. Fite et al.[31] have placed an upper limit on this moment. They deduced a lower limit of 2.4 msec. This is the same order as the earth field induced value of Section 5.3.2. It has been neglected in the figures for this appendix.

Similarly Equation (C8) can be solved for the resonance states. Then the following expansions occur:

$$\begin{aligned} |\psi_b\rangle &= b_1 |a\rangle + b_2 |b\rangle + b_3 |c\rangle \\ |\psi_c\rangle &= c_1 |a\rangle + c_2 |b\rangle + c_3 |c\rangle \end{aligned} \tag{C48}$$

For small fields only b_2 and c_3 are non-zero. For high fields the asymptotes become

$$b_1 = c_1 = (1/2)^{\frac{1}{2}}$$
$$b_2 = c_2 = (1/6)^{\frac{1}{2}} \qquad \text{(C49)}$$
$$b_3 = c_3 = (1/3)^{\frac{1}{2}}$$

As a result of (C49) the lifetime of the resonant states increases to $2/\Gamma$. The results of this calculation are shown in Figure C-6. The lifetimes of the two $2P_{3/2}$ substates that are not mixed remain at $1/\Gamma$. These are the "r" level in Figure C-1. Both C-1 and C-2 are drawn using the 3 state expansion and equations (C32) and (C33).

APPENDIX D

CALCULATION OF THE TWO WIRE FIELD

This is an appendix for those enamored with appendices. In order to calculate the expected lifetime behavior of the metastable atoms as they pass between the two wires which hang beneath the UV detector, it is necessary to know the electric field generated by these wires. The wires can be assumed to be cylinders of finite radius which are infinite in extent along the z axis. The beam path is the y axis. The oven lies in the negative y direction. The circular cross sections of the wires determine the x axis. Consider this problem as a stack of x-y planes. It then becomes a two-dimensional problem in any particular plane. It can be shown that the equipotential surfaces in the plane are circles. Further the electric field lines are arcs of circles that intersect the wires. It is known[111] that the equipotentials satisfy

$$\left[x - \left(\frac{m^2+1}{m^2-1}\right)s\right]^2 + y^2 = \left(\frac{2ms}{m^2-1}\right)^2 \qquad \text{(D1)}$$

where

$$m = \left[\frac{(x+s)^2 + y^2}{(x-s)^2 + y^2}\right]^{1/2} . \qquad \text{(D2)}$$

The center and the radius of an equipotential circle are both functions of the parameters s and m. M is the ratio of distances from the centers and s is a function of the wire separation and wire radius.

In this experiment one wire is at potential V and the other one is grounded. The potential at any point becomes

$$V(m) = A \ln(m) + \frac{V}{2} \quad . \qquad (D3)$$

The midplane of symmetry (the y axis) is at potential V/2. To evaluate the constant consider the potential difference between the midplane (m=1) and one wire ($m=m_o$). Then

$$A = \frac{V}{2 \ln(m_o)} \quad . \qquad (D4)$$

The separation between the wires (d) and the wire radius (r_o) determine m_o. The relevant equations are

$$\frac{d}{2} = \frac{m_o^2 + 1}{m_o^2 - 1} S \qquad (D5)$$

$$r_o = \frac{2 m_o S}{m_o^2 - 1} \quad . \qquad (D6)$$

Equations (D5) and (D6) are solved simultaneously to give

$$m_o^2 - m_o\left(\frac{d}{r_o}\right) + 1 = 0 \quad . \qquad (D7)$$

The roots are approximately

$$m_o = \begin{cases} \dfrac{d}{r_o} - \dfrac{r_o}{d} & d \gg r_o \\ \dfrac{r_o}{d} - \left(\dfrac{r_o}{d}\right)^3 & \end{cases} \quad . \qquad (D8)$$

Note that they obey the general rule for points symmetrically placed about the y axis

$$mm' = 1 \qquad (D9)$$

where the unprimed value refers to the positive y value and the primed one to the negative value.

S may now be evaluated. D is the distance between the wire centers. It is also the separation of the centers of the equipotentials for $m=m_o$ and $m'=m'_o$. Thus

$$d = \frac{m_o^2+1}{m_o^2-1} S - \frac{m_o'^2+1}{m_o'^2-1} S \quad . \qquad (D10)$$

Apply Equation (D9). Then Equation (D10) becomes (D5). Square and rearrange (D5) so that it becomes

$$S = \left[\left(\frac{d}{2}\right)^2 - r_o^2\right]^{1/2} \quad . \qquad (D11)$$

The field in Cartesian coordinates is

$$\vec{E}(x,y) = \frac{2sA}{\Delta^2}\left\{(x^2-s^2-y^2)\hat{\imath} + 2xy\,\hat{\jmath}\right\} \qquad \text{(D12)}$$

where

$$\Delta^2 = \left[(x+s)^2+y^2\right]\left[(x-s)^2+y^2\right] \quad . \qquad \text{(D13)}$$

The relevant quantity for the lifetime shortening is the magnitude of the field. It is

$$E = \frac{2sA}{\Delta} \quad . \qquad \text{(D14)}$$

Figures D-1 and D-2 show the equipotential curves and the equi-fields (curves of constant field magnitude) in an arbitrary z plane.

Typical values for this experiment are V = 600 volts, d = 1.25 cm, and r_o is the radius of 16 AWG wire (0.645 mm). Then $m_o = 5.17\,(-2)$, $m'_o \simeq 19$ and $s \simeq 1$ cm. The constant A is approximately -101 volts. All distances are in centimeters and voltages are in volts.

APPENDIX E

A SHORT DISCUSSION OF NORMAL ERRORS OF MEASUREMENTS

The error bars shown in the figures are just the statistical errors associated with the measurements. Systematic errors are discussed in the body of this paper. The random errors are assumed to be normally distributed, i.e., the measurements cluster around a mean value $\bar{x}$ and the probability of the number x_i appearing is

$$f(x_i) = A \exp\left\{-B(\bar{x}-x_i)^2\right\} \tag{E1}$$

where A and B are constants which depend upon the standard deviation (σ). The square of this quantity is conveniently defined as

$$\sigma^2 = \frac{\sum_{i=1}^{N} (\bar{x}-x_i)^2}{N-1} = \frac{\left[(\bar{x}-x)^2\right]}{N-1} \tag{E2}$$

where N points were taken and the square brackets indicate the enclosed quantity was summed. It is possible to derive the subsequent equations without recourse to this picture.[112]

Low order polynomials are assumed to represent the neutral beam data. In the "linear" region the beam is approximated by a linear function of target density. The two charge state exponential can be cast into this form by suitable algebraic manipulation. The basic idea is to choose parameters of the fitted polynomial such that the disagreement between actual and calculated values is smallest.

One minimizes the sums of the squares of these differences. This is the least squares method of curve fitting. In addition some measurements may be thought to be more accurate than others. Each datum can be assigned a weight. This factor is related to the errors to be discussed later. The sums are differentiated with respect to the several parameters. This generates a system of equations relating the known data points (x_i) to the erroneous measured values (y_i). For the above case the target density is assumed to be exact whereas the measured neutral fraction may contain errors. As long as the assumed functional form has an additive constant, the sum of the differences must be zero.

For example, the linear form ($y = a_o + a_1 x$) produces the following simple set of equations:

$$\begin{aligned} [y] - a_o N - a_1[x] &= 0 \\ [xy] - a_o[x] - a_1[x^2] &= 0 \end{aligned} \quad . \qquad \text{(E3)}$$

The sum of the squared differences becomes

$$\sigma^2 = [(y - a_o - a_1 x)^2]/(N-2) \quad . \qquad \text{(E4)}$$

Two pieces of information are used to determine the coefficients. Hence only N-2 data points are left to check the accuracy of these constants. For a P parameter fit the denominator would be N-P.

It is now assumed that all discrepancies between expected and measured values are caused by errors in the coefficients. Also there are P independent errors. It can be shown [113] that the standard deviations for a sum of independent measurements are related to the total standard deviation through

$$\sigma^2 = a_u^2 \sigma_u^2 + a_v \sigma_v^2 + \cdots \qquad \text{(E5)}$$

for $A_i = a_u u_i + a_v v_i + \cdots$. For a linear fit at a fixed x_i this becomes

$$d_i^2 = 1\alpha_o^2 + x_i \alpha_1^2 \qquad \text{(E6)}$$

where α_o is the error in a_o and d_i in the i^{th} difference. For all N data points Equation (E6) sums to

$$\alpha^2 = N\alpha_o^2 + [x^2]\alpha_1^2 \quad . \qquad \text{(E7)}$$

Equation (E5) overspecifies this problem of determining the coefficient errors. These can be found by applying the methods of Appendix C. Alternatively one can note that Equation (E6) comes from a Taylor series expansion. It expresses the difference as an error times the parametric partial derivative of the measurements. Independence of the errors, Equation (E5) and considerable manipulation leads to

$$\frac{\alpha^2}{det} = \frac{\alpha_o^2}{|M_{oo}|} = \frac{\alpha_1^2}{|M_{11}|} = \cdots = \frac{\alpha_i^2}{|M_{ii}|} \qquad \text{(E8)}$$

where $|M_{ii}|$ is the minor corresponding to the cofactor m_{ii}, i.e., the determinant written without the i^{th} row and column. This is properly normalized for the sum of the products of each cofactor and its minor is

the determinant. In the linear example (E8) is simply

$$\frac{\alpha^2}{N[X^2]-[X]^2} = \frac{\alpha_0^2}{[X^2]} = \frac{\alpha_1^2}{N} \qquad \text{(E9)}$$

The alphas so defined are the standard errors of the parameters. The more commonly quoted probable error is .7854 times the standard error. The weights mentioned above are inversely proportional to the error squared.

Whenever several different cross sections are averaged, weights are assigned to each one. The average cross section becomes

$$\bar{Q} = [WQ]/[W]$$

$$\overline{\alpha} = \frac{[WQ^2]}{[W]} - \left\{\frac{[WQ]}{[W]}\right\}^2 \qquad \text{(E10)}$$

where w_i is the i^{th} weight. The average error, which is the quoted value, is given by the second of (E10).

σ_{01} is determined by substituting the averaged measure of σ_{10} into Equation (2.14). The error ($\delta\sigma_{01}$) is then given by

$$\frac{\delta\sigma_{01}}{\sigma_{01}} = \frac{\delta\sigma_{10}}{\sigma_{10}} + \frac{1}{1-F_\infty^\circ}\,\frac{\delta F_\infty^\circ}{F_\infty^\circ} \qquad \text{(E11)}$$

A variant of the fitting method is used in normalizing experimental points (M_i) to the theoretical values (T_i). This is a one parameter fit. The average difference between pairs of points will not

vanish. If weights are assigned, the normalization constant satisfies

$$C = \frac{[W\,T\,M]}{[W\,T\,T]} \qquad \text{(E12)}$$

from the original equation

$$\frac{\partial}{\partial C}\left[W(M-C\,T)^2\right] = 0 \qquad \text{(E13)}$$

The error is the standard deviation divided by the square root of the total weight. The C of Figure 5.22 is one of the normalization constants as calculated from Equation (E12).

BIBLIOGRAPHY

1. W. Bleakney, Phys. Rev. 35, 1180 (1930).
2. P. T. Smith, Phys. Rev. 36, 1293 (1930).
3. J. T. Tate and P. T. Smith, Phys. Rev. 39, 270 (1932).
4. W. Bleakney, Phys. Rev. 40, 496 (1932).
5. A. Dalgarno and H. N. Yadav, Proc. Phys. Soc. A66, 173 (1953).
6. H. S. W. Massey and E. H. S. Burhop, Electronic and Ionic Impact Phenomena, (Claredon Press, Oxford, 1952), Chapter 8.
7. W. R. Ott, W. E. Kauppila, and W. L. Fite, Phys. Rev. Letters 19, 1361 (1967).
8. J. B. Hasted, Advances in Electronics and Electronic Physics, (Academic Press, New York, 1960), Vol. XIII, pp. 1-81.
9. D. R. Bates and A. Dalgarno, Proc. Phys. Soc. A66, 972 (1953).
10. W. L. Fite, R. F. Stebbings, D. G. Hummer, and R. T. Brackmann, Phys. Rev. 119, 1939 (1960);
    Phys. Rev. 124, 2051 (1961).
11. W. L. Fite, A. C. H. Smith, and R. F. Stebbings, Proc. Roy. Soc. 268, A527 (1962).
12. S. Dushman and J. M. Lafferty, Scientific Foundations of Vacuum Technique, (John Wiley and Sons, New York, 1962), Table 10.1, p. 696.
13. A. H. Futch and C. C. Damm, Nucl. Fusion 3, 124 (1963).
14. N. V. Fedorenko, V. A. Ankudinov, and R. N. Il'in, Zh. T. F. 35, 595 (1965), [Sov. Phys. - Tech. Phys. 10, 461 (1965) - English translation].

15. C. C. Damm, J. H. Fotte, A. H. Futch, and R. F. Post, Phys. Rev. Letters 10, 323 (1963).

16. D. R. Sweetman, Nucl. Fusion, 1962 Suppl. Part 1, 279.

17. J. R. Hiskes, Nucl. Fusion 2, 38 (1962).

18. J. R. Hiskes, C. B. Tarter, and D. A. Moody, Phys. Rev. 133, A424 (1964).

19. D. S. Bailey, J. R. Hiskes, and A. C. Riviere, Nucl. Fusion 5, No. 1 (1965).

20. R. N. Il'in, B. I. Kikiani, V. A. Oparin, E. S. Solov'ev, and N. V. Federenko, Zh ETF 47, 1235 (1964), [JETP 20, 835 (1965) - English transl.].

21. R. N. Il'in, V. A. Oparin, E. S. Solov'ev, and N. V. Federenko, Zh TF 36, 1241 (1966), [Sov. Phys. - Tech. Phys. 11, 921 (1967) - English transl.].

22. H. Bolen, G. Clausnitzer, and H. Wilsch, Zeits. Phys. 208, 159 (1968).

23. B. L. Donnally and W. Sawyer, Phys. Rev. Letters 15, 439 (1965).

24. B. L. Donnally, T. Clapp, W. Sawyer, and M. Schultz, Phys. Rev. Letters 12, 502 (1964).

25. L. Madansky and G. Owen, Phys. Rev. Letters 2, 209 (1959).

26. L. Colli, F. Cristofori, G. Frigerio, and P. Sona, Phys. Letters 3, 62 (1962).

27. J. E. Bayfield, Phys. Rev. 182, 115 (1969).

28. J. E. Bayfield, Phys. Rev. Letters 20, 1223 (1968).

29. G. Ryding, A. B. Wittkower, and H. B. Gilbody, Proc. Phys. Soc. (London) 89, 547 (1966).

30. D. R. Bates and G. Griffing, Proc. Phys. Soc. (London) A66, 961 (1953).

31. D. Jaecks, B. Van Zyl, and R. Geballe, Phys. Rev. 137, A340 (1965).

32. W. L. Fite and R. T. Brackmann, Phys. Rev. 112, 1151 (1958).

33. G. H. Dunn, R. Geballe, and D. Pretzer, Phys. Rev. 128, 2200 (1962).

34. E. L. Chupp, L. W. Dotchin, and D. J. Pegg, Phys. Rev. 175, 44 (1968).

35. M. Gryzinski, Phys. Rev. 115, 374 (1959).

36. M. Gryzinski, Phys. Rev. 138, A305 (1965).

37. M. Gryzinski, Phys. Rev. 138, A322 (1965).

38. M. Gryzinski, Phys. Rev. 138, A336 (1965).

39. M. Gryzinski, Phys. Rev. Letters 14, 1059 (1965).

40. J. D. Garcia, E. Gerjuoy, and J. E. Welker, Phys. Rev. 165, 66 (1968).

41. P. A. Schmelzbach, W. Gruebler, V. Konig, and P. Marmier, Helv. Phys. Acta 41, 442 (1968).

42. A. S. Schlachter, P. J. Bjorkholm, D. H. Loyd, L. W. Anderson, and W. Haeberli, Phys. Rev. 177, 184 (1969).

43. A Cesati, F. Cristofori, L. M. Colli, and P. Sona, Energia Nucleare 13, 649 (1966).

44. I. A. Sellin, Phys. Rev. 136, A1245 (1964).

45. I. A. Sellin and L. Granoff, Phys. Letters 25A, 484 (1967).

46. G. Spiess, A. Valance, and P. Pradel, Abst. 7th Int. Conf. on Physics of Electronic and Atomic Collisions, Amsterdam, 1971 (North-Holland Publ. Co., Amsterdam, 1971), pp. 823 - 824.

47. J. R. Oppenheimer, Phys. Rev. 31, 349 (1928).

48. H. C. Brinkman and H. A. Kramers, Proc. Acad. Soc. (Amsterdam) 33, 973 (1930).

49. D. R. Bates and A. Dalgarno, Proc. Phys. Soc. (London) A65, 919 (1952).

50. F. Ribe, Phys. Rev. 83, 1217 (1951).

51. J. D. Jackson and H. Schiff, Phys. Rev. 89, 359 (1953).

52. J. R. Hiskes, Phys. Rev. A137, 361 (1965).

53. S. T. Butler and I. D. S. Johnston, Phys. Letters 9, 141 (1964).

54. S. T. Butler, R. M. May, and I. D. S. Johnston, Phys. Letters 10, 281 (1964).

55. S. T. Bulter and I. D. S. Johnston, Nucl. Fusion 4, 196 (1964).

56. R. M. May, Nucl. Fusion 4, 207 (1964).

57. H. A. Bethe and E. E. Salpeter, Encyclopedia of Physics (Springer-Verlag, Berlin, 1957), Vol. XXXV, p. 370.

58. G. Breit and E. Teller, Astrophys. J. 91, 215 (1940).

59. J. Shapiro and G. Breit, Phys. Rev. 113, 179 (1959).

60. W. L. Wiese, M. W. Smith, and B. M. Glennon, Atomic Transition Probabilities, NBS Circ. 4 (U. S. Govt. Printing Office, Washington, 1966), Vol. I.

61. Obtained from Radiation Dynamics, Inc., Westbury Industrial Park, Westbury, Long Island.

62. The mixture is RCA No. 33C-118 available from the Harrison, New Jersey plant of RCA.

63. R. T. Brackmann, W. L. Fite, and K. E. Hagen, Rev. Sci. Inst. 29, 125 (1958).

64. P. H. Metzger and G. R. Cook, J. Quant. Spectrosc. Radiat. Transfer 4, 107 (1964).

65. Obtained from Harshaw Chemical Co., 1945 E. 97th Street, Cleveland 6, Ohio.

66. W. M. Preston, Phys. Rev. 57, 887 (1940).

67. Y. Tanaka, E. C. Y. Inn, and K. Watanabe, J. Chem. Phys. 21, 1651 (1953).

68. W. E. Kauppila, W. R. Ott, and W. L. Fite, Rev. Sci. Inst. 38, 811 (1967).

69. W. R. Ott, "Polarization of Lyman Alpha Radiation Emitted in Electron-Hydrogen Atom Collisions and Emitted by Metastable H(2S) Atoms in Weak Electric Fields", Ph.D. Thesis, University of Pittsburgh, 1968 (unpublished).

70. See for example: H. B. Callen, Thermodynamics (John Wiley and Sons, New York, 1963), Chapt. 17.

71. E. G. Schneider, Phys. Rev. 49, 341 (1936).

72. K. Watanabe, E. Inn, and M. Zelikoff, J. Chem. Phys. 20, 1969 (1952).

73. R. W. Ditchburn, J. E. S. Bradley, C. G. Cannon, and G. Munday, Rocket Exploration of the Upper Atmosphere (Pergamon Press, London, 1954), R. L. F. Boyd and M. J. Seaton, editors, pp. 327 - 334.

74. P. Lee, J. Opt. Soc. Amer. 45, 703 (1955).

75. K. Watanabe, Advances in Geophysics (Academic Press, New York, 1958), H. E. Landsberg and J. Van Mieghem, ed., Vol. 5, pp. 151 - 221.

76. See for example: A. G. Pacholczyk, Radio Astrophysics (W. H. Freeman, San Francisco, 1970), Chapt. 5.

77. D. Pretzer, B. Van Zyl, and R. Geballe, Phys. Rev. Letters 10, 340 (1963).

78. L. Harris and J. K. Beasley, J. Opt. Soc. Amer. 42, 134 (1952).

79. V. V. Gritsyna, T. S. Kijan, A. G. Koval', and Ja. M. Fogel', Phys. Letters 27A, 292 (1968).

80. A. A. Sterk, C. L. Marks, and W. P. Saylor, Phys. Rev. Letters 17, 1037 (1966).

81. R. Nieman, T. M. Donahue, and K. Lulla, Bull. Am. Phys. Soc. 12, 114 (1967); R. A. Nieman and T. M. Donahue, Bull. Am. Phys. Soc. 13, 66 (1968);
R. Nieman, K. Lulla and T. M. Donahue, Abst. 5th Int. Conf. on Phys. Electronic and Atomic Collisions, Leningrad, 1967 (Nauka, Leningrad, 1967), pp. 18-19.

82. A. V. Vinogradov, L. P. Presnyakov, and V. P. Shevel'ko, Zh ETF Pis. Red. 8, 449 (1968), [JETP Letters 8, 275 (1968) - English transl.]

83. J. A. Bearden and A. F. Burr, Rev. Mod. Phys. 39, 125 (1967).

84. E. Gerjuoy, Phys. Rev. 148, 54 (1966).

85. S. K. Allison, Rev. Mod. Phys. 30, 1137 (1958).

86. G. W. McClure, Phys. Rev. 130, 1852 (1963).

87. B. Van Zyl, D. Jaecks, D. Pretzer, and R. Geballe, Phys. Rev. 158, 29 (1967).

88. J. D. Jackson, Classical Electrodynamics (John Wiley and Sons, New York, 1962), p. 380.

89. E. M. Purcell, Astrophys. J. 116, 457 (1952).

90. M. J. Seaton, Proc. Phys. Soc. (London) A68, 457 (1954).

91. L. R. Wilcox and W. E. Lamb, Jr., Phys. Rev. 119, 1915 (1960).

92. J. I. Gersten, J. Chem. Phys. 51, 637 (1969).

93. M. Bloom, I. Oppenheim, M. Lipsicas, C. G. Wade, and C. F. Yarnell, J. Chem. Phys. 43, 1036 (1965).

94. A. L. McClellan, Tables of Experimental Dipole Moments (W. H. Freeman, San Francisco, 1963).

95. V. Dose, V. Meyer, and M. Salzmann, J. Phys. B. (Atom. Molec. Phys.) 2, 1357 (1969).

96. H. B. Gilbody, R. Browning, R. M. Reynolds, and G. I. Riddell, Abst. 7th Int. Conf. on Phys. Electronic and Atomic Collisions, Amsterdam, 1971 (North-Holland Publ. Co., Amsterdam, 1971), pp. 1080 - 1082.

97. G. Spiess, A. Valance, and P. Pradel, Abst. 7th Int. Conf. on Phys. Electron. Atom. Coll., Amsterdam, 1971 (North-Holland, Amsterdam, 1971), pp. 1083 - 1084.

98. D. R. Bates and J. C. G. Walker, Planet. Space. Sci. 14, 1367 (1966).

99. G. Herzberg, Atomic Spectra and Atomic Structure (Dover Publications, New York, 1944), Chapter 2.

100. J. A. Phillips and J. L. Tuck, Rev. Sci. Inst. 27, 97 (1956).

101. See for example: R. K. Eisenschitz, Matrix Algebra for Physicists (Plenum Press, New York, 1966).

102. E. U. Condon and G. H. Shortley, The Theory of Atomic Spectra (Cambridge Univ. Press, Cambridge, 1963).

103. L. Green, P. Rush, and C. Chandler, Astrophy. J. Suppl. Ser. 3, 37 (1957).

104. J. D. Jackson, Classical Electrodynamics (John Wiley, New York, 1962), pp. 502, 558.

105. H. A. Bethe and E. E. Salpeter, Quantum Mechanics of One- and Two-Electron Atoms (Springer-Verlag, Berlin, 1957).

106. G. Lüders, Z. Naturforsch. 5a, 608 (1950).

107. V. Zhukovskii, M. Kolesnikova, A. Sokolov, and I. Khermann, Optika i Spekt. 28, 622 (1969), [Opt. and Spectroc. 28, 337 (1970) - English transl.].

108. W. E. Lamb and R. C. Rutherford, Phys. Rev. 79, 549 (1950).

109. See for example: L. I. Schiff, Quantum Mechanics (McGraw-Hill Book Co., New York, 1955), Chapter 7.

110. See for example: S. Perlis, Theory of Matrices (Addison-Wesley Press, Cambridge, Mass., 1952).

111. See for example: E. M. Pugh and E. W. Pugh, Principles of Electricity and Magnetism (Addison-Wesley Publ. Co., Reading, Mass., 1960), pp. 116 - 122.

112. E. R. Cohen and J. W. M. DuMond, Encyclopedia of Physics (Springer-Verlag, Berlin, 1957), Vol. XXXV, pp. 1 - 87.

113. See for example: J. Topping, Errors of Observation and Their Treatment (Reinhold Publishing Co., New York, 1958), Chapters 2 and 3.

114. Handbook of Chemistry and Physics, 44th Edition, Chem. Rubber Publishing Co., 1961, pp. 3513-3514.

115. Handbook of Chemistry and Physics, 44th Edition, Chem. Rubber Publishing Co., 1961, pp. 2416-2417.

116. E. J. Stone (private communication).

117. C. E. Moore, NBS Circ. 467, U. S. Govt. Printing Office, Vol. I (1950), II (1952), III (1958).

LIST OF TABLES

TABLE 1.1.

A Short Guide to Cross Sections

Alkali	TX	MX	F°∞
Lithium	21		
Sodium	21		21
Potassium	21,41	45	21,41
Rubidium		45	
Cesium	21,42,46	24,43,45,46	21,42

TABLE 2.1.

Maximum Gryzinski Cross Sections

Alkali	$r_a[\mathring{A}]$[114]	$Q_{max}[\mathring{A}^2]$ (Eqn. 2.27)	E_p[keV] (± 0.1)	$Q_{max}[\mathring{A}^2]$ (Eqn. 2.30)
Lithium	1.52	55.2	1.4	20.6
Sodium	1.86	68.2	1.4	24.3
Potassium	2.27	98.2	1.0	45.7
Rubidium	2.48	110.2	0.8	53.6
Cesium	2.65	126.8	0.6	74.4

TABLE 3.1.

Standard Points for the Thermocouple Calibration[115]

Standard Point	T[°C]
LN_2	-195.80
CO_2	- 78.51
Ice	0.00
Steam	100.0
Tin	231.85

TABLE 3.2.

Molecular Oxygen UV Windows

	(Ref. 64)		(Ref. 116)	
	$\lambda[cm^{-1}]$	$k[cm^{-1}]$		Source
1	1215.7	0.28	HI	Lyα
2	1187.1	0.20	H_2	1188.0 W(3,6)R1*
3	1166.8	0.29	H_2	1166.1 W(1,4)P3
4	1157.0	0.44	H_2	1157.0 W(0,3)P5
5	1142.8	0.31	H_2	1141.9 W(5,6)P2‡
6	1126.9	0.62	H_2	1126.2 W(4,5)Q3
7	1108.3	0.20	H_2	1108.2 W(3,4)Q2

*Hydrogen Werner band (weaker Lyman band ignored)

‡Calculated value (probably ~ 0.3Å high) - not observed as yet.

TABLE 4.1.

Alkali Density Constants

ALKALI	A[$cm^{-3}T$]	B[T]
Lithium	9.417 (26)	18,560
Sodium	5.352 (26)	12,646
Potassium	1.900 (26)	10,302
Rubidium	1.438 (26)	9,466.9
Cesium	8.304 (25)	8,760.7

TABLE 5.1.

Summary of p + K Results

ENERGY [keV]	$\sigma_{10}[10^{-16}\ cm^2]$	$\delta[10^{-4}]$	F^{0}_{∞}
4	43.9 ± 5.7	326 ± 86	
5	55.9 ± 5.8	426 ± 89	.956
6	43.3 ± 2.1	242 ± 44	.947
7	36.8 ± 4.9	292 ± 28	.962
8	26.4 ± 1.3	288 ± 34	.938
9	22.3 ± 1.4	247 ± 20	
10	23.3 ± 1.4	290 ± 80	.860
11	23.4 ± 1.1	291 ± 30	
12	11.1 ± 0.8	280 ± 15	.700
13	25.2 ± 2.0	218 ± 41	
14	12.5 ± 2.8	234 ± 17	.577
15	12.9 ± 1.8	373 ± 39	
16	7.71 ± 0.54	199 ± 10	.559
17	6.39 ± 0.11	296 ± 23	
18	5.11 ± 0.38	172 ± 23	.499
19	4.45 ± 0.72	260 ± 56	
20	5.12 ± 0.43	193 ± 18	.412
22	3.42 ± 0.49	170 ± 82	
24	2.81 ± 0.65	197 ± 10	.406
26	2.62 ± 0.21	156 ± 16	
28	1.98 ± 0.20	206 ± 63	.342
30	1.93 ± 0.10	161 ± 40	

TABLE 5.2.

Summary of p + Na Results

ENERGY [keV]	$\sigma_{10}[10^{-16}\ cm^2]$	$\delta[10^{-4}]$	F^{0}_{∞}
6	32.2 ± 2.2	556 ± 34	
8	27.1 ± 2.1	465 ± 28	
10	20.1 ± 1.8	550 ± 36	
12	12.0 ± 1.7	426 ± 25	
14	8.48 ± 0.42	355 ± 19	.600
16	4.89 ± 0.10	465 ± 10	.570
18	4.12 ± 0.10	357 ± 15	.394
20	2.70 ± 0.10	324 ± 24	.460
22	2.62 ± 0.27	269 ± 55	.380
24	1.61 ± 0.20	300 ± 28	
26	1.98 ± 0.20	359 ± 50	
28	2.20 ± 0.23	272 ± 124	
30	1.41 ± 0.30	259 ± 120	

TABLE 5.3.

Summary of H_2^+ Results

ENERGY	σ_{10}(K)[10^{-16} cm^2]	σ_{10}(Na)[10^{-16} cm^2]	Δ[10^{-4}]
10	55.0 ± 6.6		59 ± 106
13	41.9 ± 6.3		14 ± 106
14			442 ± 131
16	60.8 ± 2.34		
18			249
19	39.3 ± 7.7		291 ± 142
20		10.82 ± 0.76	
22	32.5 ± 7.7	10.24 ± 0.17	
25		5.23 ± 0.16	354 ± 16
27		6.63 ± 0.73	144 ± 45
30		4.84 ± 0.22	220 ± 16

TABLE 5.4.

Alkali Binding Energies

Z	ELEMENT	Valence Electron [117] Configuration	Valence Electron [117] Binding Energy	Inner Shell [83] Configuration	Inner Shell [83] Binding Energy
3.	Lithium	$2S_{\frac{1}{2}}$	5.390	$(1s)^2$	54.75 ± 0.02
11	Sodium	$3S_{\frac{1}{2}}$	5.138	$(2p)^6$	31.1 ± 0.4
19	Potassium	$4S_{\frac{1}{2}}$	4.339	$(3s)^2$	33.9 ± 0.4
				$(3p)^6$	17.8 ± 0.4
37	Rubidium	$5S_{\frac{1}{2}}$	4.176	$(4s)^2$	29.3 ± 0.4
				$(4p)^6$	14.8 ± 0.4 14.0 ± 0.3
55	Cesium	$6S_{\frac{1}{2}}$	3.893	$(5s)^2$	22.7 ± 0.5
				$(5p)^6$	13.1 ± 0.5 11.4 ± 0.5

TABLE 5.5.

Best Values for the Background H_2 Values or

π and n as Deduced from Measured δ Values

PROBE	TARGET		
	K	Na	K + Na
P [π]	6.80 ± 6.15(13)	11.0 ± 8.5 (13)	7.76 ± 6.88 (13)
[n]	2.43 ± 2.20(12)	3.84 ± 3.04(12)	2.78 ± 2.46 (12)
H_2^+ [π]			8.50 ± 71.10(13)
[n]			3.04 ± 25.40(12)

TABLE 5.6.

Purcell Alkali Quenching Cross Sections

E(keV)	σ'	σ''	$\bar{\sigma}_{total}$
5	1.39 (-13)	2.30 (-13)	3.69 (-13)
10	7.30 (-14)	1.22 (-13)	1.95 (-13)
15	5.01 (-14)	8.44 (-14)	1.34 (-13)
20	3.83 (-14)	6.48 (-14)	1.03 (-13)
25	3.11 (-14)	5.28 (-14)	8.39 (-14)
30	2.63 (-14)	4.46 (-14)	7.09 (-14)
50	1.63 (-14)	2.79 (-14)	4.42 (-14)

TABLE 5.7.

Purcell-Seaton Proton Swarm Quenching Transition Rates

T(°K)	W'/N_p	W''/N_p
1,500	4.36 (-4)	1.46 (-4)
2,000	4.18 (-4)	2.07 (-4)
2,500	4.02 (-4)	2.41 (-4)
3,000	3.88 (-4)	2.62 (-4)
5,000	3.46 (-4)	2.94 (-4)
10,000	2.88 (-4)	2.95 (-4)
15,000	2.56 (-4)	2.82 (-4)
20,000	2.34 (-4)	2.70 (-4)
25,000	2.18 (-4)	2.59 (-4)

TABLE 5.8.

Gersten Molecular Quenching Cross Sections

E_p	$\sigma_2(N_2)$	$\sigma_2(O_2)$	$\sigma_2(H_2)$	$\sigma_1(N_2O)$	$\sigma_2(CO_2)$
0.3 eV	1.80 (-14)	1.20 (-14)	9.01 (-15)	1.90 (-13)	3.63 (-14)
1.0 eV	1.21 (-14)	8.02 (-15)	6.03 (-15)	1.04 (-13)	2.43 (-14)
0.5 keV	1.52 (-15)	1.01 (-15)	7.60 (-16)	4.65 (-15)	3.06 (-15)
1.0	1.21 (-15)	8.02 (-16)	6.03 (-16)	3.29 (-15)	2.43 (-15)
5.0	7.06 (-16)	4.69 (-16)	3.53 (-16)	1.47 (-15)	1.42 (-15)
10.0	5.61 (-16)	3.72 (-16)	2.80 (-16)	1.04 (-15)	1.13 (-15)
15.0	4.90 (-16)	3.25 (-16)	2.45 (-16)	8.49 (-16)	9.85 (-16)
20.0	4.45 (-16)	2.95 (-16)	2.22 (-16)	7.35 (-16)	8.95 (-16)
25.0	4.13 (-16)	2.74 (-16)	2.06 (-16)	6.58 (-16)	8.30 (-16)
30.0	3.89 (-16)	2.58 (-16)	1.94 (-16)	6.00 (-16)	7.82 (-16)
50.0	3.28 (-16)	2.18 (-16)	1.64 (-16)	4.65 (-16)	6.59 (-16)

TABLE B1

Condon and Shortley[102] Corrections

In Table 4^5:

4s7p reads 5.7, should be 4.2

4p7d reads 7.7, should be 6.7

In Table 5^5:

6s5p reads 1.7(-3), should be 2.7(-3)

6p5s reads 2.1(-3), should be 2.4(-3)

6d2p reads .048 , should be .051

In Table 6^5:

n = 3 reads 1.02, should be 1.002

n = 4 reads 3.35, should be 3.32

n = 5 reads 8.8 , should be 8.66

n = 6 reads 19.6, should be 19.27

TABLE 32

Hydrogen Transition Probabilities and Lifetimes

n	$\bar{A}_{NBS4}$ [60]	$\bar{A}_{TW}$	τ_{CS} [102]	τ_{TW}	τ_{M} [56]	τ_{J} [104]	τ_{RS} [105]
2	4.699 (8)	4.694 (8)	2.1	2.130	1.1	3.0	8.5
3	9.985 (7)	9.975 (7)	10.2	10.02	3.5	23	53
4	3.019 (7)	3.016 (7)	33.5	33.15	8.7	96	192
5	1.156 (7)	1.155 (7)	88	86.61	18	294	525
6	5.191 (6)	5.189 (6)	196	192.7	34	731	1193
7	2.617 (6)	2.612 (6)		382.9	.055μs	1.6μs	2.4μs
8	1.438 (6)	1.436 (6)		696.2	.088μs	3.1μs	4.4μs
9	8.450 (5)	8.462 (5)		1182	.14μs	5.5μs	7.4μs
10	5.236 (5)	5.214 (5)		1918	.20μs	9.4μs	12 μs
11	3.391 (5)	3.380 (5)		2959	.29μs	15 μs	18 μs
12	2.277 (5)	2.284 (5)		4378	.39μs	23 μs	27 μs

Lifetimes are given in nsec unless otherwise noted.

Transition probabilities are given in sec^{-1}.

TW means this work.

FIGURE CAPTIONS

Figure 2-1. Bates and Dalgarno cross section for charge exchange between protons and potassium.

Figure 2-2. Bates and Dalgarno cross section for charge exchange between protons and sodium.

Figure 2-3. May calculation of the angular momentum state of atomic hydrogen produced during p + H collisions.

Figure 2-4. Contributions to $_{10}Q_{01}$ for p + K from various atomic hydrogen levels.

Figure 2-5. Gryzinski calculation of $_{10}Q_{01}$ for various alkali targets.

Figure 2-6. Same but for $_{10}Q_{01}(2S)$ assuming $N(2S)/N(2P) = 1/3$.

Figure 2-7. Predicted ratio of MX:TX assuming statistical weight population of states as a function of proton energy.

Figure 2-8. Metastable populations of the n = 2 states.

Figure 2-9. Same but assuming only S state captures.

Figure 2-10. Relative 2S population as a function of beam energy.

Figure 3-1. Schematic view of apparatus.

Figure 3-2. The neutral beam detector.

Figure 3-3. Schematic view of detection chamber and counter electronics.

Figure 3-4. Schematic view of electron gun.

Figure 3-5. Molecular oxygen window near 1216Å.

Figure 3-6. Relative transmission of oxygen filter for Lyman alpha for x = 2 atm-cm.

Figure 3-7. Integrated transmission of the oxygen filter as a function of the viewing angle θ_o.

Figure Captions Continued

Figure 4-1. Sample neutral fraction data.

Figure 4-2. Sample metastable hydrogen data.

Figure 5-1. σ_{10} for $p + K \rightarrow H^* + K^+$ with normalized $_{10}Q_{01}$ (norm. to 30 keV).

Figure 5-2. σ_{10} for $p + Na \rightarrow H^* + Na^+$ with normalized $_{10}Q_{01}$.

Figure 5-3. σ_{10} for H_2^+ on Na and K.

Figure 5-4. $F^{o}{}_{\infty}$ for p + K with error bars indicating the data spread.

Figure 5-5. $F^{o}{}_{\infty}$ for p + Na.

Figure 5-6. $F^{o}{}_{\infty}$ for $H_2^+ + K$ and $H_2^+ + Na$.

Figure 5-7 σ_{01} for potassium as deduced from measured values of σ_{10} and $F^{o}{}_{\infty}$ for p + K.

Figure 5-8. σ_{01} for sodium as above.

Figure 5-9. Theoretical values for $_{10}Q_{01}/_{10}Q_{01} + {}_{01}Q_{10}(m,n)$ for p + K showing experimental values of $F^{o}{}_{\infty}$.

Figure 5-10. Same but for p + Na.

Figure 5-11. $_{10}Q_{01}$ for inner shell excitation of various alkalis.

Figure 5-12. $_{10}Q_{01}$ for various alkalis including both valence shell and inner shell captures.

Figure 5-13. $_{10}Q_{01}(2S)$ for inner shell excitation of various alkalis.

Figure 5-14. $_{10}Q_{01}(2S)$ for the alkalis including both valence shell and inner shell captures.

Figure 5-15. Measured background neutral fraction (δ) for a potassium target with the normalized results of Allison superimposed.

Figure 5-16. Measured background neutral fraction for a sodium target as above.

Figure Captions Continued

Figure 5-17. Typical low density results for 16 keV protons on sodium - slight curvature of the "metastable" signal.

Figure 5-18. Same as above but for 20 keV protons - pronounced curvature of "metastable" signal.

Figure 5-19. $_{10}Q_{01}$ for protons on excited sodium and potassium assuming only valence electron contribution.

Figure 5-20. $\sigma_{10}(2S)$ values of Sellin and Granoff for p + Cs, p + Rb and p + K with normalized Gryzinski calculation $_{10}Q_{01}(2S)$.

Figure 5-21. $\sigma_{10}(2S)$ values of Donnally (Ref. 24) for $\bar{p}$ + Cs with normalized $_{10}Q_{01}(2S)$ calculation.

Figure 5-22. σ_{10} for p + Cs [Schlachter] and normalized $_{10}Q_{01}$.

Figure A-1. Beam charge states and the associated cross sections.

Figure C-1. Splitting of the first excited state of hydrogen as a function of external field.

Figure C-2. Behavior of 2S state as a function of applied field.

Figure C-3. Mixing coefficients of the two level approximation.

Figure C-4. Mixing coefficients of the three state approximation.

Figure C-5. Transition probability of the metastable 2S state as a function of electric field strength.

Figure C-6. Same as above but for the 2P states.

Figure D-1. Equipotentials of the dipole wires assuming a separation of 1.25 cm and a potential difference of 600 V.

Figure D-2. Equifields for the same configuration.

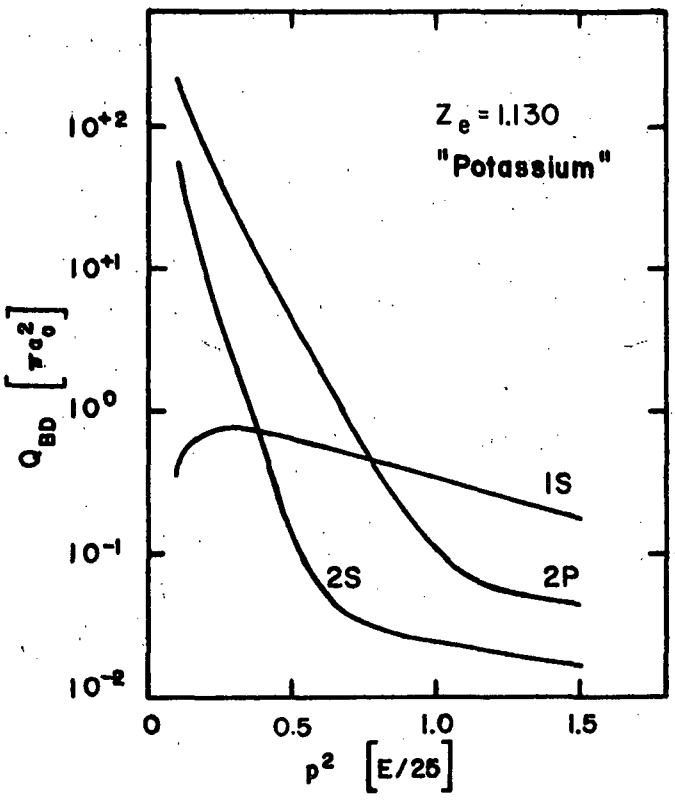
$Z_e = 1.130$
"Potassium"
10^{+2}
10^{+1}
10^{0}
10^{-1}
10^{-2}
Q_{BD} $[\pi a_o^2]$
1S
2S
2P
0
0.5
1.0
1.5
p^2 $[E/2S]$

Figure 2-1.

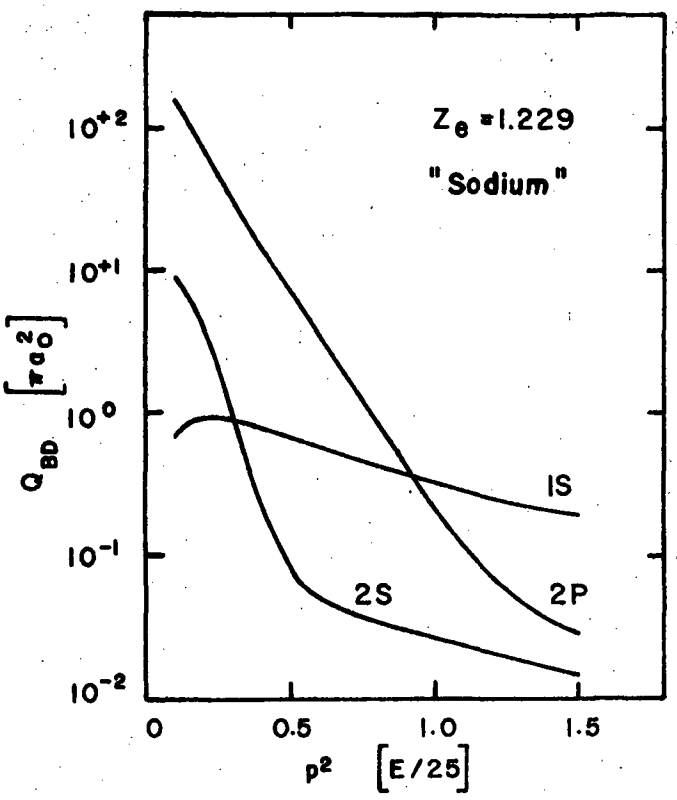
Z_e =1.229
"Sodium"
10^{+2}
10^{+1}
10^{0}
10^{-1}
10^{-2}
Q_{BD} $[\pi a_o^2]$
1S
2S
2P
0
0.5
1.0
1.5
p^2 [E/25]

Figure 2-2.

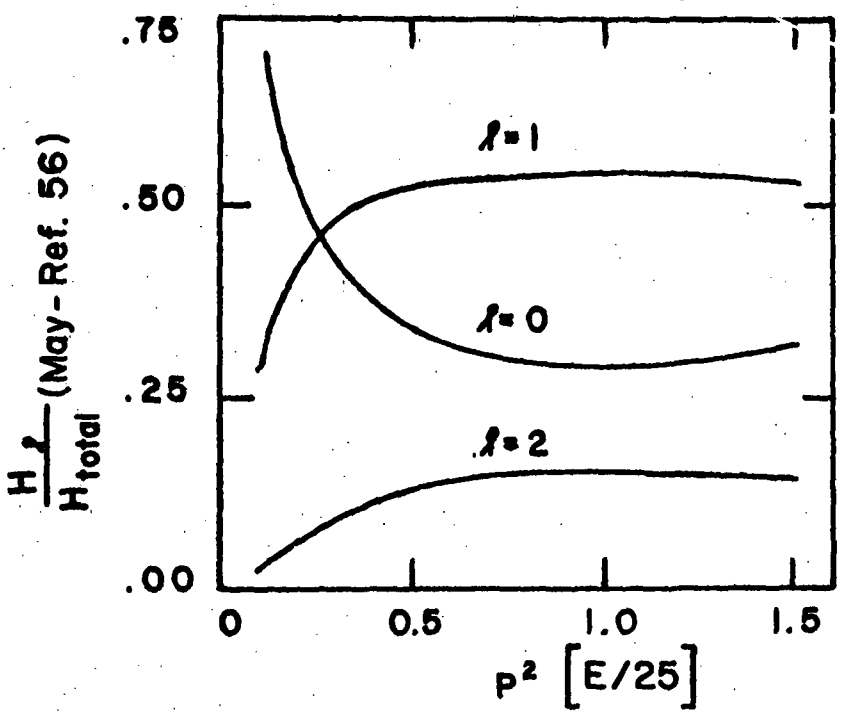

Figure 2-3.

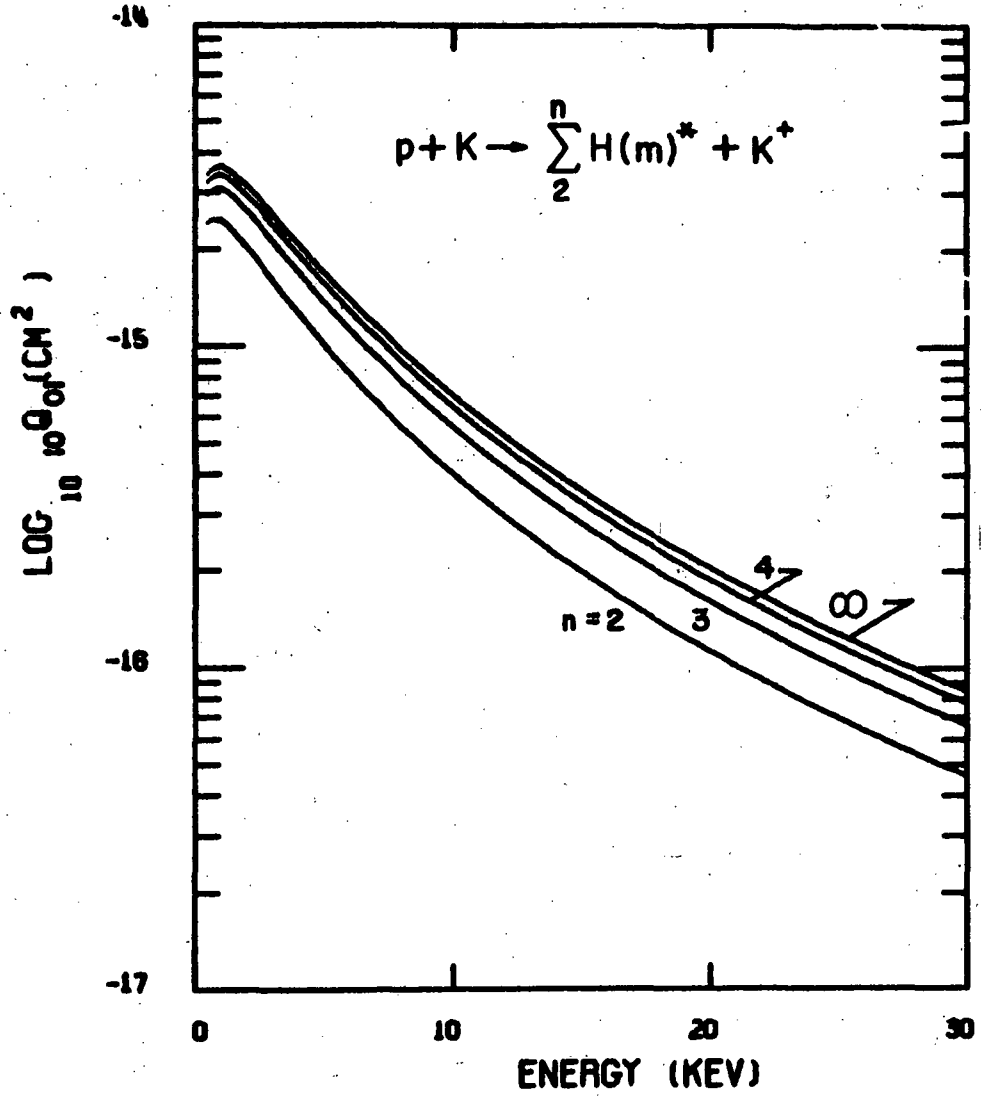
$p+K \rightarrow \sum_{2}^{n} H(m)^{*} + K^{+}$
$LOG_{10} Q_{CF} (CM^2)$
-14
-15
-16
-17
0
10
20
30
ENERGY (KEV)
n=2
3
4
∞

Figure 2-4.

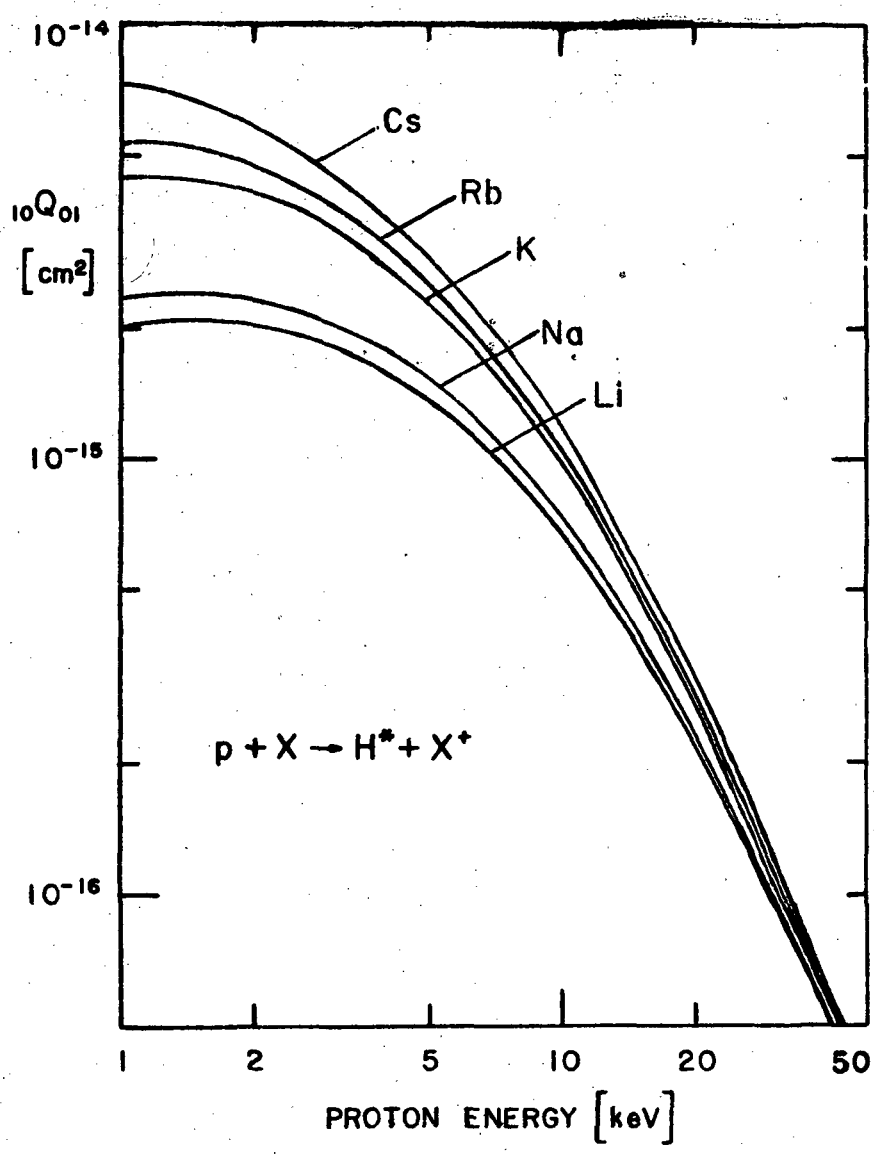
10^{-14}
$_{10}Q_{01}$
[cm²]
10^{-15}
10^{-16}
Cs
Rb
K
Na
Li
p + X → H* + X+
1
2
5
10
20
50
PROTON ENERGY [keV]

Figure 2-5.

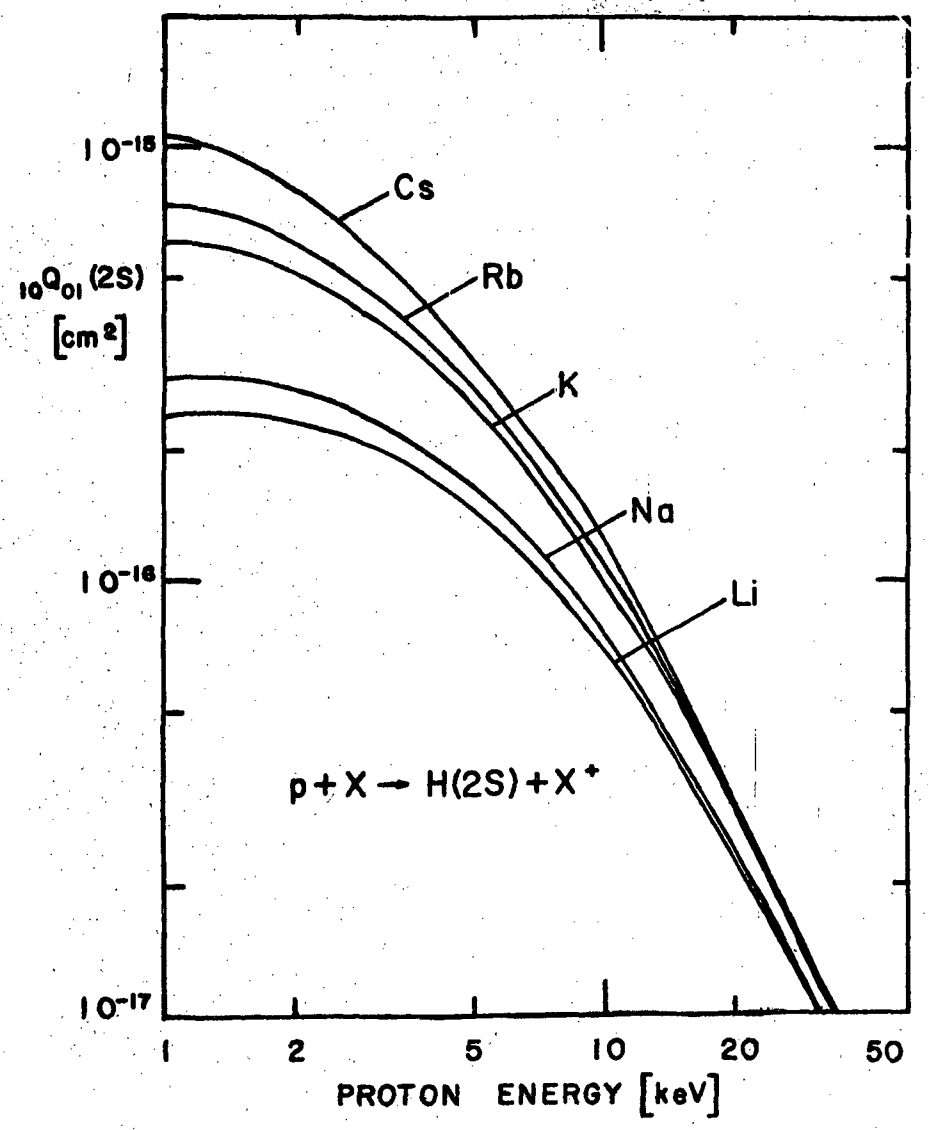
10^{-15}
10^{-16}
10^{-17}
$_{10}Q_{01}(2S)$
[cm²]
Cs
Rb
K
Na
Li
p+X → H(2S)+X⁺
1
2
5
10
20
50
PROTON ENERGY [keV]

Figure 2-6.

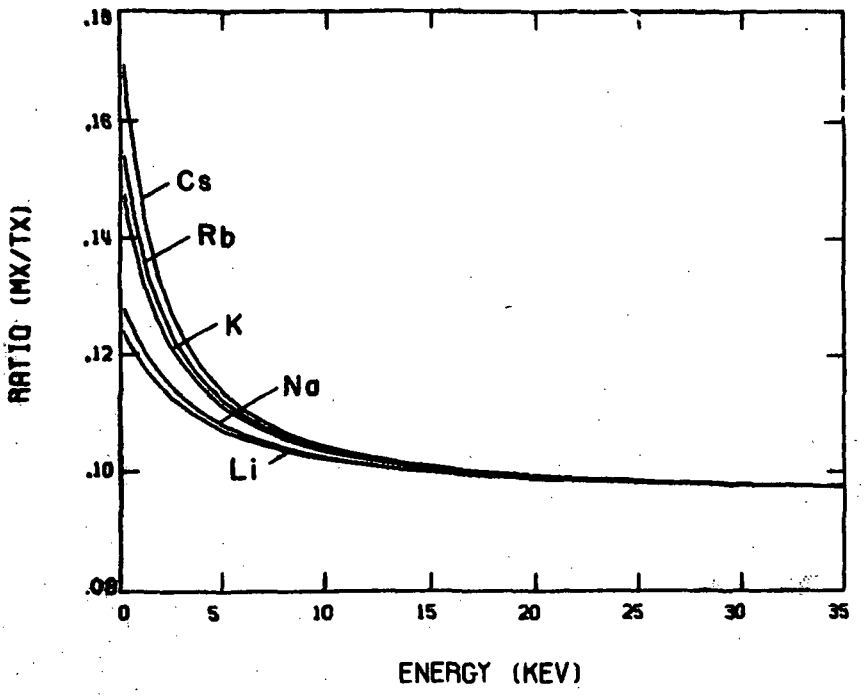
.18
.16
.14
.12
.10
.08
RATIO (MX/TX)
Cs
Rb
K
Na
Li
0
5
10
15
20
25
30
35
ENERGY (KEV)

Figure 2-7.

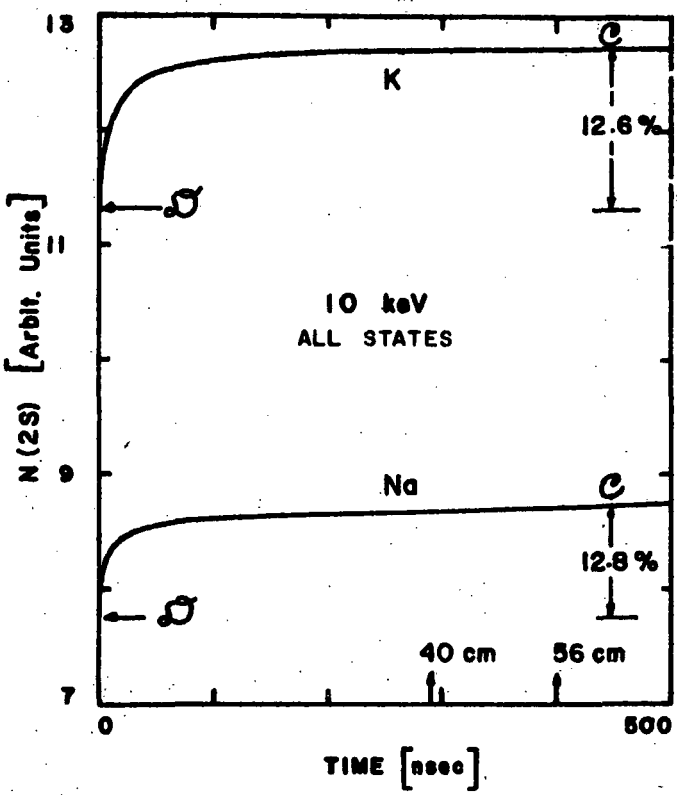
13
11
9
7
N(2S) [Arbit. Units]
K
12.6 %
10 keV
ALL STATES
Na
12.8 %
40 cm
56 cm
0
500
TIME [nsec]

Figure 2-8.

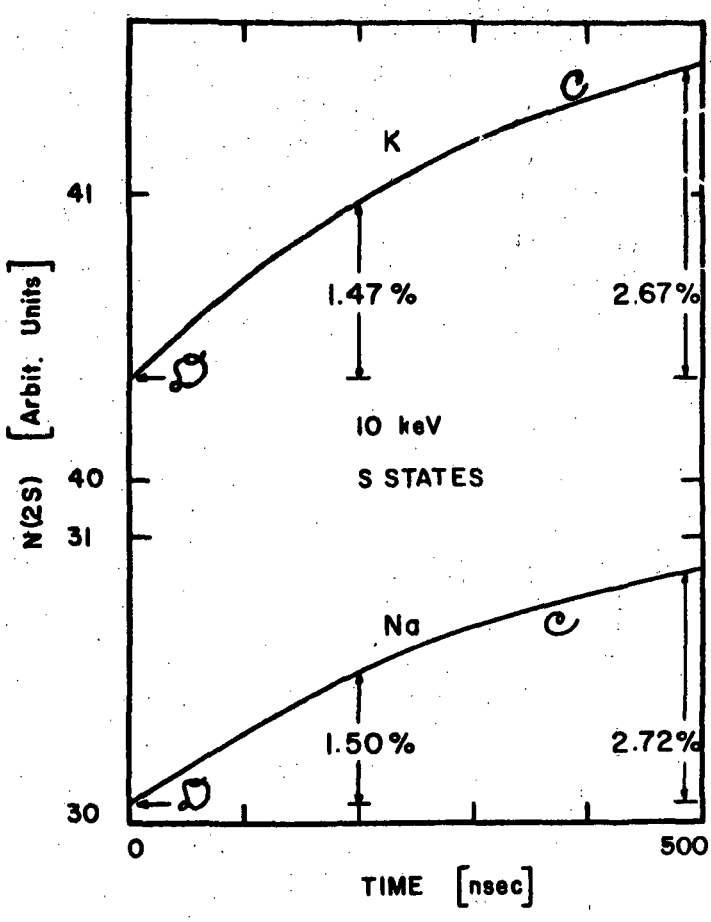
K
41
1.47 %
2.67%
10 keV
S STATES
N(2S) [Arbit. Units]
40
31
Na
1.50 %
2.72%
30
0
500
TIME [nsec]

Figure 2-9.

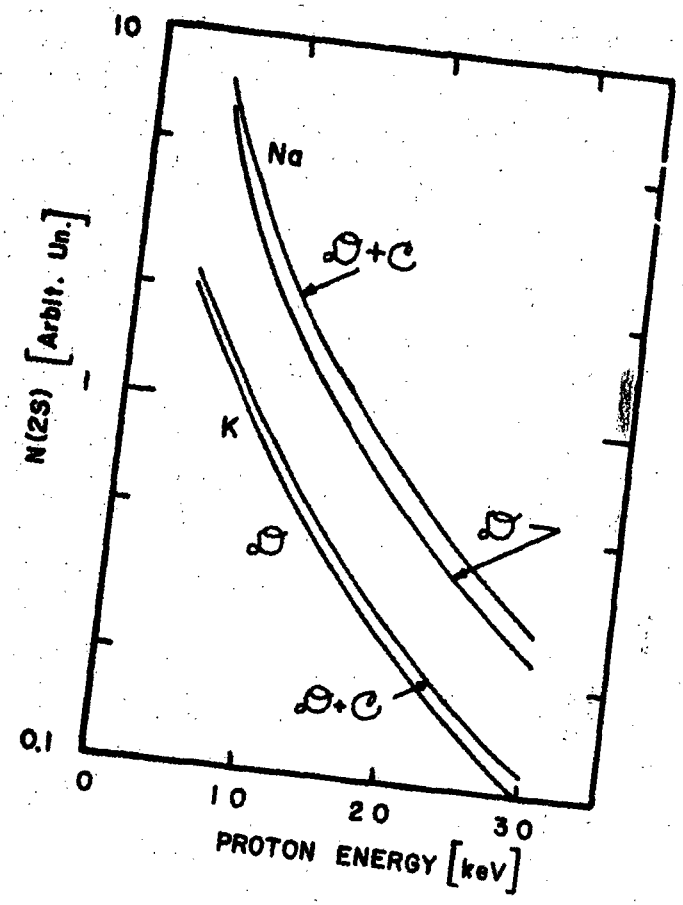

Figure 2-10.

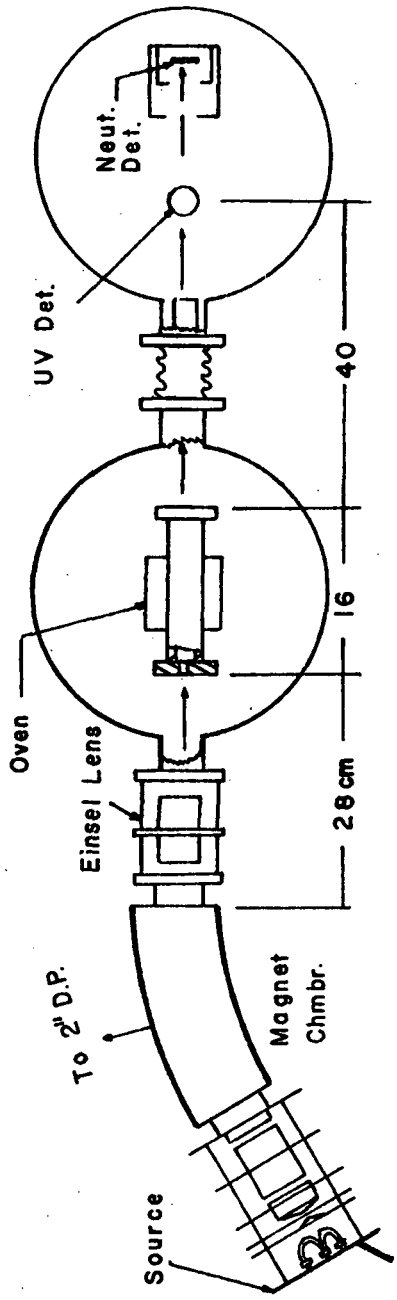
Neut.
Det.
UV Det.
40
16
Oven
Einsel Lens
28 cm
To 2" D.P.
Magnet
Chmbr.
Source

Figure 3-1.

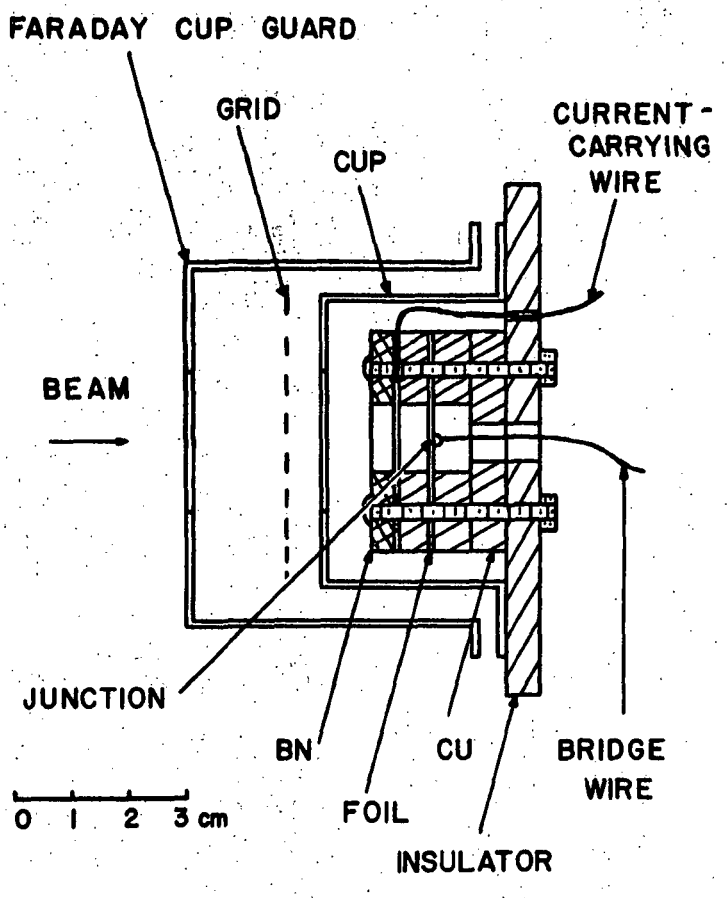
FARADAY CUP GUARD
GRID
CUP
CURRENT-CARRYING WIRE
BEAM
JUNCTION
BN
CU
BRIDGE WIRE
FOIL
INSULATOR
0 1 2 3 cm

Figure 3-2.

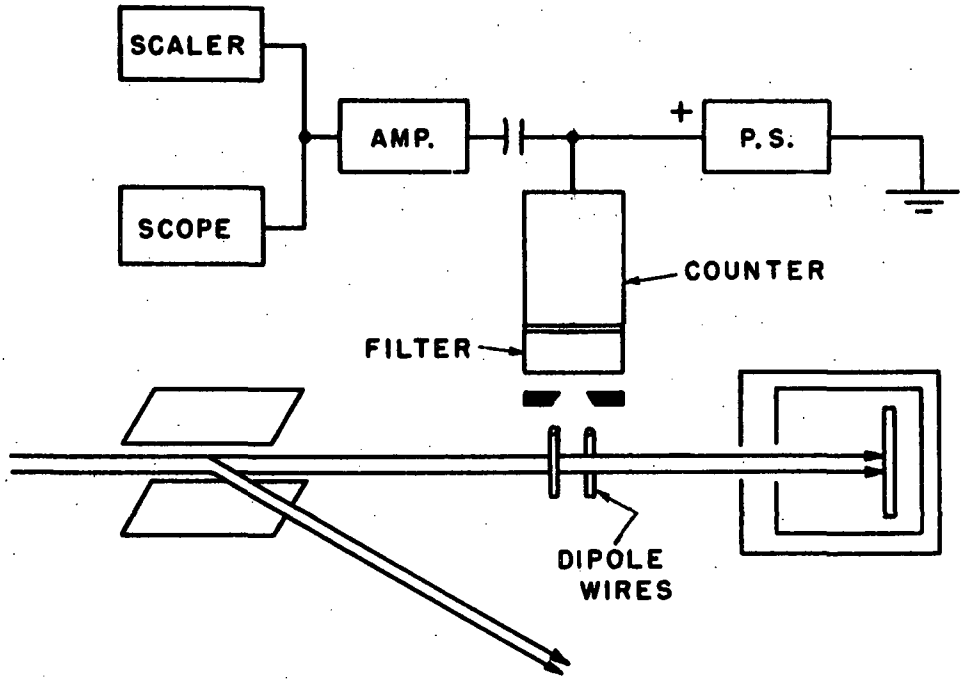

Figure 3-3.

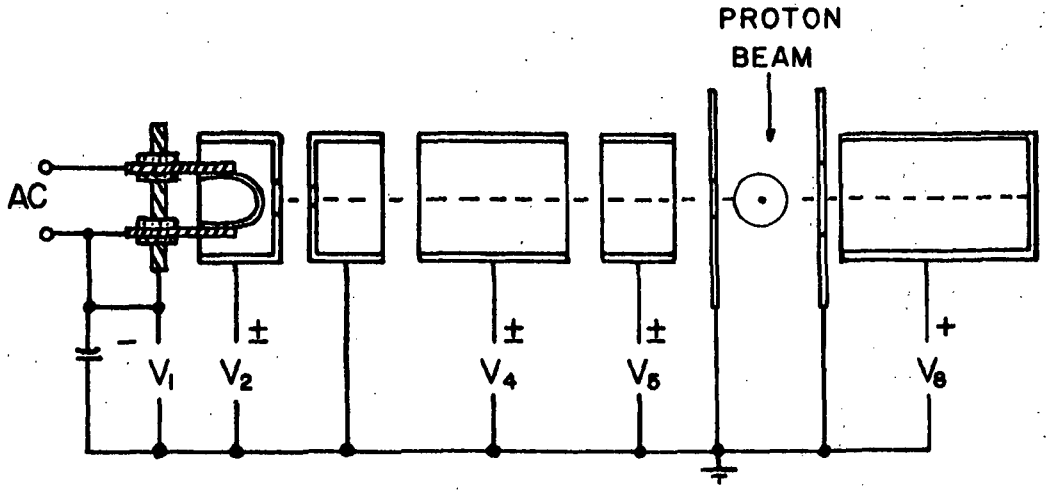

Figure 3-4.

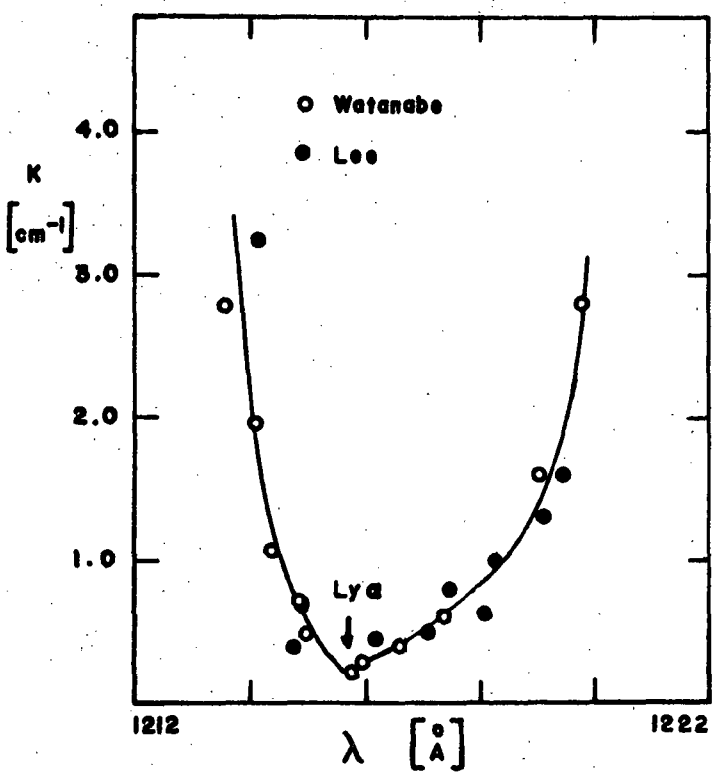

Figure 3-5.

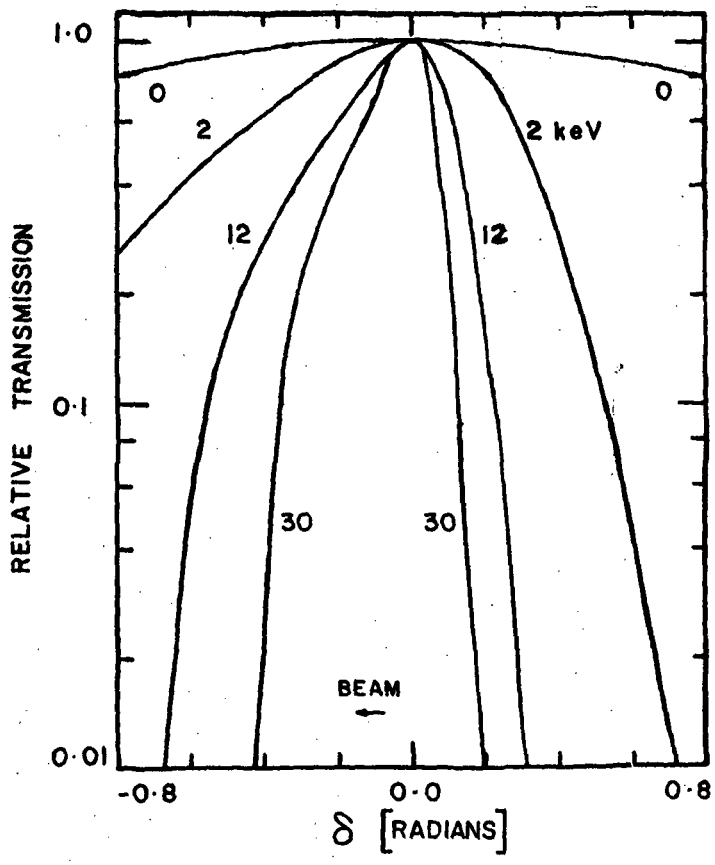
1·0
0·1
0·01
RELATIVE TRANSMISSION
0
2
12
30
2 keV
0
12
30
BEAM
-0·8
0·0
0·8
δ [RADIANS]

Figure 3-6.

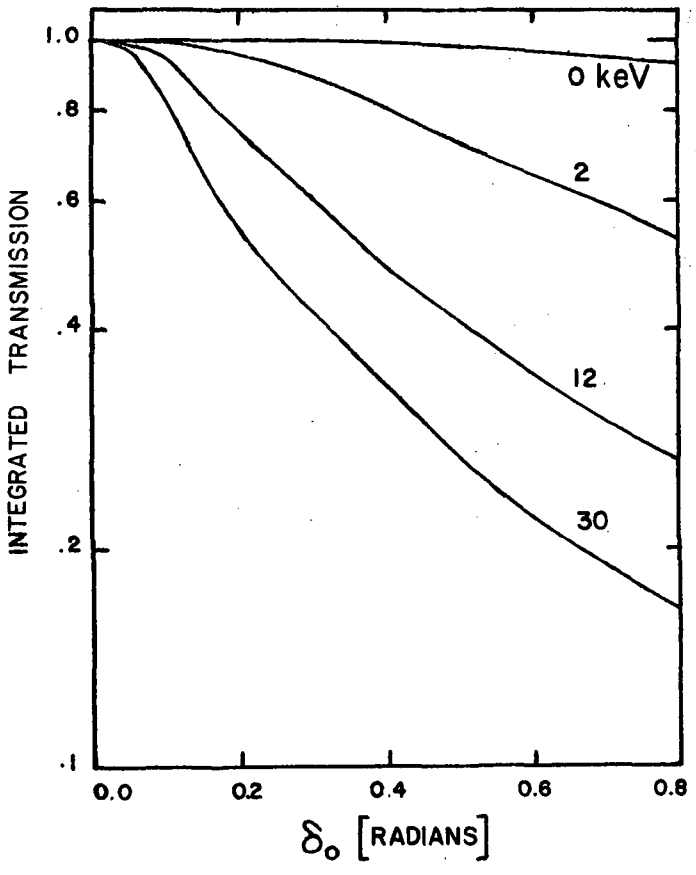
INTEGRATED TRANSMISSION
1.0
.8
.6
.4
.2
.1
0.0
0.2
0.4
0.6
0.8
0 keV
2
12
30
δo [RADIANS]

Figure 3-7.

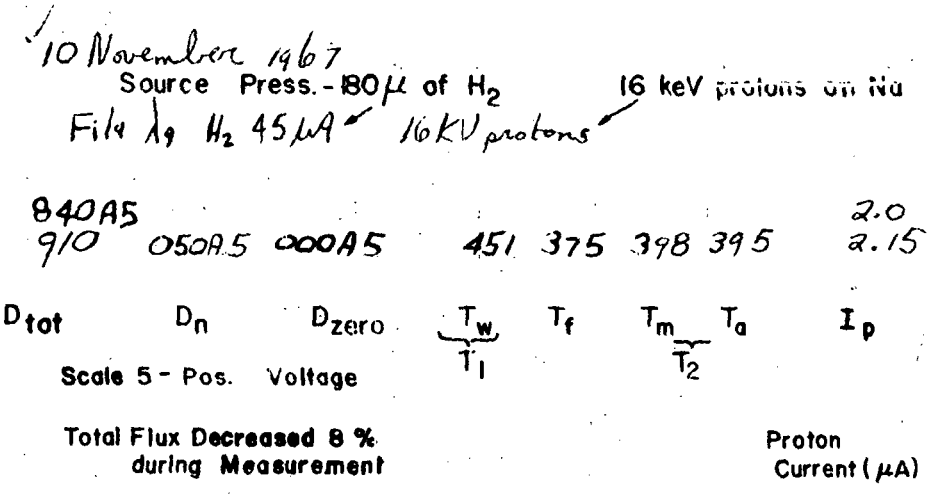

Figure 4-1.

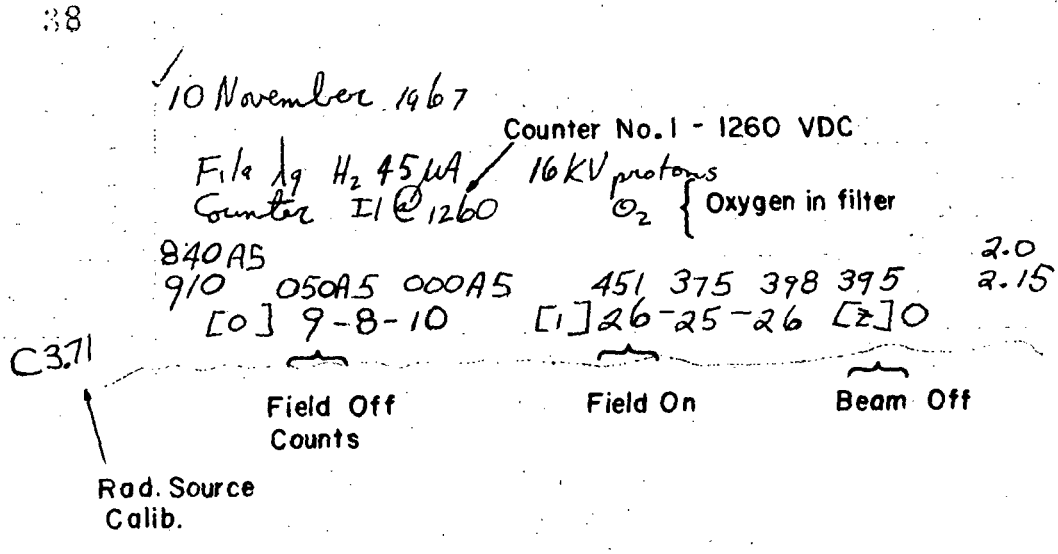

Figure 4-2.

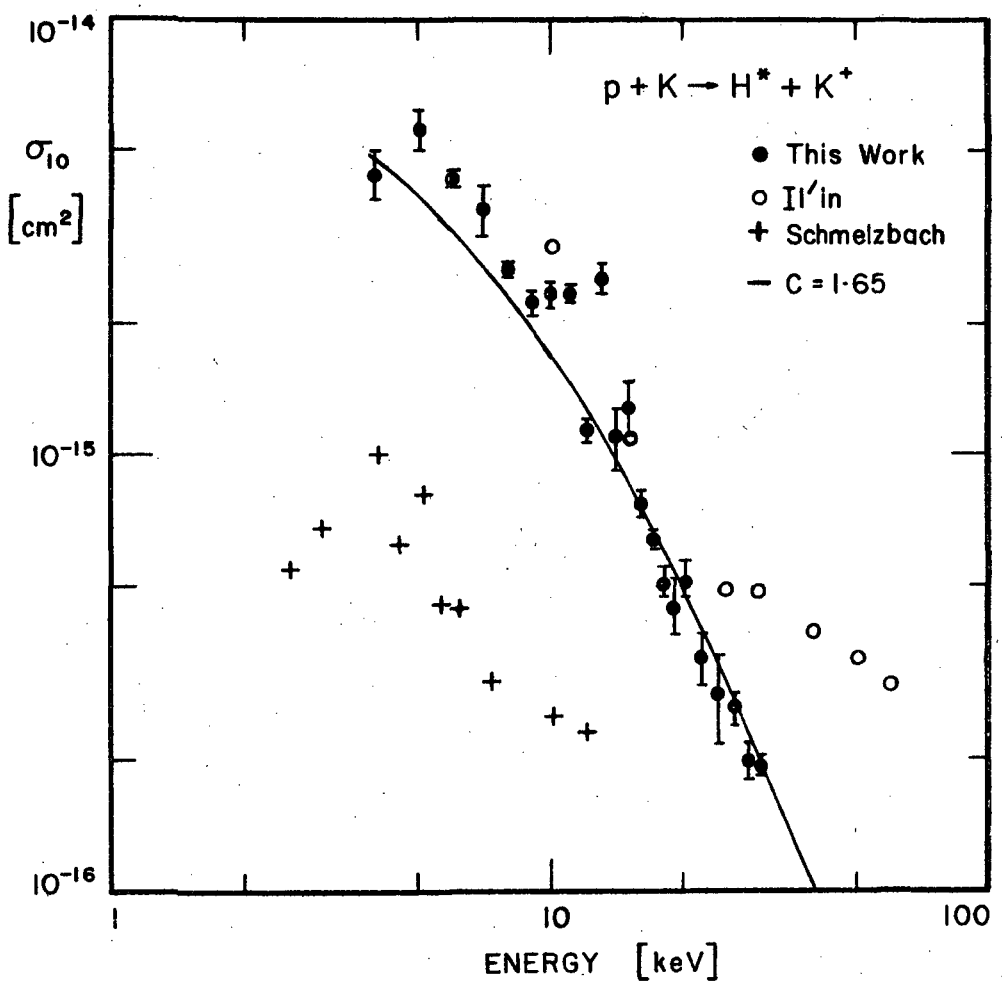
10^{-14}
σ_{10}
[cm²]
10^{-15}
10^{-16}
p + K → H* + K⁺
● This Work
○ Il'in
+ Schmelzbach
— C = 1·65
1
10
100
ENERGY [keV]

Figure 5-1.

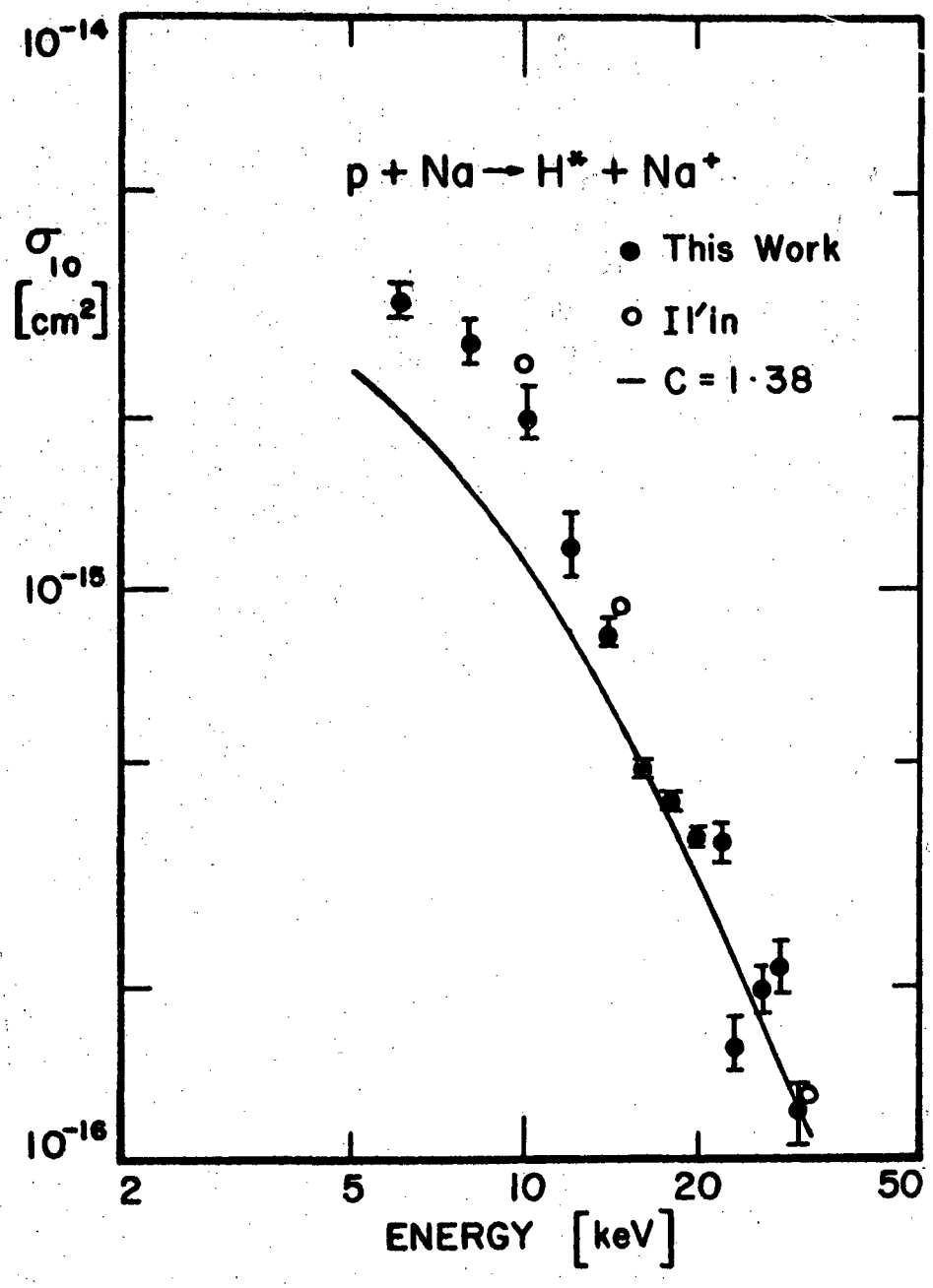
10^{-14}
10^{-15}
10^{-16}
σ_{10} [cm^2]
p + Na → H* + Na+
● This Work
o Il'in
— C = 1·38
2
5
10
20
50
ENERGY [keV]

Figure 5-2.

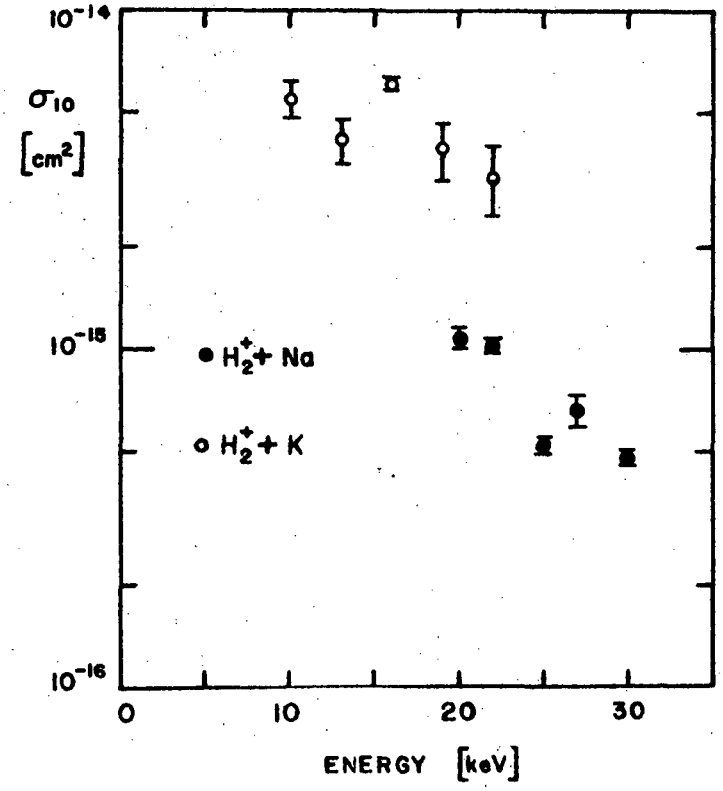

Figure 5-3.

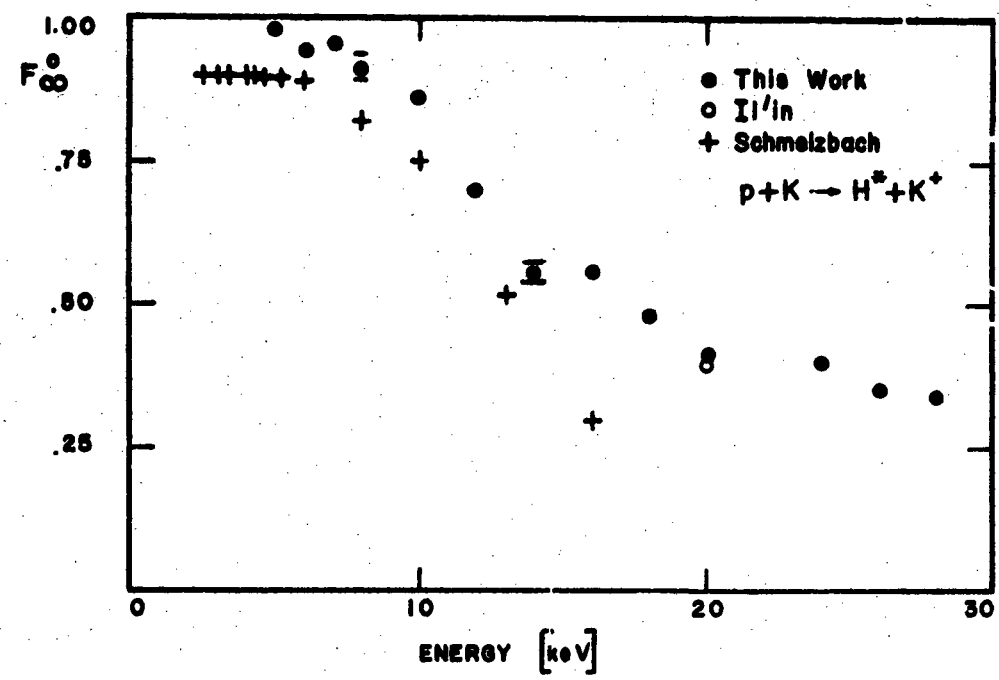

Figure 5-4.

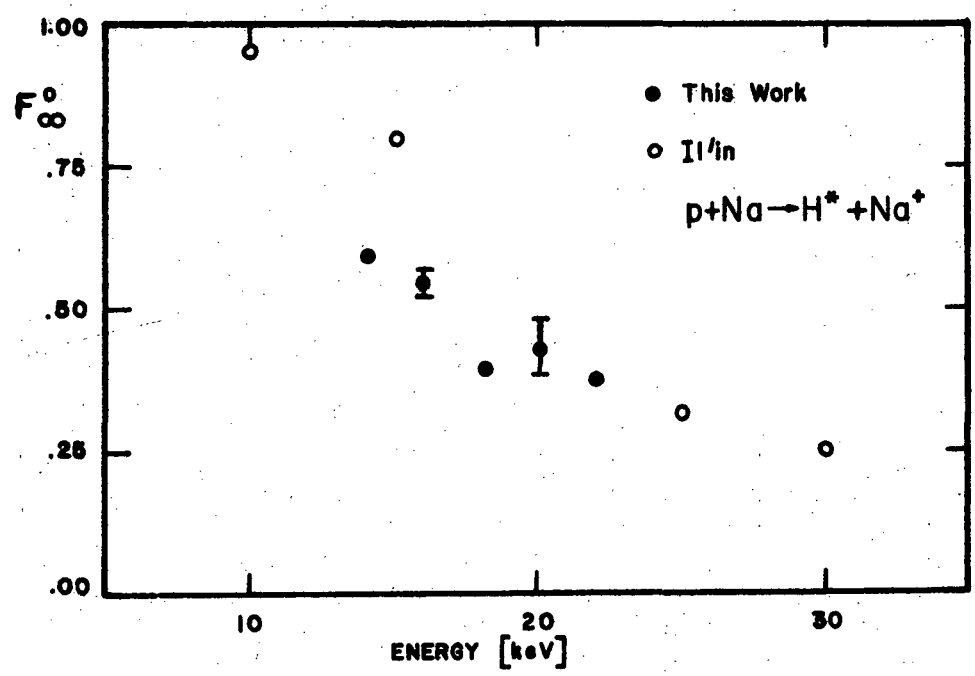

Figure 5-5.

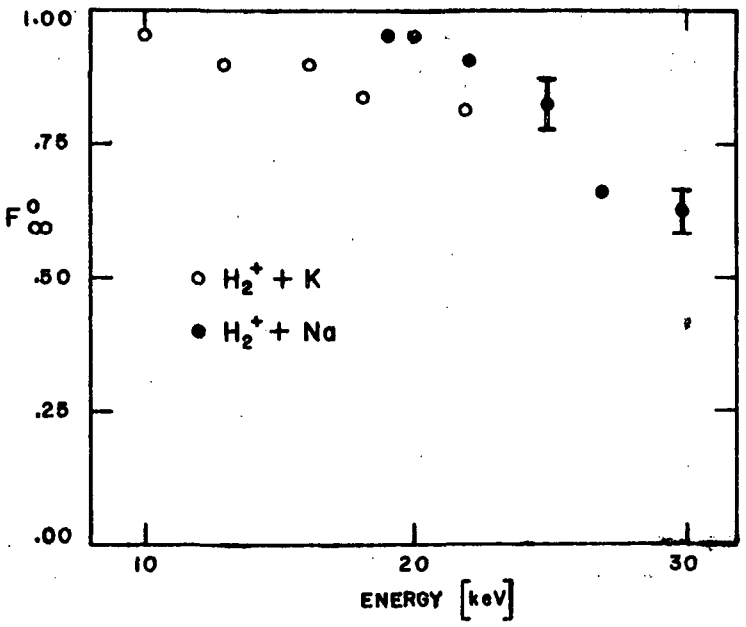

Figure 5-6.

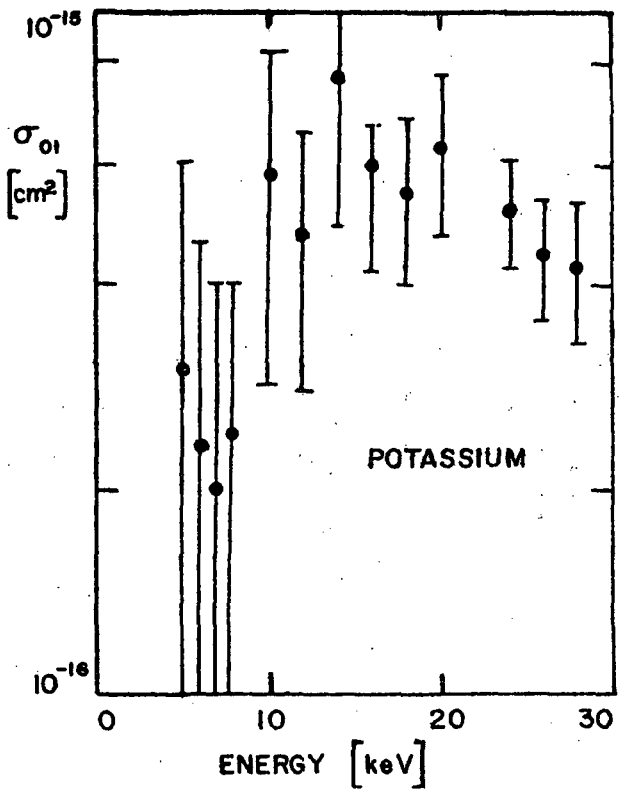

Figure 5-7.

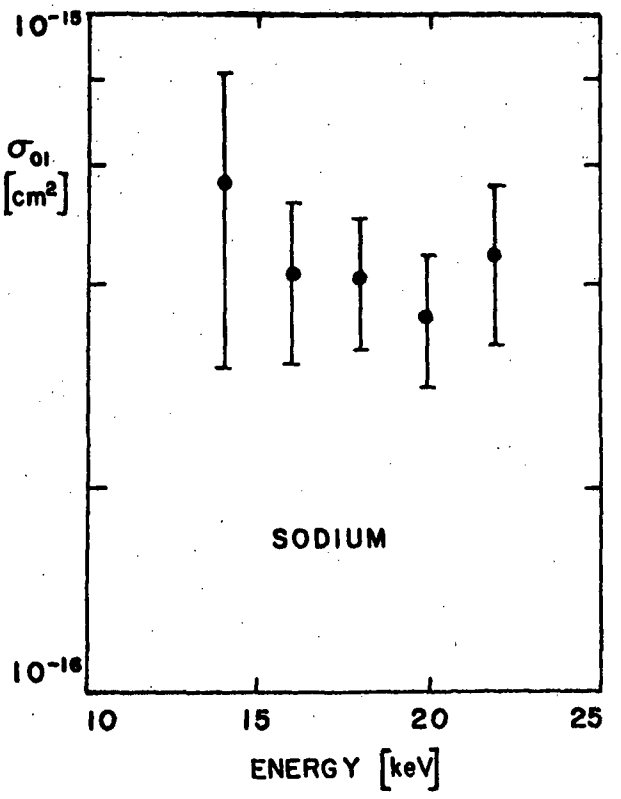

Figure 5-8.

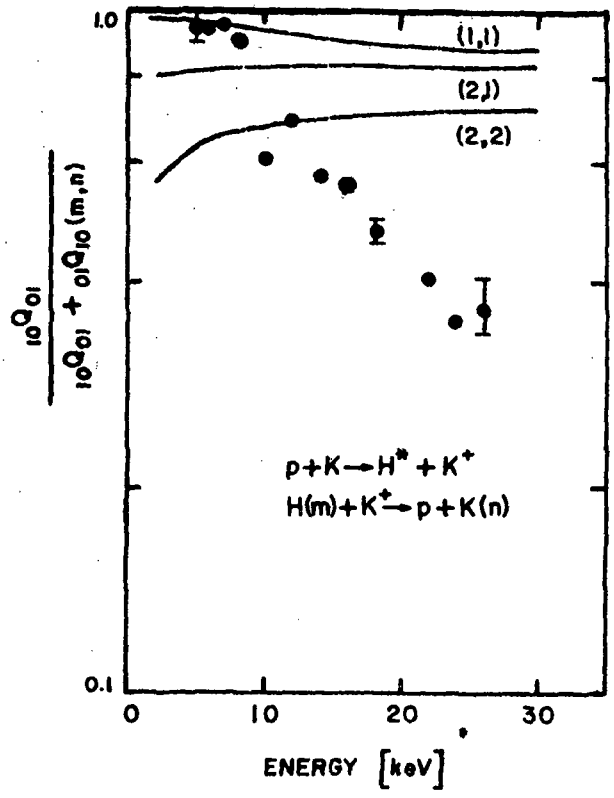

Figure 5-9.

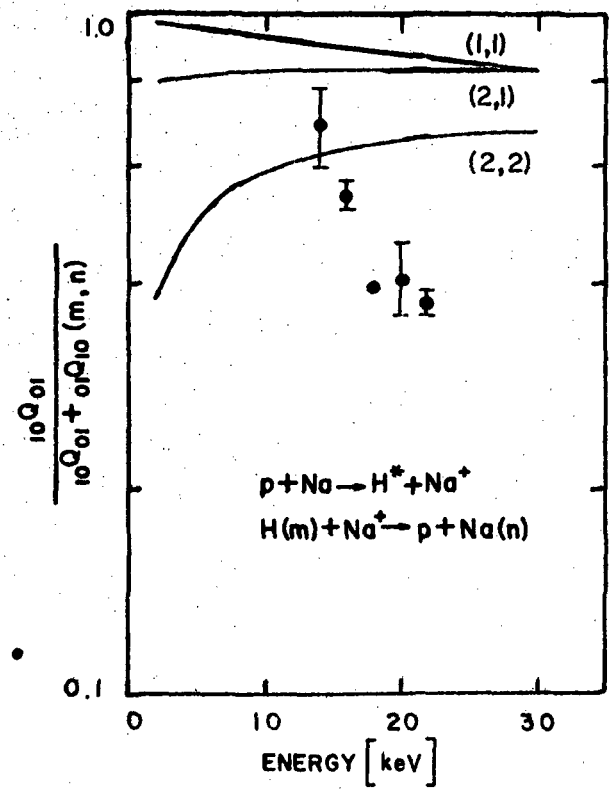

Figure 5-10.

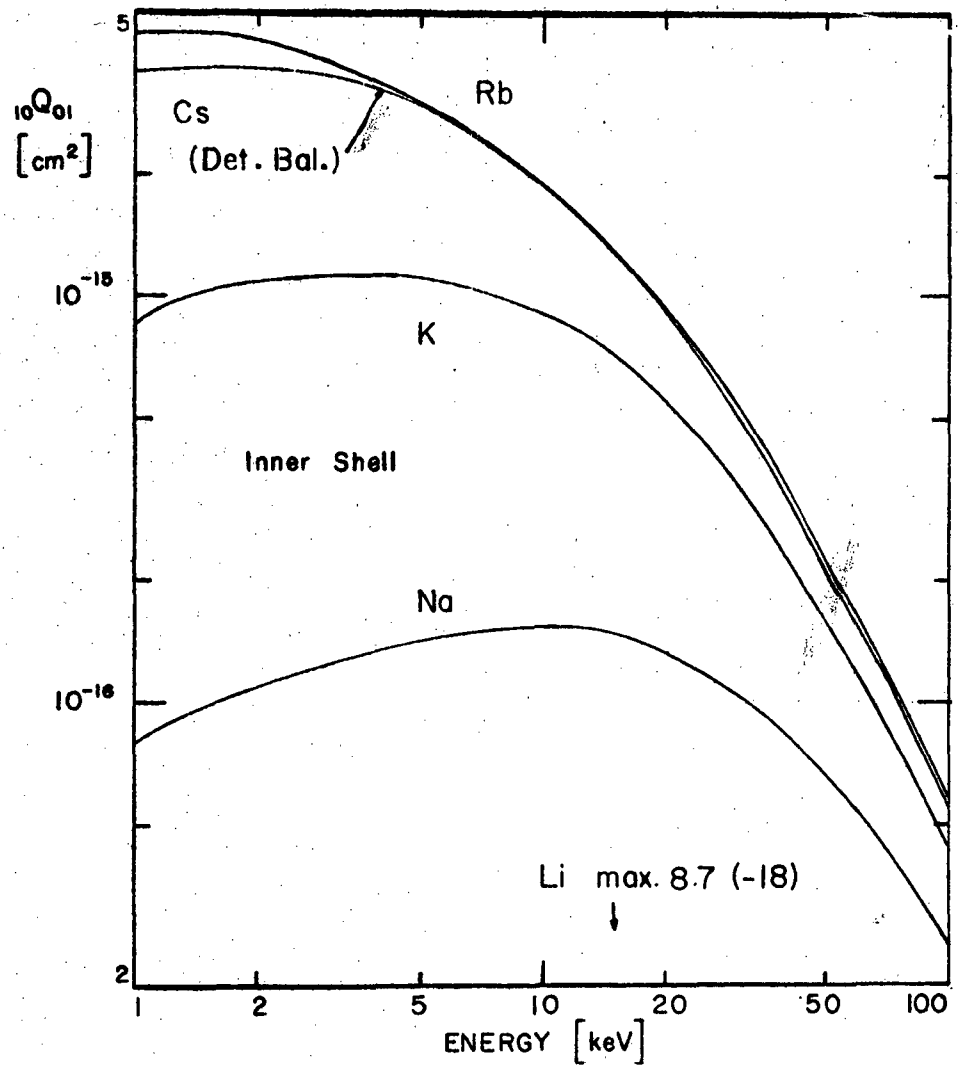
5
$_{10}Q_{01}$
[cm²]
Cs
(Det. Bal.)
Rb
10^{-15}
K
Inner Shell
Na
10^{-16}
Li max. 8.7 (-18)
2
1
2
5
10
20
50
100
ENERGY [keV]

Figure 5-11.

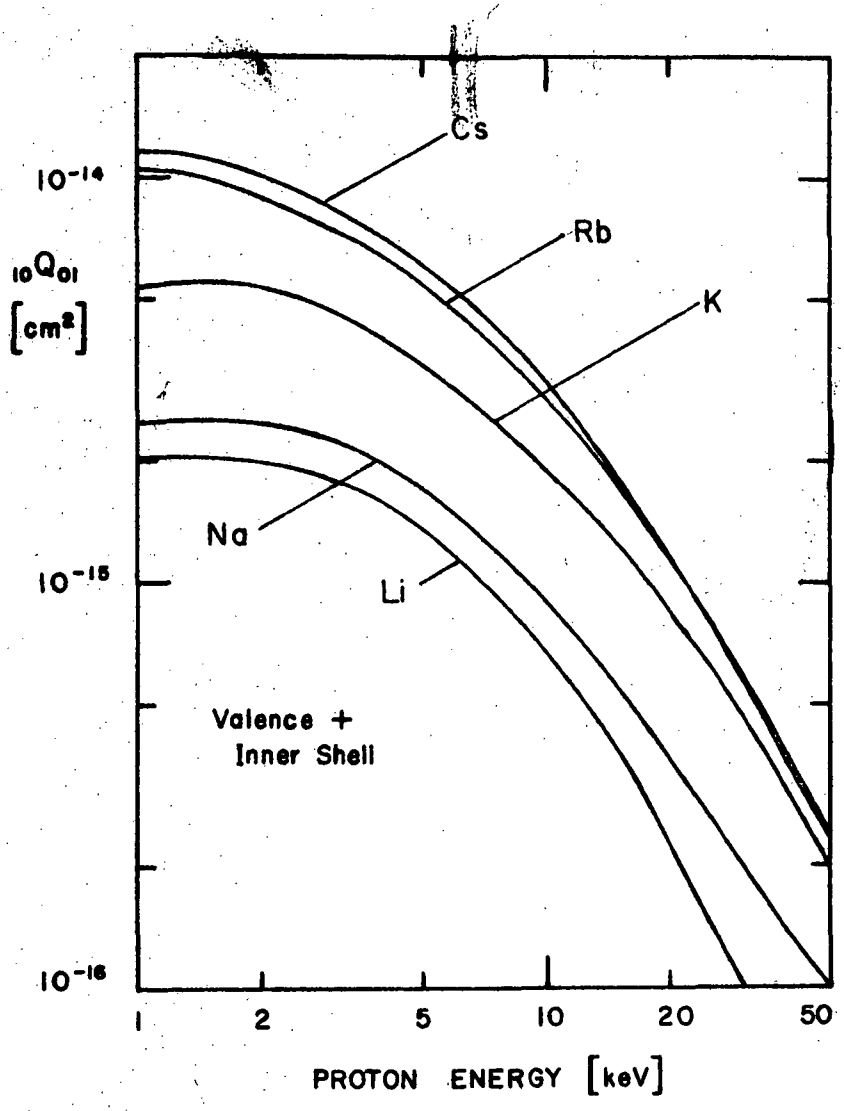
Cs
Rb
K
Na
Li
10^{-14}
10^{-15}
10^{-16}
$_{10}Q_{01}$
[cm²]
Valence +
Inner Shell
1
2
5
10
20
50
PROTON ENERGY [keV]

Figure 5-12.

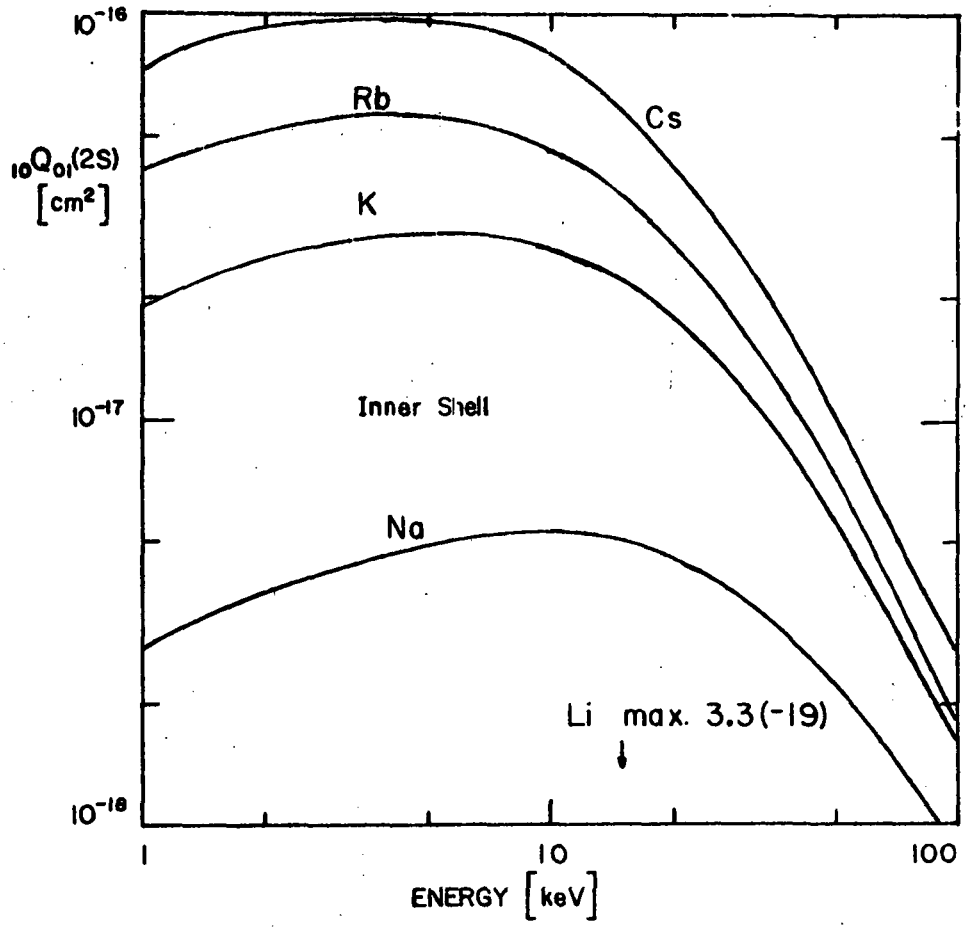
10^{-16}
10^{-17}
10^{-18}
$_{10}Q_{01}(2S)$
[cm²]
Rb
Cs
K
Inner Shell
Na
Li max. 3.3(-19)
1
10
100
ENERGY [keV]

Figure 5-13.

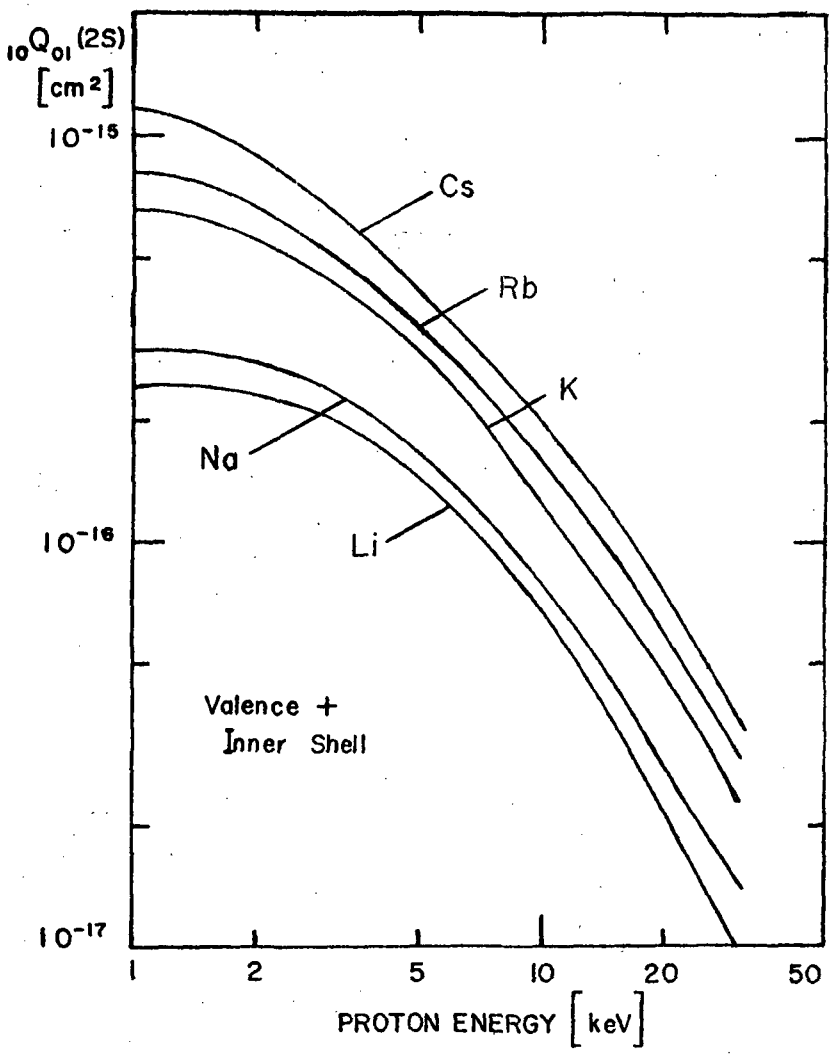
$_{10}Q_{01}(2S)$
[cm²]
10^{-15}
10^{-16}
10^{-17}
Cs
Rb
K
Na
Li
Valence +
Inner Shell
1
2
5
10
20
50
PROTON ENERGY [keV]

Figure 5-14.

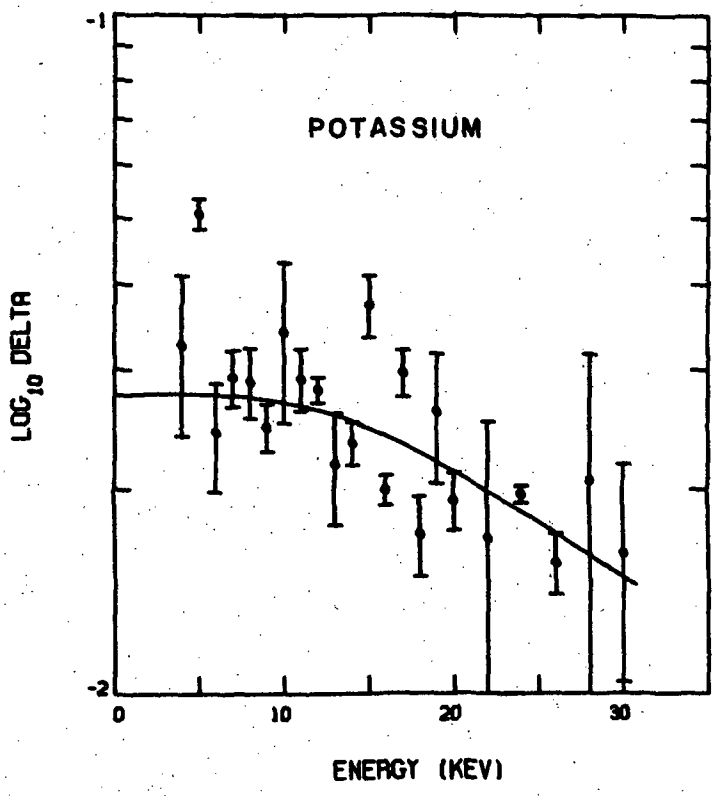

Figure 5-15.

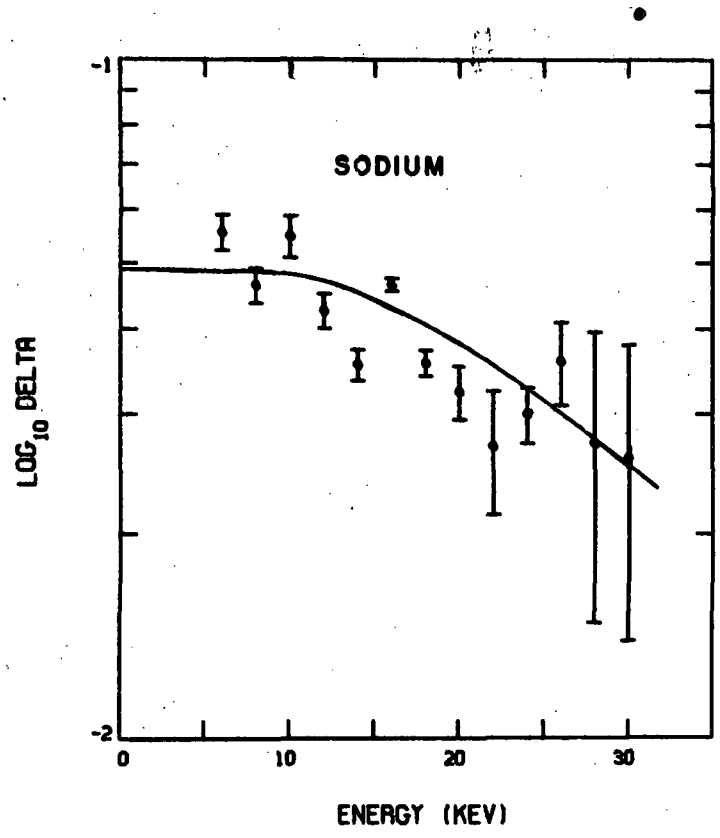

Figure 5-16.

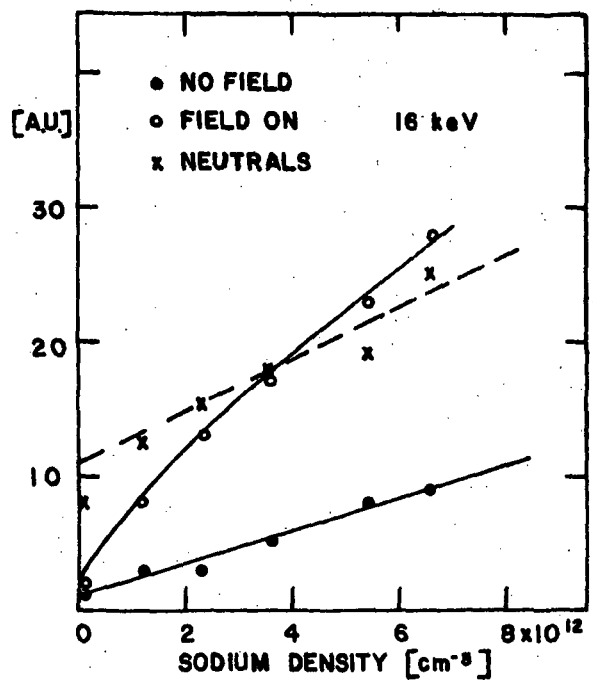
• NO FIELD
o FIELD ON
x NEUTRALS
16 keV
[A.U.]
30
20
10
0
2
4
6
8x10^12
SODIUM DENSITY [cm^-3]

Figure 5-17.

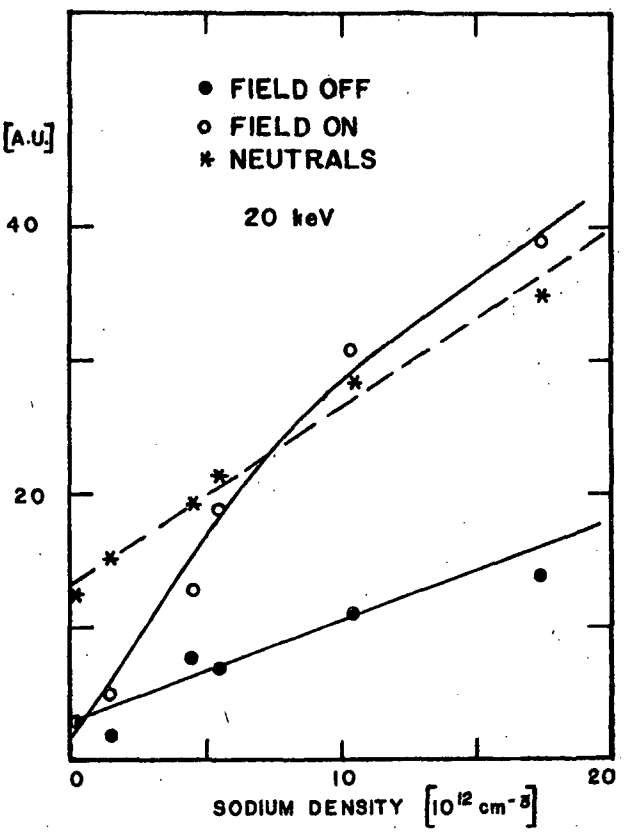
● FIELD OFF
○ FIELD ON
* NEUTRALS
20 keV
[A.U.]
40
20
0
10
20
SODIUM DENSITY [10¹² cm⁻³]

Figure 5-18.

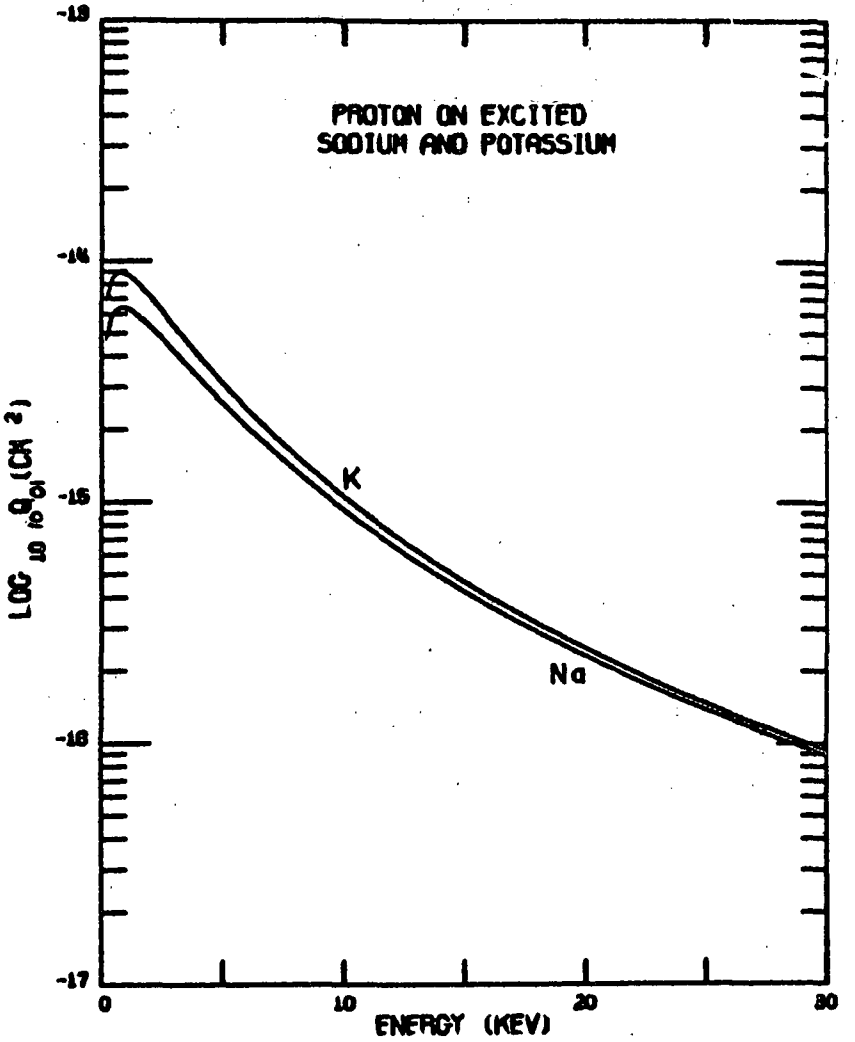
PROTON ON EXCITED
SODIUM AND POTASSIUM
K
Na
-13
-14
-15
-16
-17
0
10
20
30
ENERGY (KEV)

Figure 5-19.

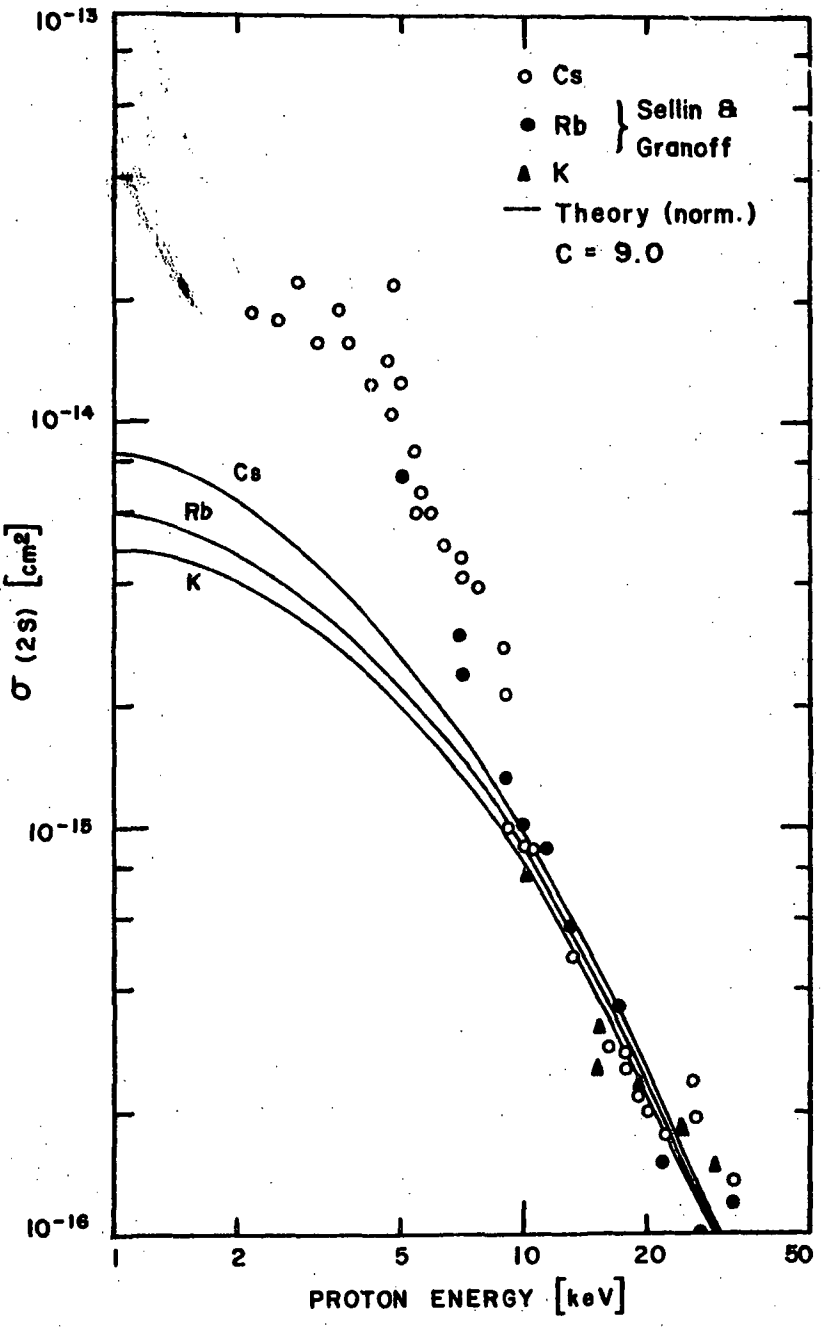
10⁻¹³
10⁻¹⁴
10⁻¹⁵
10⁻¹⁶
σ (2S) [cm²]
Cs
Rb
K
Cs
Rb
K
Sellin & Granoff
Theory (norm.)
C = 9.0
1
2
5
10
20
50
PROTON ENERGY [keV]

Figure 5-20.

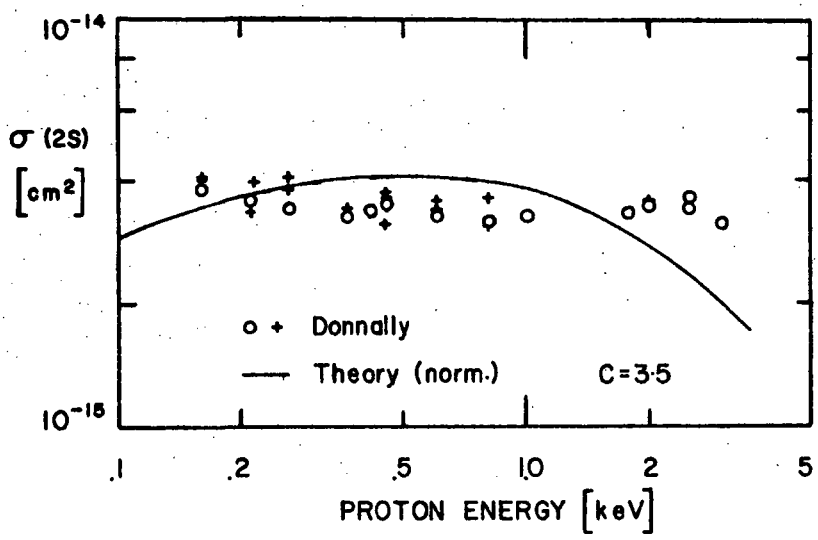
10^{-14}
σ (2S)
[cm^2]
10^{-15}
o + Donnally
Theory (norm.)
C=3.5
.1
.2
.5
1.0
2
5
PROTON ENERGY [keV]

Figure 5-21.

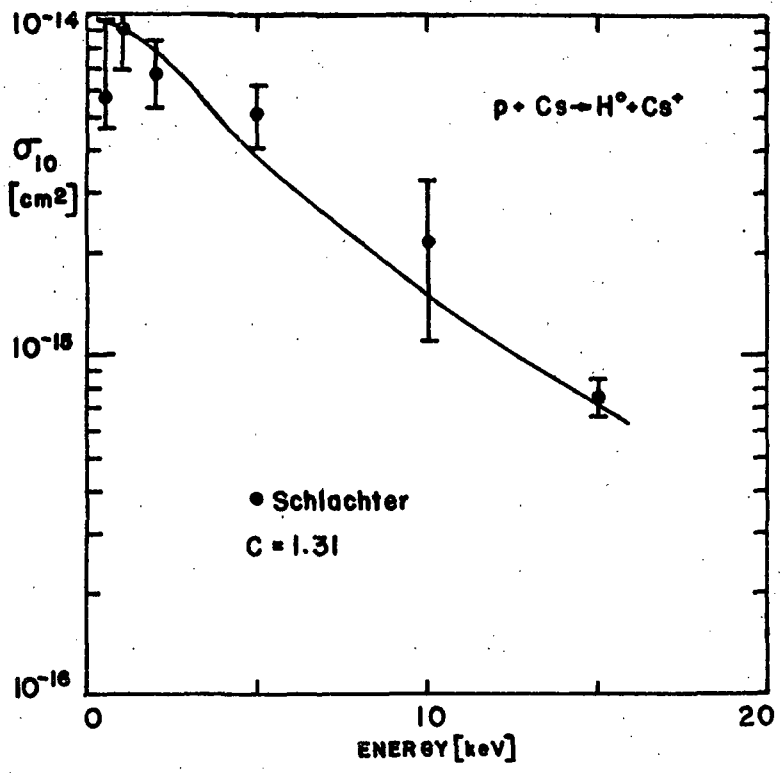
10^{-14}
σ_{10}
[cm2]
10^{-15}
10^{-16}
p + Cs → H° + Cs⁺
● Schlachter
C = 1.31
0
10
20
ENERGY [keV]

Figure 5-22.

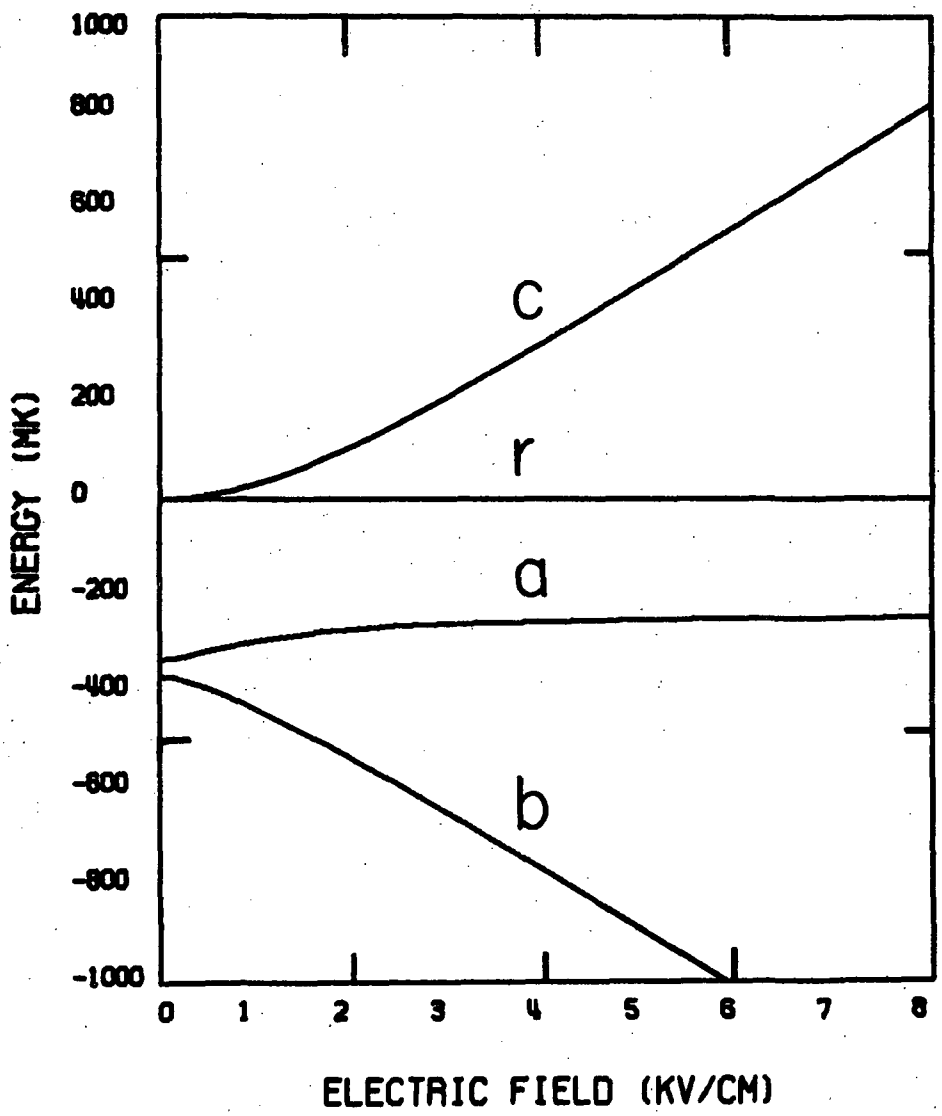
1000
800
600
400
200
0
-200
-400
-600
-800
-1000
ENERGY (MK)
c
r
a
b
0
1
2
3
4
5
6
7
8
ELECTRIC FIELD (KV/CM)

Figure C-1.

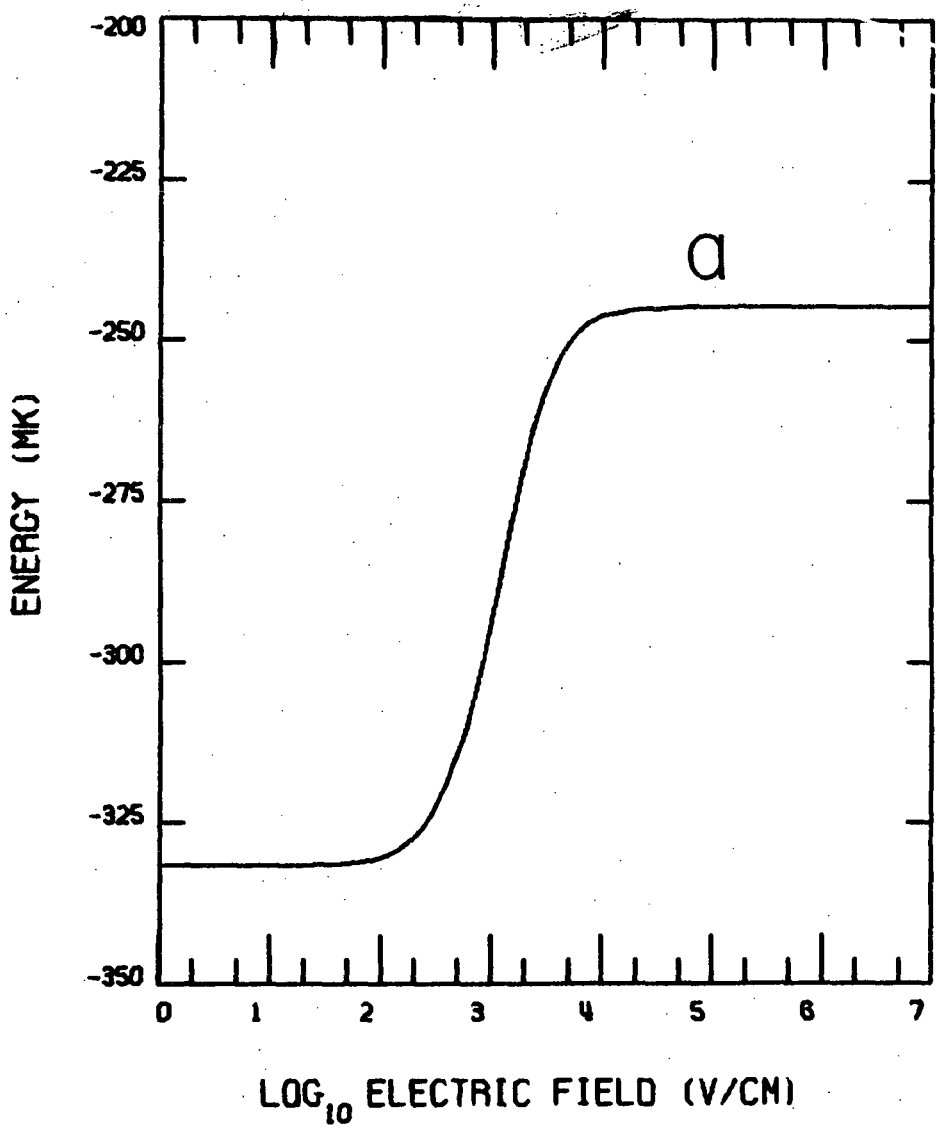
-200
-225
-250
-275
-300
-325
-350
ENERGY (MK)
a
0
1
2
3
4
5
6
7
LOG10 ELECTRIC FIELD (V/CM)

Figure C-2.

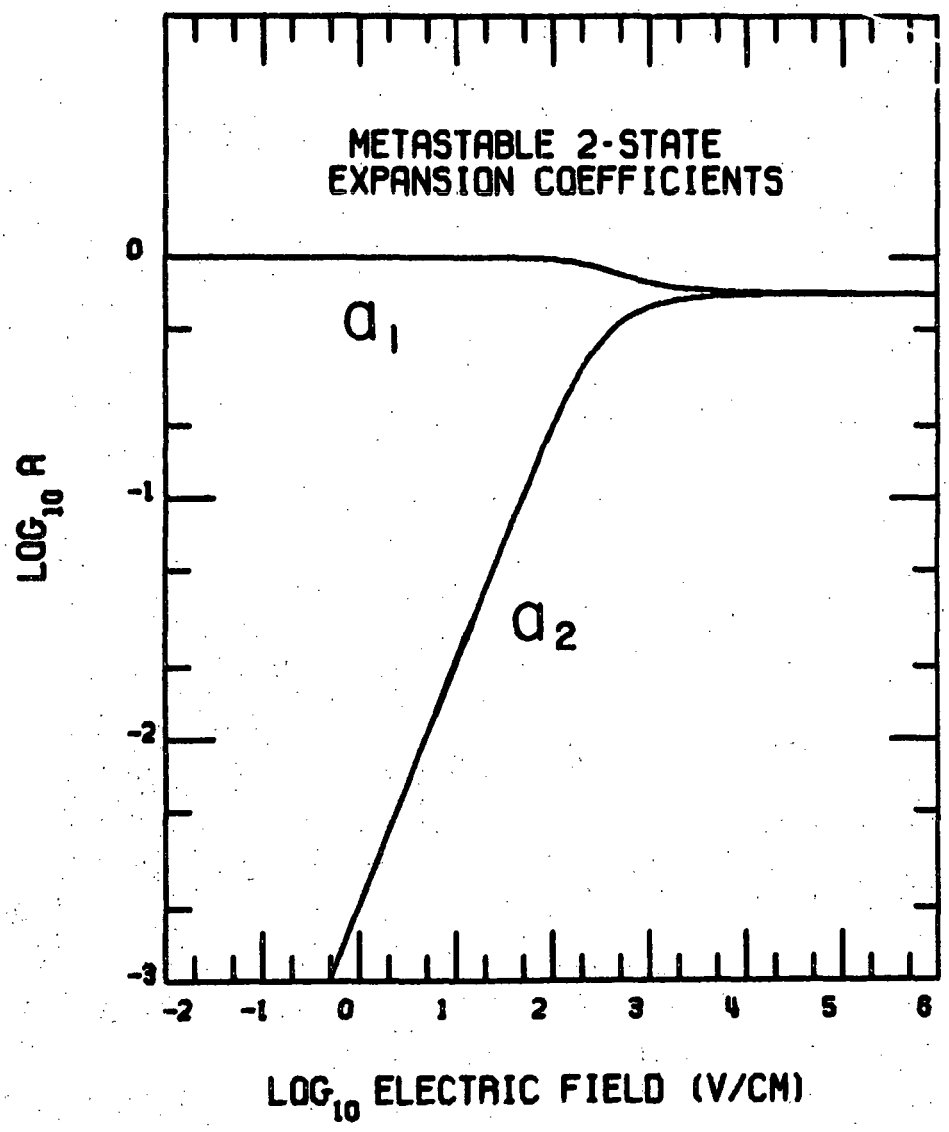
METASTABLE 2-STATE
EXPANSION COEFFICIENTS
a_1
a_2
LOG_{10} A
0
-1
-2
-3
-2
-1
0
1
2
3
4
5
6
LOG_{10} ELECTRIC FIELD (V/CM)

Figure C-3.

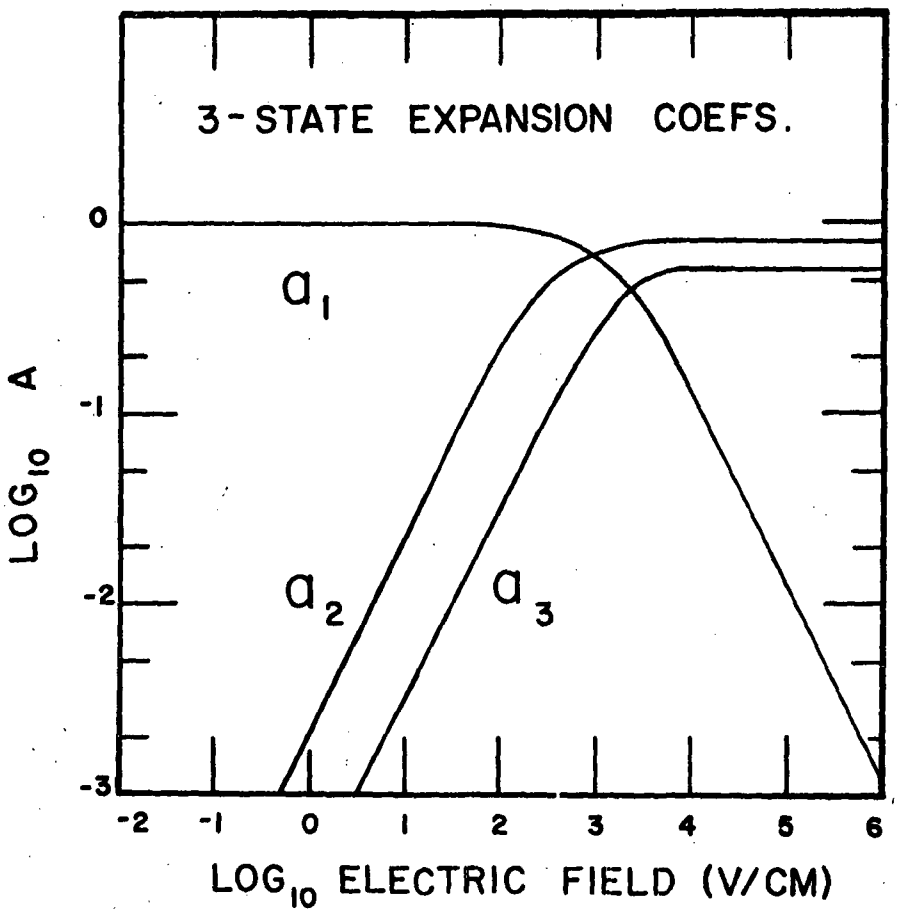
3-STATE EXPANSION COEFS.
0
-1
-2
-3
a_1
a_2
a_3
LOG_{10} A
-2
-1
0
1
2
3
4
5
6
LOG_{10} ELECTRIC FIELD (V/CM)

Figure C-4.

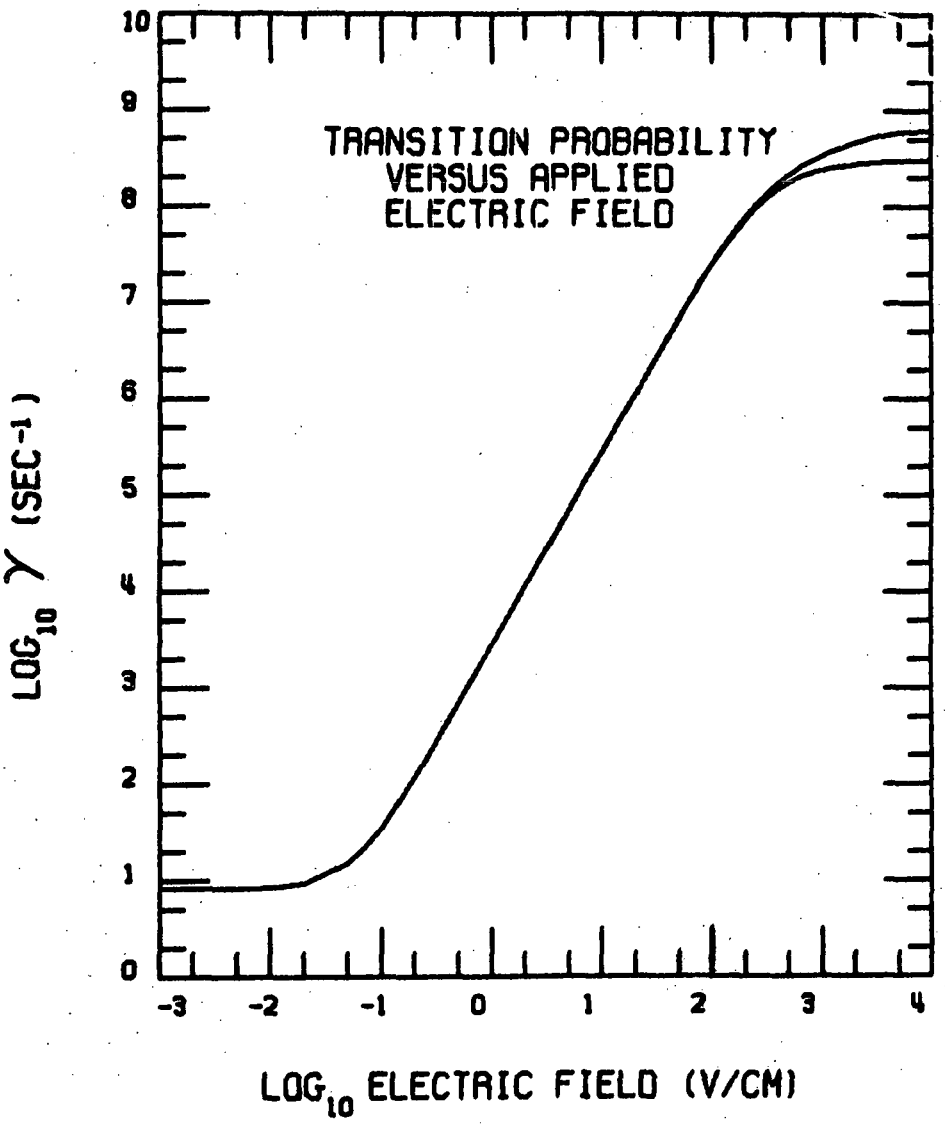
TRANSITION PROBABILITY
VERSUS APPLIED
ELECTRIC FIELD
LOG10 γ (SEC-1)
LOG10 ELECTRIC FIELD (V/CM)
10
9
8
7
6
5
4
3
2
1
0
-3
-2
-1
0
1
2
3
4

Figure C-5.

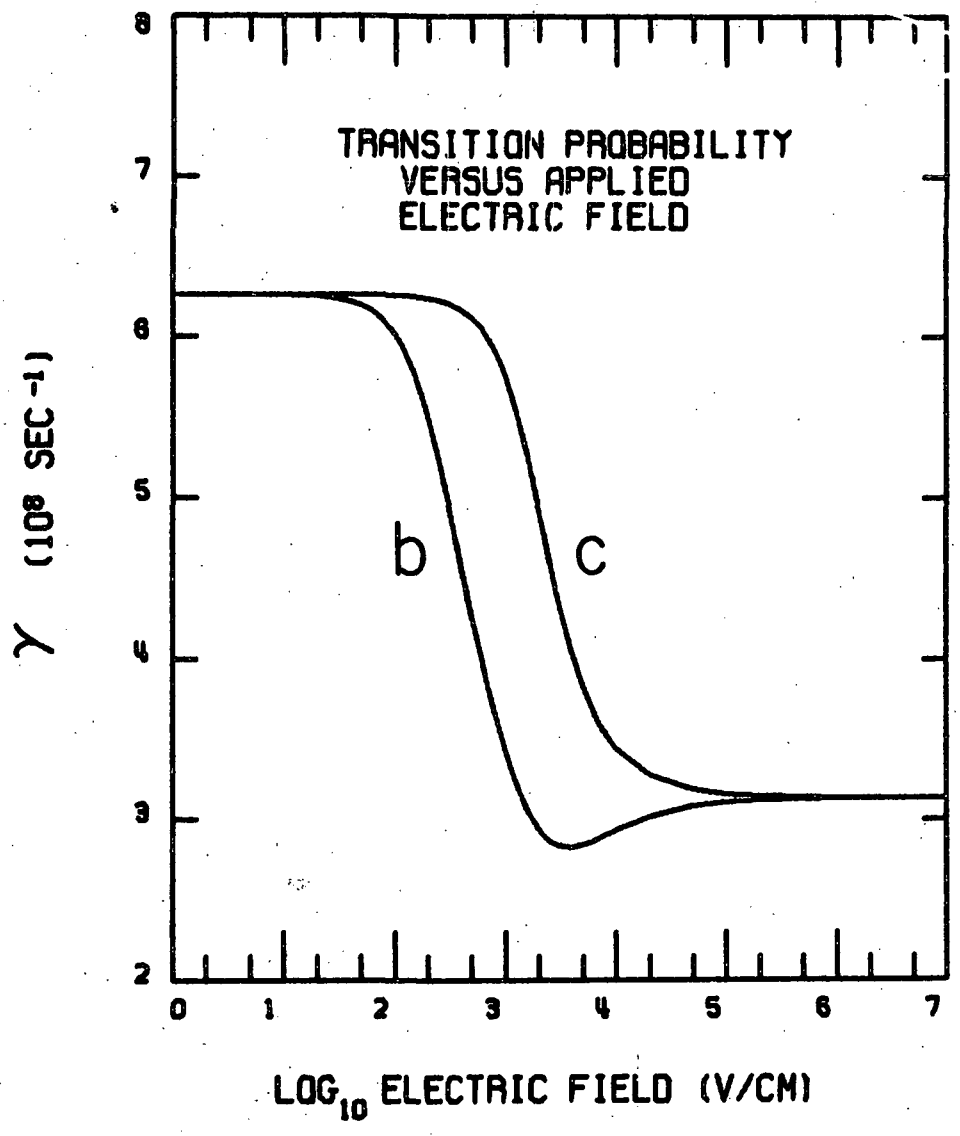
TRANSITION PROBABILITY
VERSUS APPLIED
ELECTRIC FIELD
b
c
γ (10⁸ SEC⁻¹)
LOG10 ELECTRIC FIELD (V/CM)
8
7
6
5
4
3
2
0
1
2
3
4
5
6
7

Figure C-6.

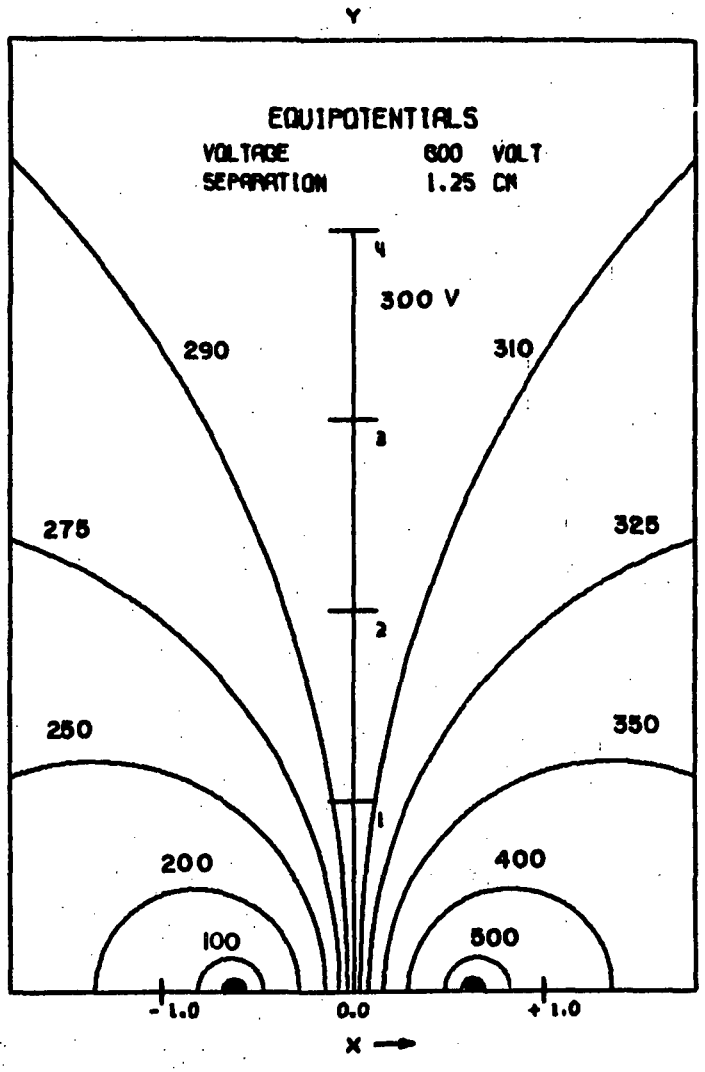
Y
EQUIPOTENTIALS
VOLTAGE 600 VOLT
SEPARATION 1.25 CM
4
300 V
290
310
3
275
325
2
250
350
1
200
400
100
500
-1.0
0.0
+1.0
X

Figure D-1.

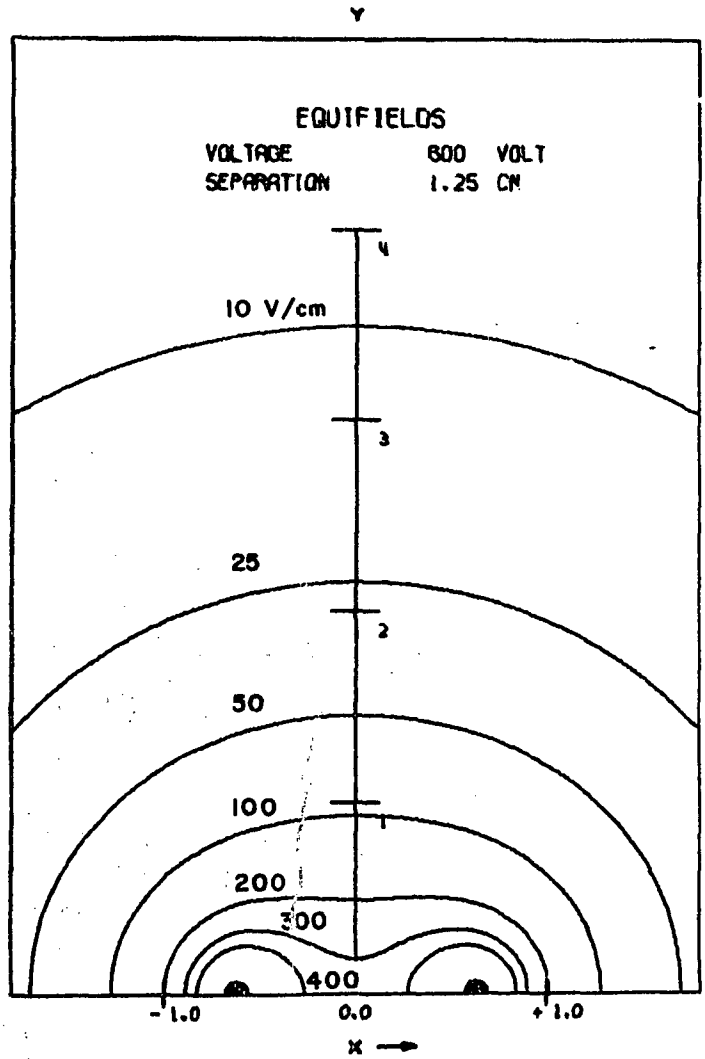
Y
EQUIFIELDS
VOLTAGE 600 VOLT
SEPARATION 1.25 CM
4
10 V/cm
3
25
2
50
100
1
200
300
400
-1.0
0.0
+1.0
X

Figure D-2.